High Field MRI:
Developments for carotid artery and brain perfusion imaging

Wouter Koning

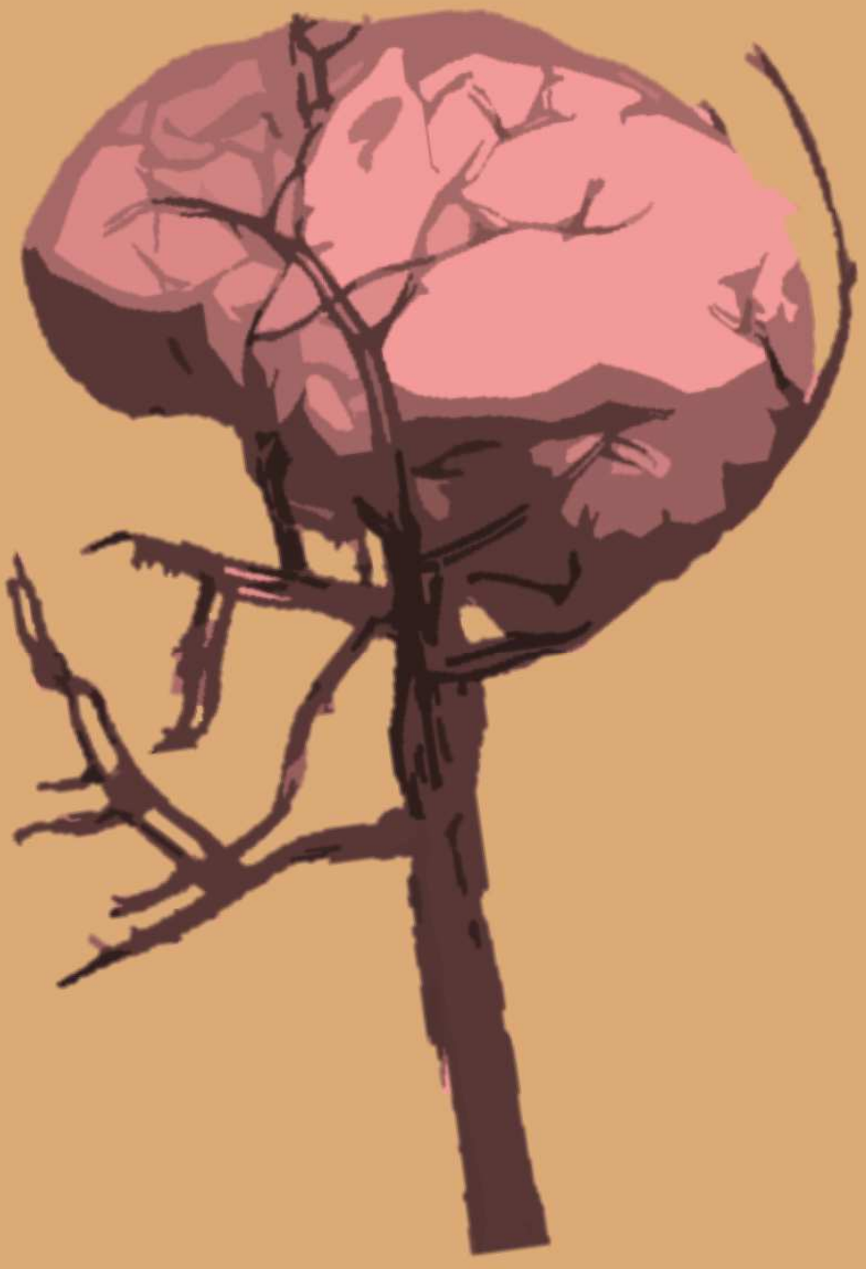

High Field MRI: Developments for carotid artery and brain perfusion imaging

Wouter Koning

This research was supported by the Center for Translational Molecular Medicine and the Dutch Heart Foundation (PARISk)

The printing of this thesis was financially supported by Philips Nederland and the Röntgen Stichting.

Published by: Uitgeverij BOXPress, 's Hertogenbosch, The Netherlands
ISBN: 978-90-8891-977-0

High Field MRI: Developments for carotid artery and brain perfusion imaging

Hoge veldsterkte MRI: Ontwikkelingen voor de beeldvorming van de halsslagaders en hersendoorbloeding

(met een samenvatting in het Nederlands)

Proefschrift

ter verkrijging van de graad van doctor aan de Universiteit Utrecht op gezag van de rector magnificus, prof.dr. G.J. van der Zwaan, ingevolge het besluit van het college voor promoties in het openbaar te verdedigen op

dinsdag 21 oktober 2014 des ochtends te 10.30 uur

door

Wouter Koning

geboren op 4 oktober 1979

te Wageningen

Promotor: Prof. dr. P.R. Luijten

Copromotoren: Dr. D.W.J. Klomp

Dr. ir. J.J.M. Zwanenburg

Table of contents

Table of contents

Chapter 1

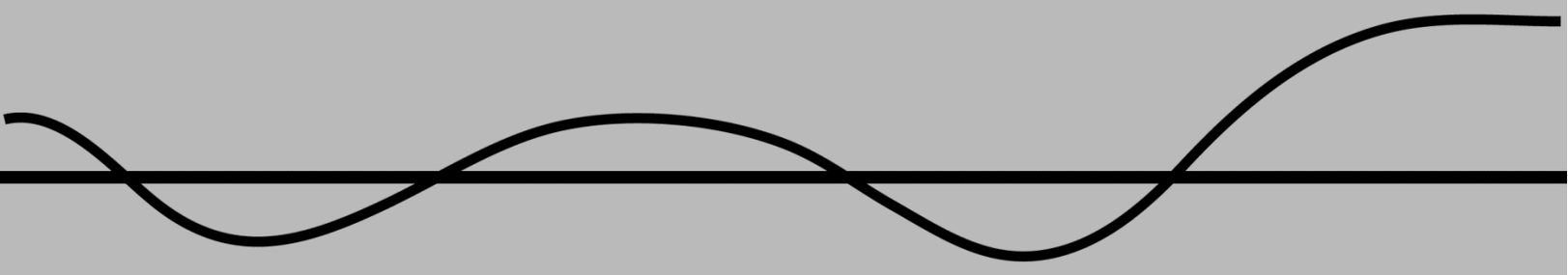

General Introduction

1.1 The carotid arteries and high field MRI

This thesis is about high field MRI and this thesis is about the carotid arteries. The carotid artery is often the crime scene of a dangerous and unfortunately quite common occurrence of an atherosclerotic plaque. High field MRI is the toolbox for which, in the research presented in this thesis, the necessary developments were explored, primary to be able to look into these carotid arteries in more detail and secondary, to use the carotid arteries to measure brain perfusion.

1.1.1 Carotid atherosclerosis

The common carotid arteries (CCA) are the two main arteries located in the left and the right side of the neck. They are responsible for supplying the brain with oxygenated blood. Around the height of the jaws the CCA's split up into the internal and the external carotid arteries (see Figure 1.1).

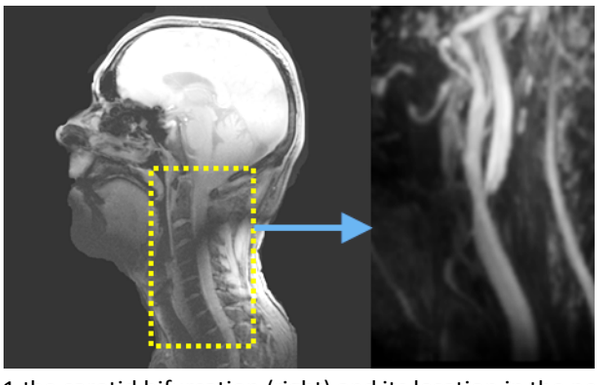

Figure 1.1 the carotid bifurcation (right) and its location in the neck (left).

Around this bifurcation, turbulence and velocity fluctuations of the blood flow are believed to play a role in the development of atherosclerosis (1, 2). Therefore, the formation of *atherosclerotic plaques* at this location is a common and dangerous disease. Atherosclerotic plaques in the carotid arteries can periodically release small emboli's into the bloodstream (3). These emboli's can end up in the brain, or the plaque can even completely rupture causing infarctions in the brain. Based on the estimated risk of rupture of an individual plaque, one can decide to remove the plaque during an endarterectomy. Assessment of this risk of rupture is in general clinical practice based on degree of stenosis, defined as the percentage of occlusion. Above a certain threshold of the degree of stenosis the risk of rupture of the plaque is considered too high. However, it has been shown (4-7) that even a small degree of stenosis can be very dangerous, while a fully stenosed carotid artery can be harmless. With CT imaging high resolution lumen images can be acquired, however plaque components can hardly be distinguished. Ultrasound allows for carotid imaging with very high temporal resolution, however cannot provide sufficient contrast for plaque analysis. Therefore, MRI is often the imaging modality of choice when vessel walls and plaques have to be

studied. Many studies have been done on characterizing plaque characteristics using MRI (8-10). Several components can already be identified with MRI: fibrous cap (FC) thickness, intra-plaque hemorrhage (IPH) and the size of the lipid rich/necrotic core (LR/NC) (11). The goal of this characterization would eventually be to predict the vulnerability of the plaque by quantifying these plaque characteristics and correlate them retrospectively to clinical events in the brain by means of cohort studies. An accurate prediction would result in a better decision whether or not to conduct an endarterectomy.

1.1.2 High field MRI

This is where high field MRI comes in. Some plaque components have details on the microscopic scale. Some of these details may be within the reach of MRI, some may be beyond, and some may be on the edge. Some of the microscopic features, like the thickness of the fibrous cap holding the plaque together, may be very important for the assessment of the risk of rupture. For other plaque components, like neovascularization, the sensitivity to detect a voxel containing neovascularization with sufficient contrast, can be the limiting factor. At a field strength of 7T, there is a higher intrinsic SNR because of a larger population of protons whose magnetic moment is in the spin-up state, according to the Boltzmann distribution. On top of that, contrasts are changed at 7T. Tissue relaxation parameters change and susceptibility differences between different tissues are increased, making 7T more sensitive to pick up certain properties. At this moment, 3T is the field strengths at which the highest quality of MR images of the carotid arteries are acquired. However, if the above mentioned gains of an ultra-high field strength can be utilized, this may significantly improve the risk assessment of an individual atherosclerotic plaque.

1.1.3 Brain perfusion imaging

The carotid arteries are also a region of interest for brain perfusion imaging. Brain perfusion can be measured by arterial spin labelling (ASL). By magnetic labelling of the blood in the brain feeding arteries in the neck, the carotid and vertebral arteries, perfusion in the brain can be quantified without the need for an injected contrast agent. However, the magnetically labelled blood is losing its magnetization in time. This is why there is a particular interest for perfusion imaging at high field strength, since the longer T_1 of blood causes the blood to stay magnetized longer, which in turn could benefit the measurements of brain perfusion.

But first, the next section describes some historical background that leads to considerations which can be neglected at lower field strengths, but become very important when going to a field strength as high as 7 tesla.

1.2 Intermezzo: a brief flight through electromagnetic history

All early history in electromagnetics culminates towards the formulation of the famous Maxwell equations, published by James Clerk Maxwell around 1861. This set of equations are at the basis of all electrical and magnetic phenomena, and were all formulated based on simple observations made earlier by famous players like Michael Faraday and Hans Christian Ørsted. To get to that result, Karl Friedrich Gauss formulated earlier two relatively simple laws describing electric fields (E) and magnetic fields (B): first, the total electric flux (ϕ_E) through any closed surface is proportional to the total charge (Q) inside that surface (Equation 1). And second, the total magnetic flux (ϕ_B) through any closed surface equals zero (Equation 2). Michael Faraday described magnetic induction, after observing that a moving magnet (time varying ϕ_B) causes an electric field and thus a current in a nearby conductor (Equation 3). Likewise, Maxwell himself adapted Ampere's law[1], and showed that a time varying ϕ_E in turn causes a magnetic field (Equation 4).

The Maxwell equations (for simplicity applied to free space, so no dielectric or magnetic material present) as found in many physics textbooks:

Gauss's law
$$\oint \boldsymbol{E} \cdot d\boldsymbol{A} = \frac{Q}{\epsilon_0} \tag{1}$$

Gauss's law in magnetism
$$\oint \boldsymbol{B} \cdot d\boldsymbol{A} = 0 \tag{2}$$

Faraday's law
$$\oint \boldsymbol{E} \cdot d\boldsymbol{s} = -\frac{d\boldsymbol{\phi}_B}{dt} \tag{3}$$

Ampere-Maxwell law
$$\oint \boldsymbol{B} \cdot d\boldsymbol{s} = \mu_0 I + \epsilon_0 \mu_0 \frac{d\boldsymbol{\phi}_E}{dt} \tag{4}$$

where ***dA*** represents an infinitesimal surface segment and ***ds*** represents an infinitesimal line segment, ϵ_0 is the permitivity in free space and equals 8.8542 x 10^{-12} C^2 N^{-1} m^{-2}, μ_0 is the permeability of free space and equals 12.566 x 10^{-7} T m A^{-1}.

This is where the astonishing part starts. These equations were formulated to describe the *observed* electromagnetic phenomena. However, Maxwell found a surprising prediction following directly from these equations, something for which *no observations* had been done. Maxwell found that Equations (3) and (4) can be combined to obtain a wave equation describing both the

[1] Maxwell added the essential displacement current, a current caused by change in charge density, to make ampere's law valid in all situations, like on a capacitor or dipole antenna driven by an alternating voltage source. On a capacitor there is obviously no net current passing the capacitor; however a changing charge density can still allow for a current on the conductors towards the capacitor.

electric and the magnetic fields. Electric and magnetic fields seemed to behave like plane transverse waves: electromagnetic (EM) waves (Figure 1.2). And *even more* surprising: following these wave equations (similar as the conventional wave equations describing other wave phenomena), the *wave speed* (*v*) followed directly from these equations:

$$v = \frac{1}{\sqrt{\epsilon_0 \mu_0}} \tag{5}$$

Since ϵ_0 and μ_0 where already empirically determined at that time, Maxwell found a wave speed of 299,800 km/s in vacuum, the speed of light![2] Maxwell concluded that light is a form of electromagnetic radiation[3].

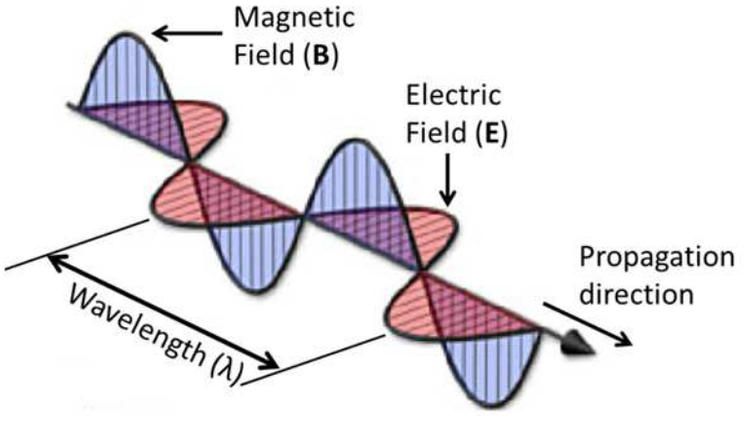

Figure 1.2. A propagating electromagnetic wave

The wavelength λ of the EM-wave is inverse proportional to the frequency *f*.

$$\lambda = \frac{v}{f} \tag{6}$$

When using MRI at a field strength as high as 7T, two of the above described phenomena are causing effects that have to be taken carefully into account. Effects that were not so important, or could even be neglected, at lower field strengths:

1. At 7T, the speed of light, or the wave propagation speed, is no longer high enough to neglect wavelength effects. This is clarified in Section 1.3.

[2] At that time the speed of light had only be determined by looking at one of Jupiters moons (Roemer, 220,000 km/s) or at a rotating wheel (Fizeau, 315,000 km/s) or rotating mirror (Foucault, 298,000 km/s). Trivium: nowadays the speed of light can be quite accurately measured in the brain of a person in a 7 T MRI scanner, by examining standing wave patterns or phase images.

[3] This was confirmed after Maxwells death by Heinrich Rudolf Hertz in 1887, who was the first to generate and detect electromagnetic waves.

2. Energy absorption and heating of the tissue is caused by the induced E-fields which are directly proportional to the frequency of the alternating B-field (see Equation 3). The consequences of this for 7T are briefly discussed in Section 1.4.

How and why these two phenomena are starting to be more important at a field strength as high as 7T is subject of the next two sections.

1.3 Why light is just not fast enough at 7 Tesla MRI

In this section it is clarified why light (or any other electromagnetic wave) can no longer be considered infinitely fast when going to 7T MRI. The EM-wave takes time to travel, and at 7T this goes too slow to ignore.

1.3.1 Wave interference

When exciting a tissue with conventional MRI, a transversal oscillating magnetic field (B_1^+) is generated, which excites the tissue if the frequency of this field is at the Larmor frequency f. The Larmor frequency is given by

$$f = \gamma \cdot B_0 \tag{7}$$

where γ is the gyromagnetic ratio and equals 42.58 Mhz/T for protons and B_0 is the field strength in T. Radio frequency (RF) coils are used to create this field, and since the propagation speed (the speed of light) is so fast, the phase of the oscillating field will be approximately equal throughout the object. Therefore, even when more RF sources are present at a certain location in the body, either by reflections or by an additional RF coil, the different waves will add up constructively. This approximation is no longer valid at a field strength of 7T. The speed of light is unchanged, but must be taken into consideration now, because the Larmor frequency increased to 298.2 MHz at 7T, resulting in a much smaller wavelength. Multiple RF sources, either by reflections or by an additional RF coil, will interfere like different wave sources in water, creating both constructive and destructive interferences. At 7T, this effect can cause black spots in the image at places where destructive interference took place.

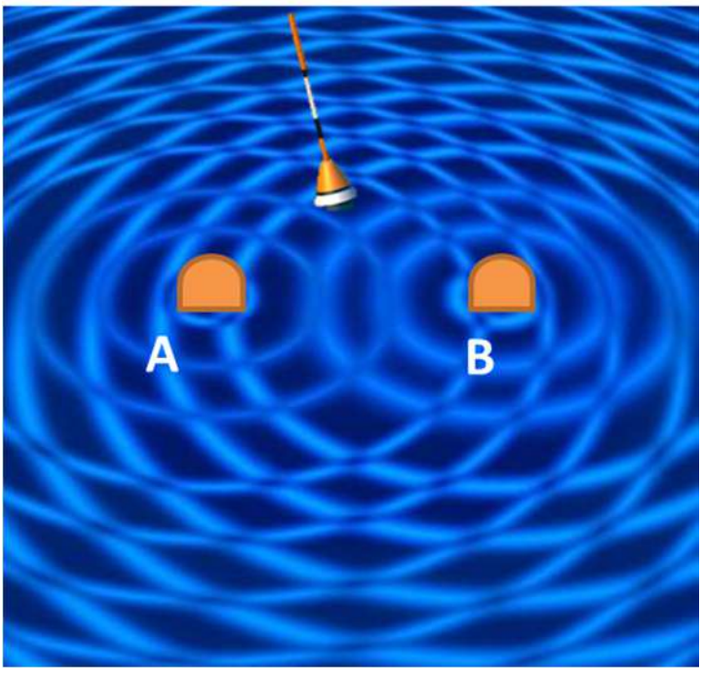

Figure 1.3 Interfering waves from two different wave sources A and B. The fishing float experiences the sum of the waves originating from both sources. Depending on the timing (relative phases) and height (amplitude) of each wave source, the waves will either add up or cancel out at the location of the fishing float.

1.3.2 RF shimming

Reflection of waves depends on the object geometry and boundaries and cannot be controlled when there is only one wave source. However, by adding one or more wave sources some level of control can be obtained. For example, looking at **Error! Reference source not found.**, by adjusting the phases and amplitudes of the two sources A and B, we can cause the fishing float either to oscillate with maximal amplitude, or to stand completely still in the water, by cancelling waves. In the same way the phases and amplitudes of the RF field of different RF coils can be adjusted in order to create maximum transverse magnetic field (B_1^+) at a certain location of interest. Optimizing for a single point in the object is therefore easy. Optimizing for multiple regions of interest, or a larger region of interest, is a bit more complicated. It requires trade-offs, in order to achieve an amplitude that is close to the desired amplitude at the whole region of interest. Determining optimal phases and amplitude for a desired B_1^+ field is called *RF shimming* (12). Better homogenization can be achieved when using more sources as long as the different sources have a certain level of independency from one other. RF shimming is a straightforward and efficient technique and is used in the upcoming chapters.

1.4 Why there is no(t yet a) standard setup at 7T

As mentioned earlier, another high field challenge is exposed by Faraday's law of induction (Equation 3). Research has been done on safety and tissue heating in MRI (13-15). Tissue heating is the consequence of an electric field in a dielectric medium. Induced currents are transformed into heat within the patient's tissue as a result of resistive losses. Equation 3 shows that the electric field is proportional to the frequency of the induced RF field. Consequently, in order to yield the same flip angle in an MR experiment (when using the same RF pulse length and B_1^+ amplitude), the increased frequency will cause a higher E-field and more tissue heating. Equivalently, the energy absorption by the tissue is bigger, causing more damping of the RF field.

As a consequence, a body volume coil is not feasible for RF transmission at 7T, since it will cause too much power to be absorbed by the subject in the scanner. Therefore more localized transmission coils are needed to avoid the MR sequences to be restricted by the specific absorption rate (SAR), a measure for tissue heating. Such coils are not commercially available for all body parts. During the development of more local transmission coils, the patient safety is most important. At 7 T, the SAR hotspots do no longer necessarily appear at the surface, but can appear in the middle of an objects by constructive interference of different E-fields (16, 17). Computer simulations need to be done and verified to predict the hotspots in a body for different transmit setups. SAR restrictions push the need for the development of specific sequences, that can work with restricted SAR as well as restricted reach of the local transmission coils.

Apart from the above mentioned *transmit coils*, needed to excite the tissue and create a flip angle, there are also the *receive coils*. Receive coils are needed to receive and record the echo's that are eventually transformed into an image. Receive coils are not sending out RF waves and therefore do not heat up the tissue like the transmit coils. Positioning of both transmit and receive coils therefor have different demands. The transmit coils are aimed at minimal SAR whereas the receive coils are aimed at maximal SNR.

1.5 Aims and layout of this research

The aim of this research was to develop methods to enable imaging of the carotid arteries at 7T, in order to eventually allow examining patients with atherosclerotic plaques around the bifurcation. The red line of this thesis is a setup of radiofrequent (RF) coils that were developed to reach the neck and the carotids. As discussed in the previous section, the integrated body transmit coil is not available at 7T. Instead, a standard commercially available head transmit coil does not reach the bifurcation of the carotid arteries with sufficient efficiency. Therefore, a coil setup had to be developed first. The previously discussed elements like wave interference and tissue heating had to be taken into account. This led to the development of a new conceptual multi transmit RF coil, a leaky waveguide transmitter, which is utilizing the challenging short wavelength phenomena's to

its own benefit. It was developed and tested in a phantom as well as *in-vivo*, and presented in **Chapter 2**. Together with the transmit coil a high density receiver array was developed dedicated to the neck region.

To assess the performance and to assess unknown magnetic parameters in the carotid artery at 7T, **Chapter 3** shows the results of a series of volunteers that was scanned at 3T and 7T. B_1^+ behavior and intrinsic SNR were evaluated and T_1 and T_2 relaxation times in the normal vessel wall were measured in the same group at both field strengths.

Additionally, the leaky waveguide transmitter made it possible to efficiently invert the blood in the carotid arteries, while imaging the brain with the standard head coil. This enabled whole brain arterial spin labelling, a technique to measure brain perfusion, which is quite well developed at lower field strengths, but still facing substantial challenges at 7T. In **Chapter 4** these challenges are discussed and it is shown how the new developed leaky waveguide transmitter realized a big step in brain perfusion measurements at 7T.

Chapter 5 discusses a challenge for 7T carotid MRI which is related to the absence of a body transmit coil: standard blood suppression techniques are not possible since they rely on blood preparation in the upstream artery, a region which cannot be covered by a local excitation coil. Chapter 5 gives a presentation of an explorative research to alternative blood suppression techniques that do not need the large coil coverage. Existing and new developed methods are evaluated on a phantom flow model.

Finally, in **Chapter 6**, the developed technology in the current state was tested on a series of patients with atherosclerotic plaques in the carotid arteries, including a first attempt to validate these results with histopathology. In the final **Chapter 7**, the results of this research are summarized and discussed.

References

1 **Davies PF, Remuzzi A, Gordon EJ, Dewey CF Jr, Gimbrone MA Jr** Turbulent fluid shear stress induces vascular endothelial cell turnover in vitro. Proc Natl Acad Sci USA 1986; 83: 2114–2117.

2 **Davies PF** Flow-mediated endothelial mechanotransduction. Physiol Rev 1995; 75:519–560

3 **Droste, DW, Dittrich, R, Kemeny, V, Schulte-Altedorneburg, G, Ringelstein, EB** (1999) Prevalence and frequency of microembolic signals in 105 patients with extracranial carotid artery occlusive disease. J of Neurology, Neurosurgery & Psychiatry, 67(4), 525–528

4 **Kerwin WS, Hatsukami T, Yuan C, et al** MRI of carotid atherosclerosis. AJR Am J Roentgenol. 2013;200: 304-313

5 **Yuan C, Mitsumori LM, Ferguson MS, et al** In vivo accuracy of multispectral magnetic resonance imaging for identifying lipid-rich necrotic cores and intraplaque hemorrhage in advanced human carotid plaques. Circulation. 2001;104:2051-2056

6 **Cai J, Hatsukami TS, Ferguson MS, et al** In vivo quantitative measurement of intact fibrous cap and lipid-rich necrotic core size in atherosclerotic carotid plaque: comparison of high-resolution, contrast-enhanced magnetic resonance Imaging and histology. Circulation. 2005;112:3437-3444

7 **Yuan C, Kerwin WS, Ferguson MS, et al** Contrast-enhanced high resolution MRI for atherosclerotic carotid artery tissue characterization. J Magn Reson Imaging. 2002;15:62-67.

8 **Underhill HR, Yarnykh VL, Hatsukami TS, et al** Carotid plaque morphology and composition: initial comparison between 1.5- and 3.0-T magnetic field strengths. Radiology. 2008;248:550-560

9 **Cappendijk VC, Heeneman S, Kessels AG, et al** Comparison of singlesequence T1w TFE MRI with multisequence MRI for the quantification of lipid-rich necrotic core in atherosclerotic plaque. J Magn Reson Imaging. 2008; 27: 1347-1355

10 **den Hartog AG, Bovens SM, Koning W, et al** Current status of clinical magnetic resonance imaging for plaque characterisation in patients with carotid artery stenosis. Eur J Vasc Endovasc Surg. 2013;45:7-21

11 **Naghavi M, Libby P, Falk E, et al** From vulnerable plaque to vulnerable patient: a call for new definitions and risk assessment strategies: Part I. Circulation 2003;108(14):1664-1672

12 **Metzger, GJ, Snyder, C, Akgun, C, Vaughan, T, Ugurbil, K, Van de Moortele, PF** Local B1+ shimming for prostate imaging with transceiver arrays at 7T based on subject-dependent transmit phase measurements. Magn Reson Med 2008, 59(2), 396–409

13 **Strilka, JS, Li, S, Martin, JT, et al** A numerical study of radiofrequency deposition in a spherical phantom using surface coils. Magn Reson Med 1998, 16(7), 787–798

14 **Hoult, DI, Phil, D** Sensitivity and power deposition in a high-field imaging experiment. JMRI 2000, 12(1), 46–67

15 **Vaughan, JT, Garwood, M, Collins, CM, Liu, W, DelaBarre, L, Adriany, G, Andersen, P, et al** 7T vs. 4T: RF power, homogeneity, and signal-to-noise comparison in head images. Magn Reson Med 2001, 46(1), 24–30

16 **Norris, DG** High Field Human Imaging. J Magn Reson Imaging 2003, 519–529

17 **Schick, F** Whole-body MRI at high field: technical limits and clinical potential. European radiology 2005, 15(5), 946–59

Chapter 2

High resolution MRI of the carotid arteries using a leaky waveguide transmitter and a high density receive array at 7 tesla

W. Koning, J.J. Bluemink, E.A.J. Langenhuizen, A.J. Raaijmakers,
A.E. Andreychenko, C.A.T. van den Berg, P.R. Luijten,
J.J.M. Zwanenburg, D.W.J. Klomp

*(*published in *Magnetic Resonance in Medicine,* 2013, PMID: 22760686*)*

Abstract

A setup for 7T MRI of the carotid arteries in the neck was designed and constructed. Separate dedicated arrays were used for transmit and receive. For the transmit array, single-side adapted dipole antennas were mounted on a dielectric pillow, which was shown to serve as a leaky waveguide, efficiently distributing B_1 into the neck. Risk assessment was performed by simulations. Phantom measurements were performed to establish optimal positions of the antennas on the pillow. Using two antennas, a dual transmit setup was created. In vivo B_1^+ maps with different shim configurations were acquired to assess transmit performance. This effective transmit array was used in combination with a dedicated 30 channel small element receive coil. High resolution in vivo turbo spin echo images were acquired to demonstrate the excellent performance of the setup

2.1 Introduction

The carotid arteries are the main arteries feeding the brain. A changed pattern in the blood flow distal and close to the bifurcation of the common carotid artery (CCA) into the internal and external carotid artery (ICA and ECA) can lead to atherosclerotic plaque formation. From these plaques emboli's can be shot towards the brain (1), which can lead to cerebrovascular stroke. Currently the clinical decision whether or not to intervene is mostly based on a combination of clinical symptoms and the degree of stenosis (2). However, it has been shown that no strong correlation exists between degree of stenosis and associated risk of stroke. Previous studies have indicated that plaque composition may provide a better assessment of the risk of stroke (3, 4). Characterization and quantification of specific plaque composition like fibrous-cap thickness (FCT), intraplaque hemorrhage (IH) and size of the lipid rich/necrotic core (LRNC) were shown to be important in this risk assessment (5). To correlate these characterizations with possible future clinical events it is important that they are imaged in as detailed a manner as possible. Although MRI of the plaques at 1.5 and 3.0T already provides detailed information on the plaque components (6, 7), the level of detail shown in histology (8, 9) cannot be met with MRI. Therefore, we explore the possibilities of imaging these plaques at 7T, under the assumption that higher level of detail may eventually result in an improved risk assessment.

Increasing the field strength in MRI implies dealing with shorter wavelengths of the radio frequency (RF) electromagnetic (EM) waves. At a field strength as high as 7 tesla the challenges associated with these short wavelengths become severe. First, interferences of RF waves cause inhomogeneous amplitudes of RF transmit (B_1^+) fields. Second, decreased RF penetration results in lower B_1 efficiency. And finally, increased RF power deposition will cause higher levels of specific absorption rates (SAR). B_1 inhomogeneities degrade the image quality while increased SAR levels can significantly decrease the degrees of freedom in designing pulse sequences for clinical imaging (10). These RF challenges also impede the use of a body coil, hence more local coils may be required for excitation, which allow excitation within the SAR limits, but at the cost of further decreased B_1^+ homogeneity.

Despite these challenges, imaging of the brain at 7T gives already promising results. For example, higher resolutions and increased sensitivity e.g. to magnetic susceptibility weighted contrast yield in an increased sensitivity in detecting white matter lesions compared to 3T (11). Local transmission (e.g. a birdcage head coil) combined with multi-element receive arrays results in efficient and relatively low SAR excitation together with high SNR reception with parallel acceleration potential. However, the birdcage volume coil that is the current standard for transmission in brain imaging at 7 tesla, is not able to deliver a strong enough B_1 field in the neck region without exposing the brain to intolerably high SAR levels. Using local transceiver coils, some potential of 7T MRI for the carotid arteries was recently shown by Kraff et al. (12). However, transceiver coils are subject to a trade-off between local SAR and SNR. Closely positioned coils are

beneficial for the receive sensitivity but result in higher local SAR. More distant positioned coils cause less local SAR, but are less sensitive in receiving. Here we introduce a new setup for carotid artery imaging at 7T MRI that uses separate local transmit and receive arrays. For the receive array, two high density element arrays (15 coil elements per side) were designed similar to that presented by Petridou et al (13). A novel 2-channel transmit array was designed, making use of radiative antennas (14). The region of interest, the carotid bifurcation, is located at the height of the neck and jaw. Because this is a very irregular surface with a high inter person shape variability, the antennas presented here, being rigid themselves, were mounted on a flexible neck pillow filled with deuterium oxide as a dielectric substrate. This assures a constant filling factor of the antennas and a good dielectric connection between pillow and neck. This good connection, in turn, enables an efficient transmission of the electromagnetic (EM) wave from the pillow into the neck, as long as the permittivity of the substrate and the neck are matched. Local electric field hotspots occur in the lossless dielectric pillow, making this setup efficient in terms of B_1 per local SAR in the tissue. In this paper the setup is described, both for the receive and transmit parts, the safety is addressed by means of simulations, the B_1 efficiency is evaluated and the feasibility of this setup is finally demonstrated by high resolution carotid artery imaging in vivo.

2.2 Methods

2.2.1 Receive array

For signal reception two 15 element receiver arrays were constructed, one for each side of the neck. Each of the 30 individual receiver elements was tuned to 298.2MHz and matched to a real impedance of 50 ohm. The receiver elements are elliptically shaped with outer dimensions of the ellipse of 15 x 35mm^2 (Figure 2.1a). Figure 2.1b shows the resonant circuit of the element. A PIN diode was used to detune the circuit during transmit, allowing for the use in combination with high-power transmit fields at 7T. Preamplifier decoupling was applied by using proper cable-lengths between the elements and low impedance preamplifiers, which were interfaced to the MR system (Nova medical, Massachusetts, USA).

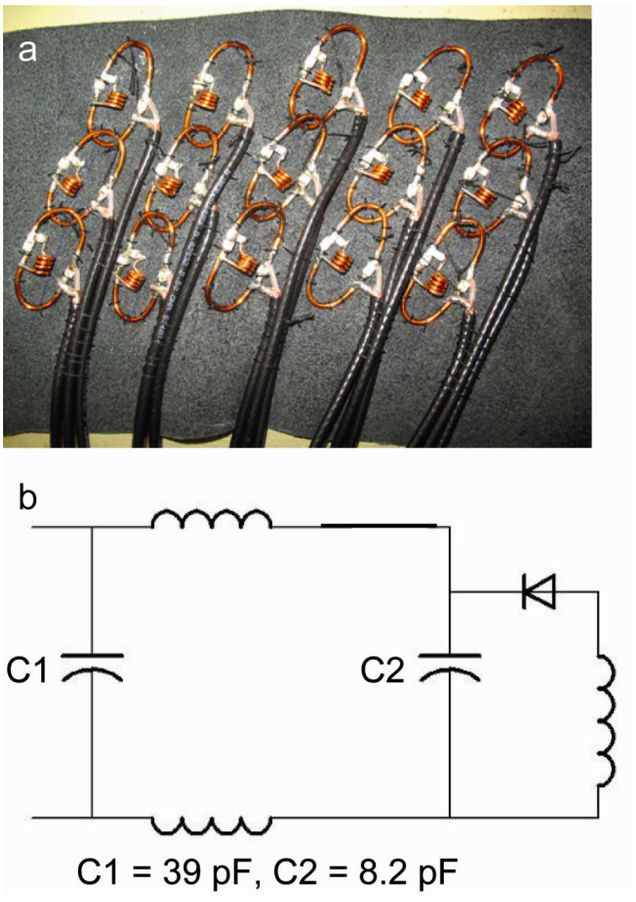

Figure 2.1 One of the two 15 channel receiver coil arrays: (a) photo of a 15 channel receiver coil arrays, consisting of 5 modules of 3 loop coils. The coils have a 4 mm overlap in the longitudinal direction (which is to be placed in B_0 direction) and the transversal spacing between the modules is 28mm. (b) shows the circuitry of a single loop element.

Each of the two 15 element arrays consists of 5 modules of 3 receiver elements. Each module of three elements shares a common cable trap. The spacing between the separate modules is 28mm in transverse direction to achieve sufficient spatial coverage, and the three elements within a single module have a 4mm mutual overlap in longitudinal direction to prevent signal absence. Together with the preamplifier decoupling this was sufficient for decoupling. The modules were mounted together on flexible fabric with total dimensions 10 x 15cm^2 (Figure 2.1a), allowing all modules to be placed closely to the neck and all coil elements to be properly loaded.

2.2.2 Transmit array

Radiative antennas, similar to the antennas proposed by Raaijmakers et al (14), were used for transmit, each driven by a 4kW amplifier. Each element consisted of a C-shaped $^1/_2\,\lambda$ dipole antenna (Figure 2.2a). The dipole was formed by two copper strips of dimensions 25 x 60mm^2. The total length of the C-shaped dipole was 125mm. The copper strips were attached to a

C-shaped glass fiber mould with an extra 2mm layer of polyester resin for extra stiffness. The antennas were tuned and matched to 50 - by a matching network consisting of a single capacitor of 13.8pF in parallel between the two antenna strips (Figure 2.2d). The antennas were fed via a single cable trap and mounted on a U-shaped pillow (Figure 2.2b and c) The outer dimensions of the pillow are 30 x 22cm, with a tube radius of 5cm average. The pillow was filled with 99.9% deuterium oxide as a dielectric medium. The flexibility of the pillow allowed necks of different sizes and shapes to fit in. The medium deuterium oxide has a dielectric permittivity of 78 and a low conductivity in the order of 10^{-5} S/m.

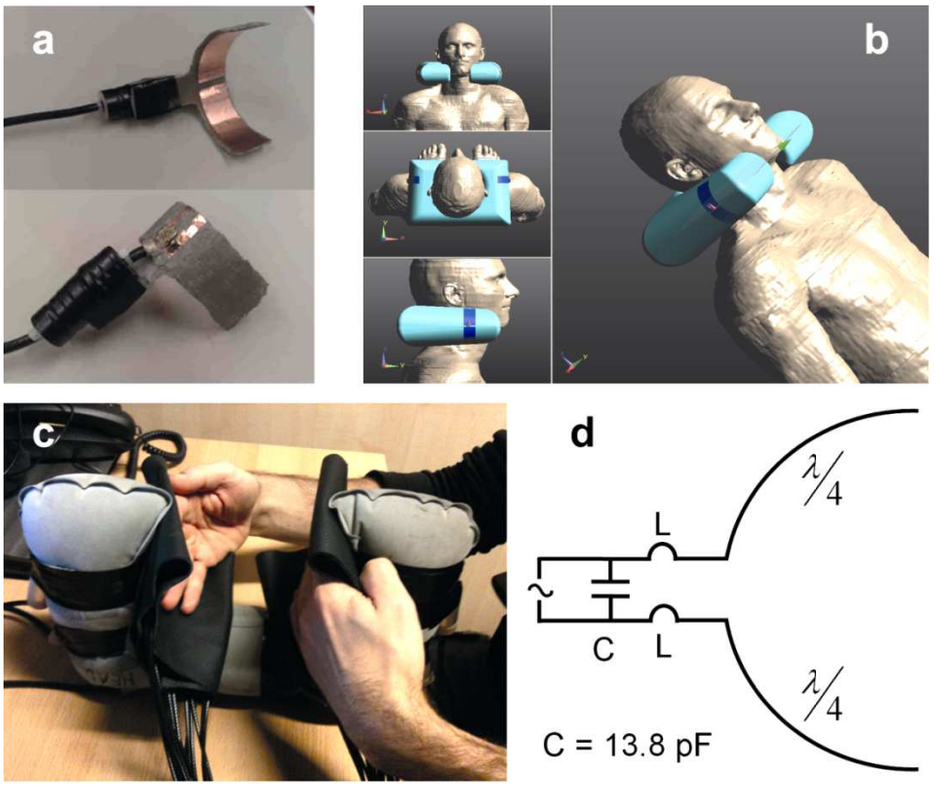

Figure 2.2 Designed transmit array: (a) The C-shaped dipole antenna. (b) Schematic overview of the transmit setup as used in the simulations (SEMCAD X64 v14.2 Speag, Zurich, Switzerland). (c) The antennas mounted on the U-shaped pillow together with two 15 channel receiver arrays, and (d) a schematic circuit of the antenna (L = 2 cm leads).

To ensure RF safety, temperature validated (15) FDTD (Finite Difference Time Domain) simulations were performed (SEMCAD X64 v14.2 Speag, Zurich, Switzerland) with the adult male human model from the virtual family (16). Intensities and positions of the maxima of local 10 gram averaged SAR_{10g} (W/kg) normalized to 1W power delivered at the antenna were obtained, and all experiments were assured to remain within SAR safety guidelines of 10W/kg of local SAR_{10g} (17).

2.2.3 Experiments

All experiments were performed on a 7T whole body MRI scanner (Achieva 7.0T, Philips Healthcare, Cleveland, USA). For phantom experiments a plastic bottle with a cross section of 10 x 15cm^2 was used, filled with a solution of 3.0 g/l NaCl dissolved in tap water to obtain a loading similar to a human neck. For all experiments the two 15 element receiver arrays were positioned between the pillow and the neck or phantom (Figure 2.2b). The ratio $Q_{loaded}/Q_{unloaded}$ of each of the individual receiver elements was determined with a network analyzer (Agilent, USA), where Q_{loaded} was determined on the neck of a healthy volunteer. Noise images were acquired with each element and correlation between the noise images of all receiver elements was determined both with and without the presence of the transmit elements. Acceleration performance in AP and HF direction was assessed by calculating 2D g-factor maps for acceleration factors of 2 to 8 per direction. To acquire the acceleration performance for the target area of this setup, the carotid arteries, the average g-factor over 4 ROI's was calculated. The ROI was located in the neck at depths of 1.0, 2.0, 3.0 and 4.0cm respectively. The surface of the ROI's used was 5.0cm^2, and shown in Figure 2.4.

To investigate the dependence of the B_1^+ profiles on the positioning of the antennas on the dielectric pillow, 6 B_1^+ maps (Bloch-Siegert B_1^+ map (18), 4kHz off-resonance pulse of 4ms duration, TR = 1000ms) were acquired on the phantom for different antenna positions. Each of the six B_1^+ maps was acquired with a single antenna present. Based on these B_1^+ profiles, two antenna positions were selected for optimal excitation of the carotid artery regions on both sides of the neck. On these two positions two antennas were mounted on the pillow for the in vivo experiments and driven by two 4kW amplifiers. Coupling (S_{12}) between the two antennas was measured with a network analyzer. In vivo B_1^+ maps of both antennas transmitting individually as well as simultaneously, were acquired in a healthy volunteer, for three orthogonal orientations to demonstrate the coverage of the transmit array (B_1^+ map: AFI method (19), $T_{R,1}/T_{R,2}$ = 25/125ms, nominal flip angle (fa): 50º, 3D gradient echo (GE), 220 x 220 x 55mm^3). Using a dual transmit setup, phase and amplitude could be set separately for both channels, allowing for RF phase shimming to maximize the B_1^+ at the carotid artery on the side of interest, or phase and amplitude shimming to provide the same high B_1^+ at both sides. In this study only phase shimming was performed. Therefore, a fast GE phase map (T_{acq} = 5s) was acquired for both channels. In the region of interest the phase difference between the two channels was measured and compensated for in all following scans. The whole procedure takes about two minutes. Finally, high resolution T2W turbo spin echo images were acquired, with the following scan parameters: multi slice turbo spin echo (TSE), T_R/T_E = 3000/43ms, number of slices = 12, turbofactor = 7 (excluding 3 startup echos), refocusing angles = 80º, voxel size = 0.4 x 0.4 x 1.5mm^3 Fat suppression was performed by chemical shift selective excitation on the fat resonance and crushing of these signals with gradients. In order to obtain optimal signal combination of all receiver elements, complex coil sensitivity profiles were measured enabling amplitude weighting

and phasing of the receive channels, or to unfold the sense encoding. This reference scan was acquired using once reception of all receiver elements, and once only one of the two transmit antennas as receiver, while maintaining the same transmit fields. All volunteers in the study signed an informed consent according to the guidelines of the institution.

2.3 Results

2.3.1 Receive

The mean unloaded Q for the receive elements was found to be 330. Mean loaded Q was 22, resulting in a mean ratio $Q_{unloaded}/Q_{loaded}$ of 15. Figure 2.3 Noise correlation between all 30 receive elements acquired with two transmit antennas present. shows the correlation between the received noise of all elements in the presence of the transmit antennas. There was no effect of the presence of the transmit elements, as the noise correlation between the elements of a single 15 channel array was virtually equal when the transmit elements were present (-13.2dB on average) and when the transmit elements were absent (-12.8dB on average).

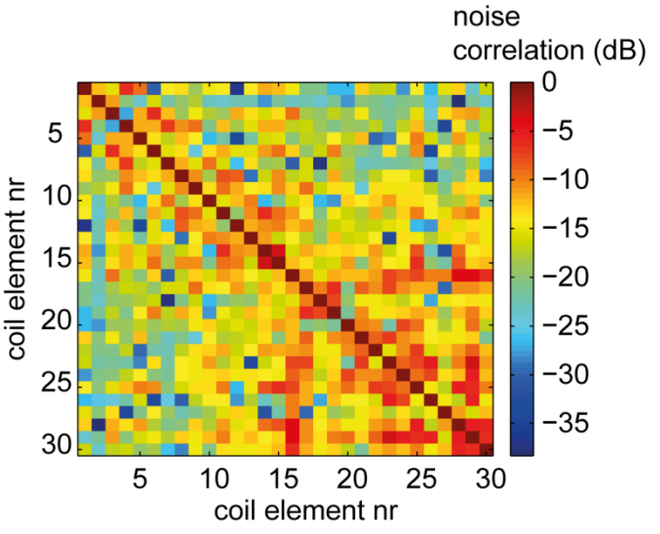

Figure 2.3 Noise correlation between all 30 receive elements acquired with two transmit antennas present.

In Figure 2.4 the g-factor maps are shown for acceleration in the AP direction (Figure 2.4a) and in the HF direction (Figure 2.4b), for SENSE acceleration factors of 2, 3, 4 and 5. Figure 2.5 shows the g-factor for different depths. Considering the carotid bifurcation to be at an average depth of 3cm, an ROI at that distance gave an average g-factor of 1.15 $\pm$ 0.07 in the AP direction and 1.14 $\pm$ 0.08 in the HF-direction.

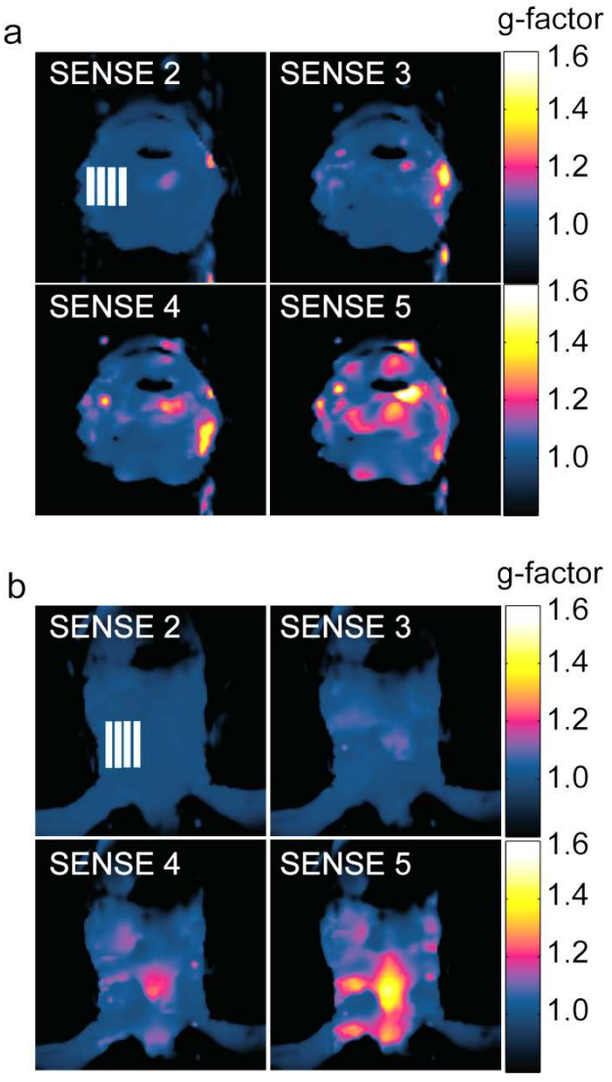

Figure 2.4 g-factor maps, (a) transverse g-maps in the neck with acceleration in AP-direction and (b) coronal g-maps in the neck with acceleration in HF-direction.

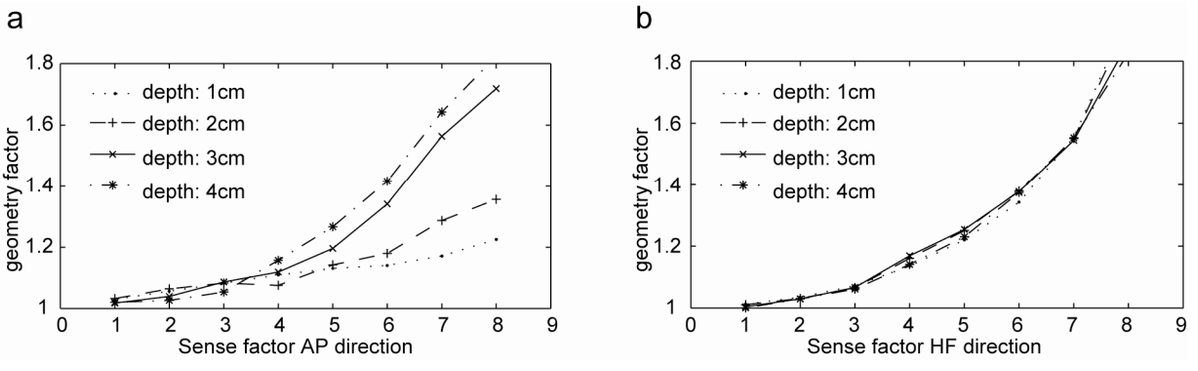

Figure 2.5 g-factor averaged over an area of interest at depths of 1.0, 2.0, 3.0 and 4.0 cm, for acceleration in (a) AP- and (b) FH-direction. The four regions of interest used for this quantification are annotated in Figure 2.4.

2.3.2 Transmit

Figure 2.6 shows the resulting B_1^+ maps in the phantom (normalized to 1W power at the antennas) for different positions/orientations of the antennas on the pillow. Position 3 and 6 delivered the most B_1^+ in the target regions, so these positions were chosen for the in vivo experiments. Coupling between these two elements was always less than -15 dB (S12 $<$ -15 dB). The elements were driven by two 4 kW RF amplifiers, the output of which had a loss of 50% in the cables and the connectors between amplifier and transmit elements. For further SAR calculations it was assumed that none of the remaining power was absorbed by the antenna itself.

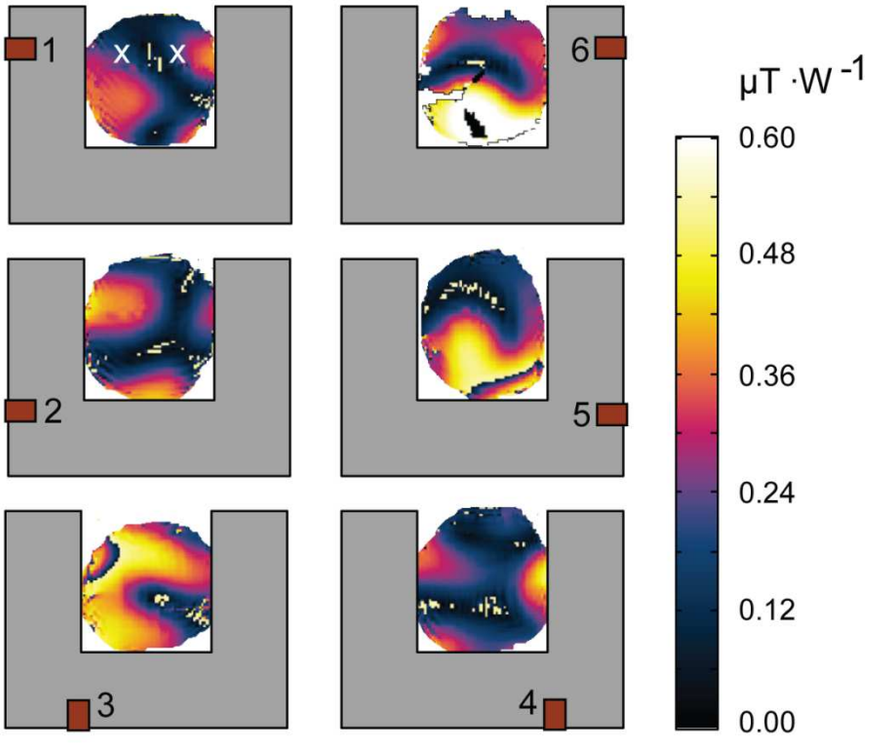

Figure 2.6 B_1^+ amplitude maps in a neck-shaped phantom. In each of the 6 B1+ maps the antenna is placed at a different position. Every position results in a different B1+ pattern. In the first image, the two white crosses point out an approximate average position of the carotids.

Figure 2.7 shows the SAR distribution averaged over 10g (SAR_{10g}) of tissue for each of the two channels separately. A maximum normalized SAR_{10g} of 1.99W·kg^{-1}·W^{-1} for one channel was found, with the hotspot located at the left side of the neck. The antenna at the back of the neck results in a lower SAR_{10g} hotspot of 1.75W·kg^{-1}·W^{-1}. Simulations of the two antennas transmitting simultaneously, resulted in hotspots that did not exceed the single element values by more than

50% (ranging from 0 to 50% using different settings for the RF phase between the two transmit channels).

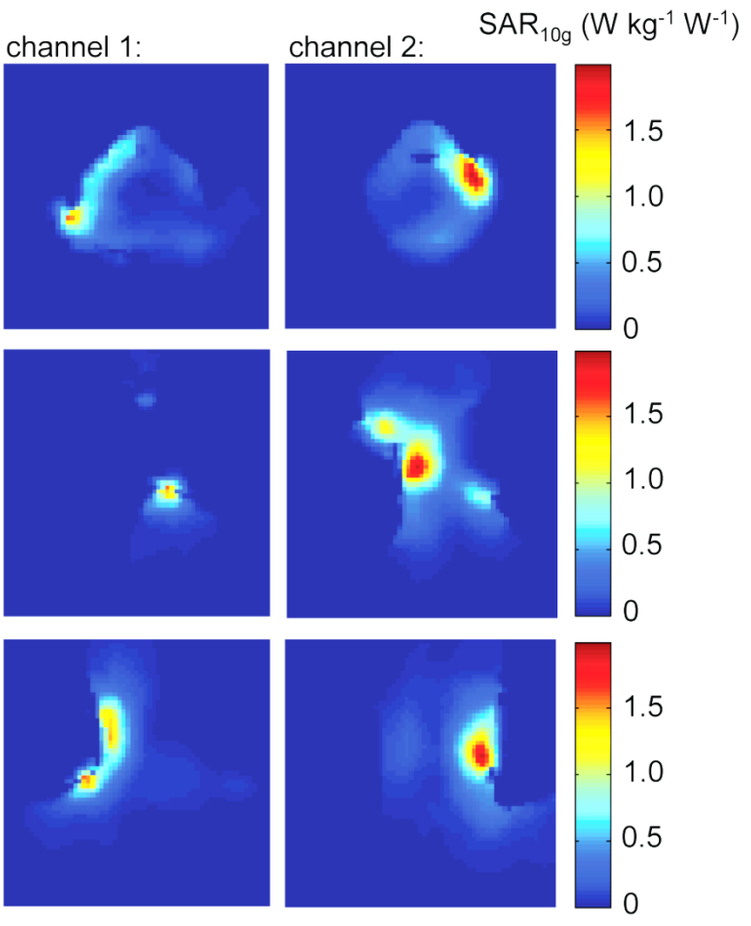

Figure 2.7 Simulations of the antennas on the dielectric medium with SEMCAD X64 v14.2 Speag, Zurich, Switzerland (a) SAR hotspots from the antenna at position 3, (b) SAR hotspots from the antenna at position 6 (positioning see Figure 2.6).

Figure 2.8b and c shows the in vivo B_1^+ maps acquired with each separate antenna in three orthogonal orientations. Figure 2.8 shows also two different shim configurations, one focused on the left carotid artery (Figure 2.8d) and one focused on the spine (Figure 2.8e).

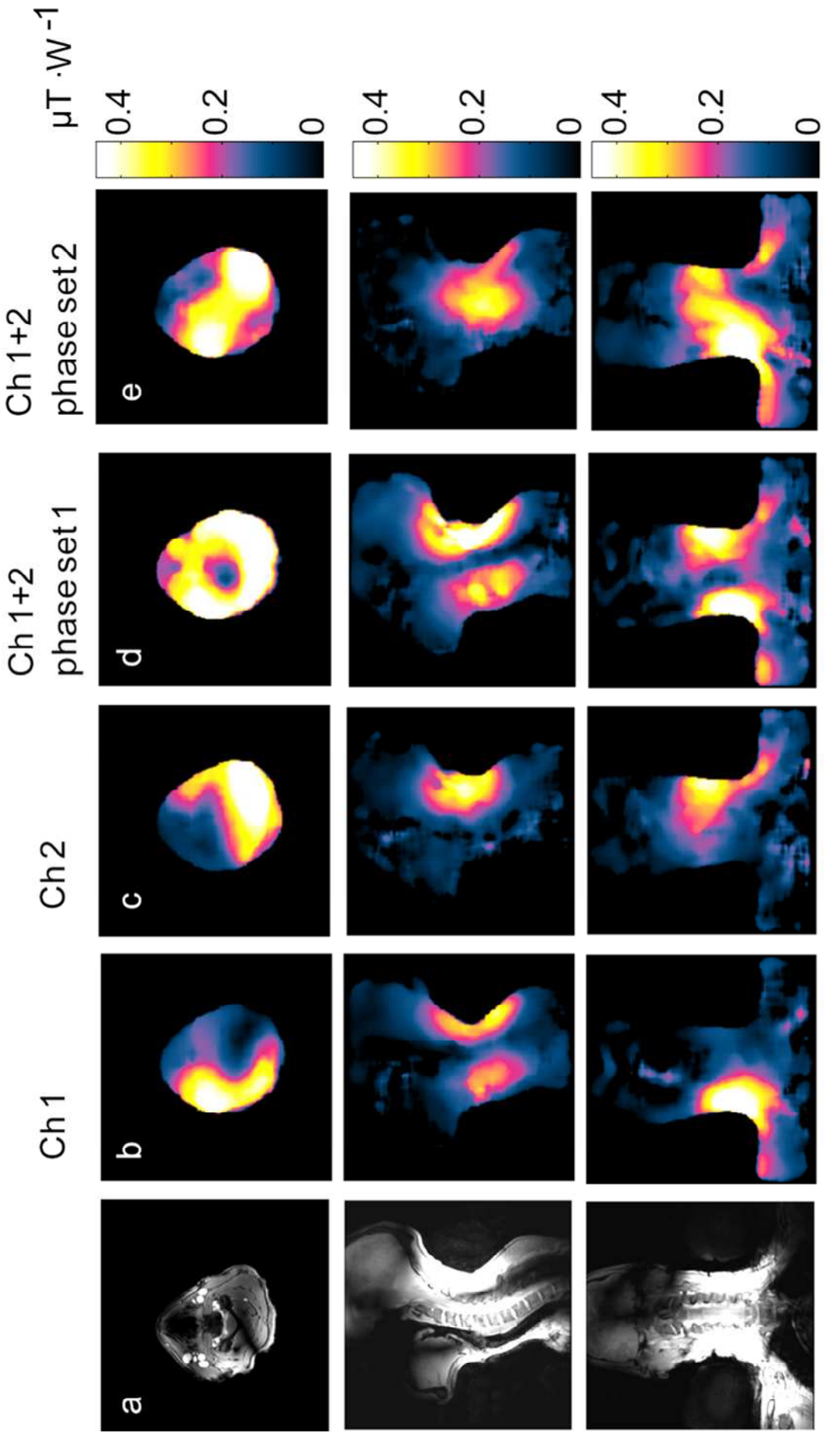

Figure 2.8 B1+ maps acquired in vivo with two antennas, (a) anatomical reference images in transversal, sagital resp. coronal direction. (b) corresponding B_1^+ maps acquired while transmitting with channel 1, (c) corresponding B_1^+ maps while transmitting with channel 2. (d) and (e) show B_1^+ maps acquired while transmitting with both channels simultaneously, and forced by phase adjustment to constructively interfere at the left carotid artery (d) and at the spine (e) Axes are clipped at 0.45 $\mu T\ W^{-1}$, which corresponds to a B_1^+ amplitude of 20μT for a delivered power of 2kW.

The potential of the setup for in vivo imaging is demonstrated in Figure 2.9. The high in-plane resolution together with the high SNR lead to a sharp and clear depiction of the carotid vessel wall and the bifurcation.

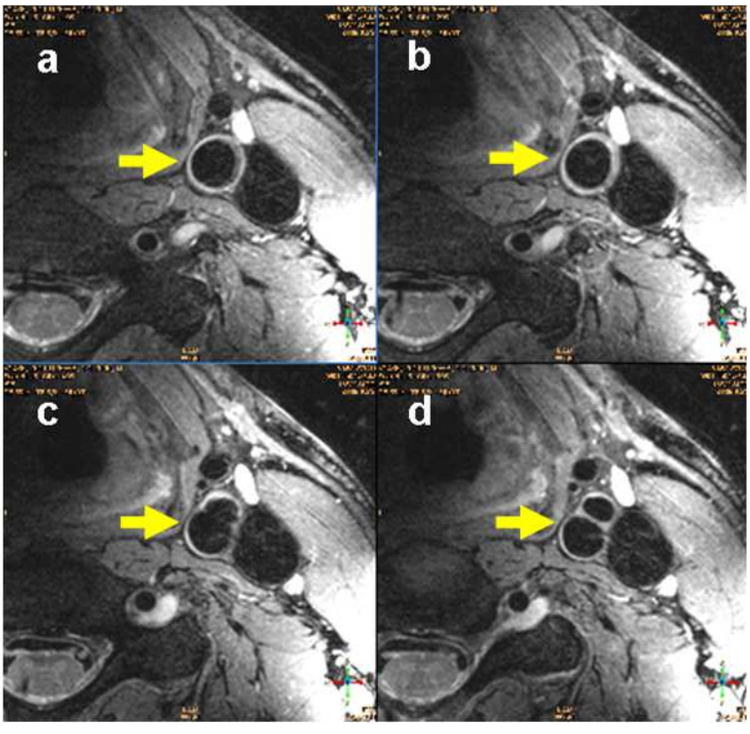

Figure 2.9 Transveral TSE images of the neck showing the bifurcation indicated by the yellow arrow. From (a) to (d) slices are ascending in FH direction. Resolution: 0.4 x 0.4 mm2, slice thickness: 1.5 mm, TR/TE: 3000/120ms, Turbo factor: 7, echo spacing / shot length: 30.1/210ms, refocusing angle: 80o.

2.4 Discussion and conclusion

A setup for MR imaging in the neck region was designed and created. To avoid a compromise between SAR and SNR, separate arrays for transmission and reception were constructed, which to the best of our knowledge has not been reported before for this application at 7T. The performance of this setup was demonstrated by showing good B1 performance and the excellent reception performance and acceleration potential. This resulted in clinically relevant sequences that could be applied within SAR constraints, which yielded in high-resolution in vivo images of the carotid vessel wall.

The relatively large number of small elements in the receive arrays could potentially cause additional noise as compared to a single optimized RF coil. However, the measured Q-ratio (unloaded/loaded) of 15 shows that this additional noise is negligible compared to the noise introduced by the sample itself (20), reflecting good coupling to the tissue. An important factor in favour of such a multi element coil is the positioning. Closely positioned receiver coils ensure

maximal receive sensitivity. However, positioning becomes quite critical when a single optimal sized (21) coil is used for this, particularly for imaging the carotid artery. Using this multi element array, a proper reference scan that obtains the sensitivity profiles for the coils ensures that each pixel in space is obtained with optimal SNR. This provides an optimal combination in a range of locations, hence resulting in a more robust positioning compared to a single optimal sized receive coil, as was also demonstrated in (22). On top of this, the large amount of elements allows for very high acceleration factors for parallel imaging. It was shown that up to an acceleration factor of 4, the g-factor easily remains within acceptable values ($<$1.3) in the carotid artery region, for acceleration in AP as well as in FH direction (Figure 2.4 and Figure 2.5). The high possible acceleration factors can also be beneficial when motion artefacts (e.g. by swallowing) must be avoided. The anatomical images shown in Figure 2.9 Transveral TSE images of the neck showing the bifurcation indicated by the yellow arrow. From (a) to (d) slices are ascending in FH direction. Resolution: 0.4 x 0.4 mm2, slice thickness: 1.5 mm, TR/TE: 3000/120ms, Turbo factor: 7, echo spacing / shot length: 30.1/210ms, refocusing angle: 80o., show that the high receive sensitivity in combination with the gain in intrinsic SNR due to the high field strength can be utilized to acquire MRI with voxel sizes of 0.4 x 0.4 x 1.5mm^3 = 0.24mm^3. For the multi slice sequence used, this was found to be the smallest voxel volume that still yielded sufficient SNR. Minimal voxel volumes that can be used at 3T are around 0.58 mm^3 (23) or 0.50mm^3 (24), currently. The TSE images are acquired without triggering. Consequently, in Figure 2.9 Transveral TSE images of the neck showing the bifurcation indicated by the yellow arrow. From (a) to (d) slices are ascending in FH direction. Resolution: 0.4 x 0.4 mm2, slice thickness: 1.5 mm, TR/TE: 3000/120ms, Turbo factor: 7, echo spacing / shot length: 30.1/210ms, refocusing angle: 80o.c pulsation artefacts can be seen. In the future, a combination of 3D acquisition schemes together with sophisticated motion compensation and the current coil setup, could allow for even smaller voxel volumes with sufficient SNR.

The transmit elements are attached to a tube that contained a medium with a permittivity (ε = 78) higher than that of air ($\varepsilon_{air} = 1$). The high permittivity of the medium allows for feasible antenna sizes that fit the geometric boundaries of a neck pillow. In addition, the permittivity in the pillow being closer to tissue ($\varepsilon \approx 50$) than to air, causes signal leakage into air to be much lower than signal transmission into the tissue. The conductivity of the used D_2O is close to zero, providing minimal dielectric losses. As a consequence, a comfortable liquid filled pillow can be used with antennas that can generate a strong B1 field efficiently. In addition, the geometry of the transmit array allowed for receiver arrays that did not require any compromise on their geometrical design. Because of the pillow, the capacitors in the antennas are always at more than 5cm distance from the nearest tissue, therefore the high E-fields around the capacitors do not directly cause local SAR hotspots in the tissue. Since the locations of highest power deposition are substantially different for the two antennas (Figure 2.7), the antennas can be driven with a total of twice as much RF power, while SAR increases with only 0 to 50%, depending on the phase setting. As the maximum local SAR remains outside the human head, the safety guidelines are less conservative and allow

for a local SAR of 10W/kg. The images in Figure 2.9 were acquired far within the SAR limitations following from these values.

Looking at the B_1^+ maps at different locations shown in Figure 2.6, a clear asymmetry is shown between the symmetrically aligned antennas (position 1 versus 6, 2 versus 5, and 3 versus 4).. While two opposing antennas with symmetrical geometries, have symmetrical B1 patterns, the measured and simulated B_1^+ patterns are far from symmetrical (i.e. B_1^+ and B_1^- maps of the transmit antennas are not equal). Although spatial B_1^+ asymmetries have been observed at high fields before (21), the origin of the asymmetric behavior may be different with the transmit setup presented here. A circular or elliptical polarized local B_1 is a superposition of linear B_1 fields with different angular orientation and phases, e.g. by originating from different located sources, as is commonly facilitated in quadrature setups. The presence of these highly pronounced asymmetric patterns implies the EM wave is propagating through the pillow, and enters the neck from different locations and with different phases. Dependent on the position in the neck and the dominant direction of the traveling wave in the pillow, these waves of different phase and orientation create mixed polarization patterns, and therefore add to the asymmetry of the B_1^+ (and the B_1^-) field. This effect can be appreciated in the B_1^+ fields observed with the antenna positioned at the top of the pillow (Figure 2.6, antenna position 1). Hardly any B_1^+ is obtained close to the antenna, while counter clockwise with the pillow, high B_1^+ fields are observed, indeed suggesting a propagating wave inside the pillow, where the pillow acts as a dielectric waveguide. To allow for a propagation of a wave the RF frequency must be above the cut-off frequency (25). At our frequency (300 MHz) this corresponds to a certain minimal cross-sectional dimension for which wave propagation of the mode with the lowest cut-off frequency (TE_{01} mode) is possible. Equation (1) shows the governing equation that defines the lower limit of the dimension of an open cylindrical waveguide that allows wave propagation:

$$a > \frac{u_{n,m} \cdot \lambda}{2\pi\sqrt{n_{water}^2 - n_{air}^2}} \qquad (1)$$

With refractive index $n = \sqrt{\varepsilon_r \cdot \mu_0}$ and wavelength in water deuterium λ. The possible values $u_{n,m}$ are the mth roots of the nth order Bessel functions describing the wave propagation modes (25). For the first possible mode $u_{n,m} = 2.4048$, with $\varepsilon_{r,water} = 78$, $\varepsilon_r \approx 1$ and $\mu_0 = 4\pi \cdot 10^{-7}$, it follows from Equation (1) that indeed a wave (TE_{01} mode) will propagate in the dielectric pillow if the radius a exceeds 4.4 cm. This condition is fulfilled with the dimensions of the pillow. So, the pillow indeed allows for propagation of waves at 300 MHz in water. The dielectric pillow therefore seems to function as a leaky waveguide, distributing the B_1 into the neck from all sides with a phase delay. This is a difference to the radiative antennas presented in (14), where the wave enters the body only from one direction, resulting in a more linearly polarized B_1 field. The fact that the B_1^+ varies with the position of the antenna, will facilitate homogenizing the B_1^+ field by phase and amplitude shimming, as well as the use of techniques like transmit Sense (26) once

more antennas are used simultaneously. In this research only two channels were used simultaneously and their B_1^+ fields were focused on the region of interest by phase shimming. The two shim configurations shown in Figure 2.8 show the versatility of the setup, that can be used to focus the B_1^+ on the spine (Figure 2.8e) or on the carotids (Figure 2.8d).

No significant difference between noise correlation with and without transmit antennas was observed. This means no additional decoupling circuit is required to detune the transmit antenna's during reception. On top of this, tuning and matching of the antennas is independent of neck shapes, since the waveguide averages out the variability of the load between different necks experienced by an antenna. To conclude: a 2-channel radiative transmit array was designed and constructed. Antennas were used in combination with a dielectric neck pillow filled with D_2O to distribute the B_1 in the neck. The neck pillow was shown to act as a leaky waveguide. Even though the design of the pillow for this transmit setup can still be optimized by using more transmit antennas and exploring different geometries, the resulting B_1^+ patterns were already sufficient to be used for imaging the carotid arteries. Combined with a dedicated 30-channel small element receive coil a TSE sequence could be implemented to show that 7T can be used for clinical high spatial resolution imaging to asses carotid vessel wall integrity.

References

1 **Siebler M, Sitzer M, Steinmetz H** Detection of intracranial emboli in patients with symptomatic extracranial carotid artery disease. Stroke 1992; 23(11):1652-1654.

2 **Rothwell PM, Eliasziw M, Gutnikov SA, Fox AJ, Taylor DW, Mayberg MR, Warlow CP, Barnett HJ** Analysis of pooled data from the randomised controlled trials of endarterectomy for symptomatic carotid stenosis. Lancet. 2003; 361(9352):107-16.

3 **Naghavi M, Libby P, Falk E, Casscells SW, Litovsky S, Rumberger J, et al** From vulnerable plaque to vulnerable patient: a call for new definitions and risk assessment strategies: Part I. Circulation 2003; 108(14):1664-1672.

4 **Falk E.** Why do plaques rupture? Circulation 1992; 86(6 Suppl):III30-42.

5 **Takaya N, Yuan C, Chu B, Saam T, Underhill H, Cai J, Tran N, Polissar NL, Isaac C, Ferguson MS, Garden GA, Cramer SC, Maravilla KR, Hashimoto B, Hatsukami TS** Association between carotid plaque characteristics and subsequent ischemic cerebrovascular events: a prospective assessment with MRI - initial results. Stroke 2006;37(3):818-23.

6 **Saam T, Ferguson MS, Yarnykh VL, Takaya N, Xu D, Polissar NL, Hatsukami TS, Yuan C** Quantitative evaluation of carotid plaque composition by in vivo MRI. Arterioscler Thromb Vasc Biol. 2005; 25(1):234-9.

7 **Hatsukami TS, Yuan C.** MRI in the early identification and classification of high-risk atherosclerotic carotid plaques. Imaging Med. 2010;2(1):63-75.

8 **Watanabe Y, Nagayama M, Suga T, Yoshida K, Yamagata S, Okumura A, Amoh Y, Nakashita S, Van Cauteren M, Dodo Y** Characterization of atherosclerotic plaque of carotid arteries with histopathological correlation: vascular wall MR imaging vs. color Doppler ultrasonography (US). Magn Reson Imaging 2008;28(2):478-85.

9 **Lovet, J.K.; Redgrave, J.N.E.; Rothwell PM** A Critical Appraisal of the Performance, Reporting, and Interpretation of Studies Comparing Carotid Plaque Imaging With Histology. Stroke 2005;36:1085-1091.

10 **Norris DG** High Field Human Imaging. J Magn Reson Imaging. 2003;18(5): 519-29.

11 **Tallantyre EC, Morgan PS, Dixon JE, Al-Radaideh A, Brookes MJ, Evangelou N, Morris PG** A Comparison of 3T and 7T in the Detection of Small Parenchymal Veins Within MS Lesions. Investigative Radiology 2009; 44(9):491-494.

12 **Kraff O, Bitz AK, Breyer T, Kruszona S, Maderwald S, Brote I, Gizewski ER, Ladd ME, Quick HH** A transmit/receive radiofrequency array for imaging the carotid arteries at 7 Tesla: coil design and first in vivo results. Investigative Radiology 2011;46(4):246-54.

13 **Petridou N, Italiaander M, Bank BVD, Siero J, Hoogduin J, Luijten P, Klomp D** Enhancing fMRI sensitivity at 7T with a modular 16-channel small element surface coil. Proceedings of the 18th Annual Meeting of ISMRM, Stockholm, Sweden, 2010.

14 **Raaijmakers AJE, Ipek O, Klomp DWJ, Possanzini C, Harvey PR, Lagendijk JJW, van den Berg CAT** Design of a radiative surface coil array element at 7 T: The single-side adapted dipole antenna. Magn Reson Med. 2011 Nov;66(5):1488-97.

15 **Bergen BVD, Klomp DWJ, Raaijmakers AJE, Arteaga C, Castro D, Boer VO, Kroeze H, Luijten R, Lagendijk JJW, van den Berg CAT** Uniform prostate imaging and spectroscopy at 7 T: comparison between a microstrip array and an endorectal coil. NMR in Biomed 2011; 24: 358-365.

16 **Christ A, Kainz W, Hahn EG, Honegger K, Zefferer M, Neufeld E, Rascher W, Janka R, Bautz W, Chen J, Kiefer B, Schmitt P, Hollenbach HP, Shen J, Oberle M, Szczerba D, Kam A, Guag JW, Kuster N** The Virtual Family - development of surface-based anatomical models of two adults and two children for dosimetric simulations. Phys Med Biol. 2010 Jan 21;55(2):N23-38.

17 The International Commission on Non-Ionizing Radiation Protection. Medical Magnetic Resonance (MR) Procedures: Protection of patients. Health Physics. 2004;87(2):197-216.

18 **Sacolick LI, Wiesinger F, Hancu I, Vogel MW** B1 mapping by Bloch-Siegert shift. Magn Reson Med. 2010;63(5):1315-22.

19 **Yarnykh VL** Actual flip-angle imaging in the pulsed steady state: a method for rapid three-dimensional mapping of the transmitted radiofrequency field. Magn Reson Med. 2007;57(1):192-200.

20 **Kumar A, Edelstein WA, Bottomley PA** Noise figure limits for circular loop MR coils. Magn Reson Med. 2009;61(5):1201-9.

21 **Hoult DI, Phil D** Sensitivity and power deposition in a high-field imaging experiment. J Magn Reson Imaging. 2000;12(1):46-67.

22 **Hadley JR, Roberts JA, Goodrich KC, Buswell HR, Parker DL** Relative RF coil performance in carotid imaging. Magn Reson Imaging. 2005;23(5):629-39.

23 **Zhao X, Miller ZE, Yuan C** Atherosclerotic plaque imaging by carotid MRI. Curr Cardiol Rep. 2009;11(1):70-7.

24 **Saam T, Reiser MF, Nikolaou K** Imaging of the Carotid Atherosclerotic Plaque with 3T MRI Using dedicated 4-Channel Surface Coils. J Cardiovasc Magn Reson. 2009 Oct 27;11:41.

25 **Snitzer E** Cylindrical Dielectric Waveguide Modes. Journal of the Optical Society of America. 1961;51(5).

26 **Katscher U, Börnert P, Leussler C, van den Brink JS** Transmit SENSE. Magnetic Resonance in Medicine. Magn Reson Med. 2003 Jan;49(1):144-50.

Chapter 3

MRI of the carotid artery at 7 tesla
quantitative comparison with 3 tesla

W. Koning, A.A.J. de Rotte, J.J. Bluemink,
T.A. van der Velden, P.R. Luijten,
D.W.J. Klomp, J.J.M. Zwanenburg

(published in *Journal of Magnetic Resonance*, 2014, PMID: 24578311)

Abstract

Purpose

To evaluate the 7T MRI of the carotid arteries, as quantitatively compared with 3T.

Material and methods

7T MRI of the carotid arteries was performed in six healthy subjects and in two patients with carotid stenosis. The healthy group was scanned at 3T and at 7T, using current coil setups at both field strengths. T_1 and T_2 values of the normal carotid vessel wall were assessed at both field strengths. B_1^+ maps and SNR maps were obtained, as well as T_1 weighted images with a resolution as high as 0.4 x 0.4 x 1.5 mm^3.

Results

The T_1 of the normal carotid vessel wall was found to be 1227 $\pm$ 47ms at 3T and 1628 $\pm$ 130ms at 7T, while a T_2 of 55 $\pm$ 11ms at 3T and 46 $\pm$ 4ms at 7T was found. A two-fold average gain in SNR at the carotid arteries was found with 7T. T_1 weighted images showed an increased SNR at 7T for all subjects.

Conclusion

Evaluation between 3T and 7T carotid MRI with optimized setups at both field strengths showed improved SNR at 7T, an increase in vessel wall T_1 and a decrease in vessel wall T_2.

3.1 Introduction

Imaging the carotid vessel wall is important for risk assessment and intervention decisions (1, 2). In general, the resolution of current MRI is insufficient to reflect plaque detail (3 - 5). Current 1.5T and 3.0T MR scanners are operating at their limits in terms of maximizing image resolution for a given scan time. Increasing the field strength to 7T can increase the signal to noise ratio (SNR) (6), which can be utilized to increase resolution. Due to the field strength dependence of T_1 and T_2, image contrast may change at 7T. Hence, T_1 and T_2 measurements in the carotid vessel wall might need to be performed, and coils optimized. The goal of this study was two-fold. Firstly, to validate the receive and transmit performance of a current setup of 7T MRI, and secondly, to measure the change in T_1 and T_2 in the normal carotid vessel wall, relative to 3T MRI, as relaxation parameters depend on field strength.

3.2 Material and methods

The performance and potential of 7T carotid MRI was evaluated using a series of quantitative and qualitative experiments in six healthy subjects (two male, four female, age 27 $\pm$ 3) that were scanned at both 3T and 7T. Additionally, the feasibility of 7T MRI was demonstrated in two patients with carotid stenosis (both male, age 60 and 76). Institutional Review Board (IRB) approval was obtained for this study. All participants signed an informed consent according to the regulations of the IRB.

3.2.1 3T MRI

The 3T scans were performed on a whole body MRI scanner (Achieva 3.0T, Phillips Healthcare, Best, The Netherlands). The body coil was used for transmission, and an additional dedicated bilateral eight-channel phased array receive array (Shanghai Chenguang Medical Technologies Co., Shanghai, China) was used for reception. Outer dimensions of the receiver array were 12.8 x 10.3cm^2. The automatic power optimization provided by the MRI vendor was used for flip angle calibration.

3.2.2 7T MRI

The 7T scans were performed on a whole body MRI scanner (Achieva 7.0T, Philips Healthcare, Cleveland, USA). A two element leaky waveguide transmitter (7) was used in combination with a 30 element bilateral receiver array (15 elements per side) with total outer dimensions of 15 x 10 cm per side (MR coils BV, Drunen, the Netherlands). For all subjects, flip angle calibration was performed locally on the carotid arteries, as follows: transversal complex B_1^+ maps were acquired for each of the two transmit elements (Actual Flip angle Imaging (AFI) (8), $T_{R,1}/T_{R,2}$ = 25/125 ms, flip angle: 50º, gradient echo (GE), 220 x 220 x 55mm^3). To avoid slice profile effects, a 3D

acquisition was performed, acquiring 5 slices of which the middle slice was used. Since both elements contribute significantly to both regions of interest (left and right carotid arteries), in-house built software was used to perform B_1^+ shimming. Complex weighting factors were calculated iteratively, based on manually selected regions of interest (ROI's). Both left and right carotid arteries were selected as target ROI's for the shimming procedure. The calculated weighting factors were used for all the subsequent exams of the same subject. After shimming, a B_1^+ shimmed transversal B_1^+ map was acquired. The B0 field was shimmed for the neck using 3rd order image based shimming (9). A SAR model developed for this transmit array (7) was used to assure that all scans remained within the SAR guidelines (10).

3.2.3 SNR maps

SNR maps of a transverse slice of the neck were acquired at both field strengths. Identical protocols were designed to acquire a proton density weighted gradient echo image with minimal T_1 and T_2 weighting, with the following parameters: T_R/T_E = 200/2.1ms, flip angle = 6° (calibrated as described above), $BW_{readout}$ = 858Hz, FOV = 200 x 200mm^2, acquired voxel size = 1.0 x 1.0mm^2, slice thickness = 3mm. An additional noise image was acquired by repeating the scan with the same receive gain settings, phases and weightings in coil combination, but without the application of any RF or gradients. The standard deviation of the noise in the local ROI in the real-part image of the noise scan was taken as the noise metric to calculate the SNR of the corresponding image. SNR maps were corrected for differences caused by flip angle inhomogeneity. This was done using the measured actual flip angle from the B_1^+ shimmed B_1^+ map, according to Equation (1),

$$SNR_{corrected} = SNR_{measured} \cdot \frac{\sin(\alpha)}{\sin(c \cdot \alpha)} \quad (1)$$

where α is the nominal flip angle, and c is the ratio of the actual and the nominal flip angle, following directly from the B_1^+ map. From the corrected SNR maps of all subjects, profiles were measured from the edge of the neck inwards to evaluate SNR as a function of penetration depth. The mean and standard deviation (over the subjects) of the SNR was calculated at each depth.

3.2.4 T_1 and T_2 maps

T_1 and T_2 measurements in the vessel wall of the healthy subjects were acquired via T_1 and T_2 maps. T_1 was acquired by three subsequent high resolution inversion recovery turbo spin echo (IR-TSE) images with three different inversion times (50, 700 and 2000ms) and the following parameters: T_R = 8000ms, echo train length = 10 (including 2 startup echoes), refocusing angle = 80°, FOV 150 x 150mm^2 , slice thickness = 2mm, acquired voxel size = 0.5 x 0.5mm^2, SENSE acceleration factor = 3 (7T) and 2 (3T), total scan time = 6m48 (7T) and 9m36 (3T). T_2 relaxation time in the vessel wall was acquired using a high resolution multi echo spin echo sequence with the following parameters: 15 echos, echo spacing = 9ms, T_R = 1600ms, slice thickness = 2mm,

acquired voxel size = 0.5 x 0.5mm^2, FOV 150 x 150mm^2. No ECG gating was applied in either T_1 or T_2 measurements. Only even echo numbers were used for T2 determination. For both T_1 and T_2 maps, slices were positioned 2 cm below the bifurcation to facilitate a perpendicular planning of the slice through the vessel. Since the asymmetric transmit pattern of the 7T setup could not always guarantee sufficient B_1^+ on the left side of the neck at this low position for all volunteers, only the right side carotid arteries were taken into account for T_1 and T_2 analysis.

3.2.5 Anatomical scans

Multi-slice T_1 weighted turbo spin echo (TSE) sequences were acquired at both field strengths for each subject. Scan parameters: 15 slices, T_R = 1000ms, TSE factor 11 (including 3 startup echoes), reduced refocusing angles: min angle = 80^o, $T_{E,k=0}$ = 28ms, $T_{E,eq}$ = 18ms calculated for a given reference tissue with a T_1 and T_2 of 2000 and 50 ms, respectively ($T_{E,eq}$ is the equivalent echo time of a plain spin echo, yielding similar T_2 weighting (11)), acquired voxel size = 0.4 x 0.4mm^2, slice thickness = 1.5 mm, FOV = 180 x 180mm^2, SENSE acceleration factor = 2, acquisition time = 3m52s. In the two patients, an additional multi slice dual echo TSE scan was performed, providing proton density weighted (PDW) and T_2 weighted (T_2W) images. Scan parameters: 15 slices, T_R = 3000 ms, TSE factor 16, $T_{E,\,eq}$ = 27 and 70ms for first and second echo, respectively, acquired voxel size = 0.5 x 0.5mm^2, slice thickness = 2.0mm, FOV = 150 x 179mm^2, acquisition time = 4m36s.

3.2.6 Image analysis

T_2 maps were calculated by fitting the two parameter model shown in Equation 2 to the individual T_E images,

$$SI(T_E) = \alpha \cdot e^{-T_E / T_2} \tag{2}$$

where SI is the signal intensity and α is the amplitude of the curve. The mean and standard deviation T_2 over the vessel wall was calculated for each subject. The T_1 was calculated from three subsequently acquired images with different inversion times. In order to avoid errors from small deformation and displacement between the acquisitions, a circumferential center line was drawn in the vessel wall in each of the three IR images. Signal intensities were taken at this center line. The lengths of the three lines of the different acquisitions were normalized, and the data was interpolated to equal dimensions. A two parameter (amplitude and T_1) fit resulted in a circumferential T_1 line, of which the mean T_1 of each subject was taken for comparison between 3T and 7T. Equation 3 shows the two parameter inversion recovery model, where SI is the signal intensity as a function of inversion time TI, and α is the amplitude of the curve.

$$SI(t) = \alpha \cdot \left(1 - 2e^{-T_i / T_1}\right) \tag{3}$$

To evaluate the performance of 7T compared to 3T imaging, the combined effect of gain in SNR, and changed T_1 and T_2 relaxation time constants was computed for a plain spin echo sequence. This was done by combining the effects of SNR and the changes in T_1 and T_2 as described in Equation 4, derived from equations 2 and 3,

$$SNR_{act}(T_R, T_E) = SNR_{PD}(1 - e^{-T_R/T_1})e^{-T_E/T_2} \quad (4)$$

where SNR_{act} is the actual SNR for a given T_R and T_E and SNR_{PD} is the proton density weighted SNR corrected for B_1^+. A map with the actual ratio of 7T over 3T SNR_{act} as function of T_E and T_R was computed following Equation 4, accounting for the measured gain in SNR_{PD}, and the observed T_1 and T_2 values of the carotid vessel wall at both field strengths.

3.2.7 Coupling loss

An additional experiment was performed at 7T to quantify the potential loss of SNR due to coupling effects of the high density receiver array. Coupling effects were measured on a spherical phantom with a diameter of 12cm containing a solution of 120mg/ml $CuSO_4$ in water. Two images were acquired as follows: 1) "coupled": the image was acquired with all elements connected simultaneously and combined with sum of squares 2) "uncoupled": the image was acquired for each element separately, while detuning all other elements, and combining the separate element images with sum of squares, creating an ideally uncoupled and perfect noise decorrelated image. The ratio of the coupled image to the uncoupled image was calculated providing a spatial indication of losses due to combined coupling effects.

3.3 Results

Figure 3.1 shows a representative example of a coronal and transversal actual flip angle maps at 3T and 7T. The flip angle distribution at 7T was always much less homogeneous, reflecting an inhomogeneous B_1^+.

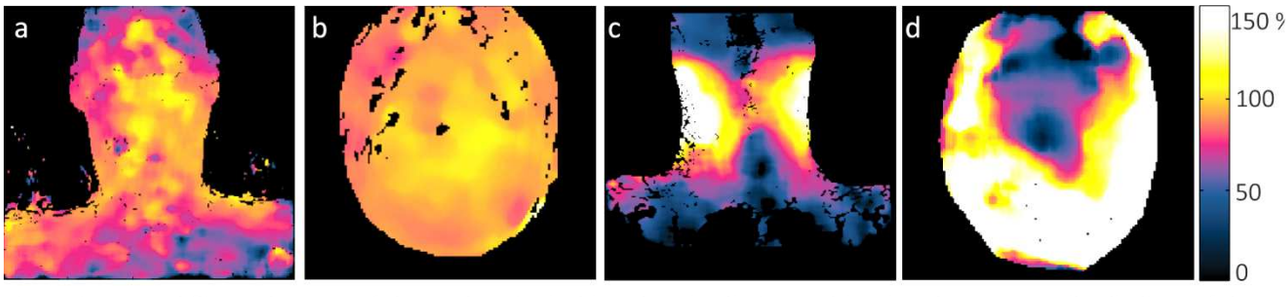

Figure 3.1 Actual flip angle maps of the neck at 3T (a, b) and 7T (c, d). Coronal (a, c) and transverse (b, d) slices of the neck. The actual flip angle map is shown as a percentage of the nominal flip angle.

Figure 3.2 shows examples of the bilateral B_1^+ shimming procedure for a 24 y.o. female and a 25 y.o. male. The measured actual flip angle in the ROI's after B_1^+ shimming, did not deviate more than 20% from 100% flip angle, in all subjects. The SNR maps that were corrected with the flip angle maps are shown in Figure 3.3, illustrating an improved SNR at 7T, particularly at the periphery.

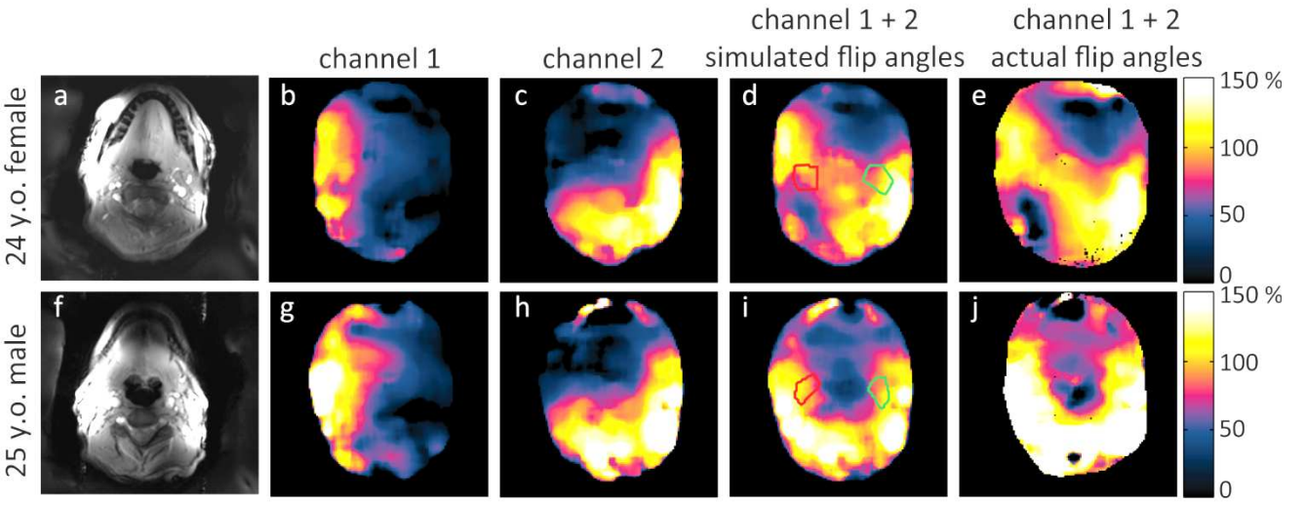

Figure 3.2 Examples of the bilateral B1+ shimming procedure in two volunteers (24 y.o. female and a 25 y.o. male). Actual flip angle maps are shown as a percentage of the nominal flip angle. In b, c, g and h, the actual flip angle maps of the single channels are shown. In d and i the simulated combined flip angle field after B1+ shimming is shown, with the red and green regions of interest indicating the locations for which the B1+ was optimized. In e and j the corresponding actually measured flip angle maps are shown.

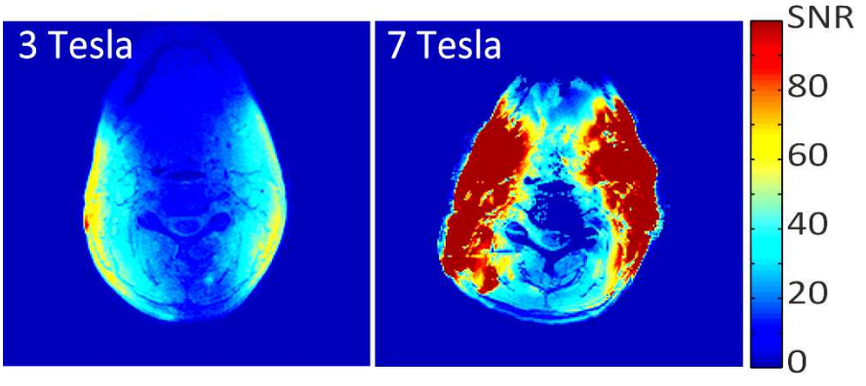

Figure 3.3 SNR maps in a transverse slice of the neck at 3T and 7T.

SNR profile lines averaged over subjects are shown in Figure 3.4a. As can be observed from the larger standard deviation, the SNR at 7T is more variable between subjects than at 3T, but remains stronger. Figure 3.4b shows the SNR ratio between 7T and 3T. Up to 2cm penetration depth there is a high average gain ($>$7/3) in SNR at the 7T setup. At a depth of 3cm, the average SNR gain was found to be a factor 2.0.

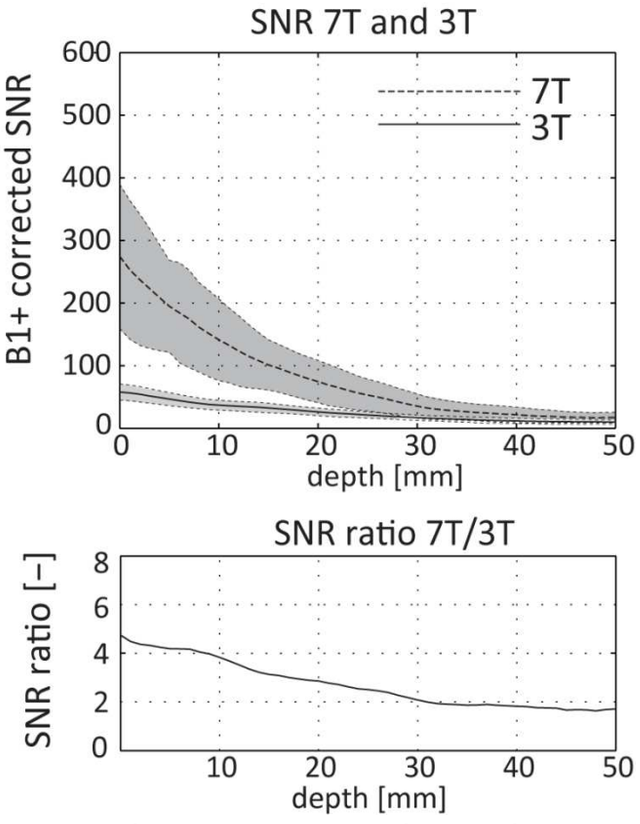

Figure 3.4 a) Mean SNR in the neck of all healthy subjects as a function of depth at 3T and 7T, and b) the ratio between these two curves. The centered lines show the inter subject average, and the filled area show the inter subject standard deviation.

T_1 weighted TSE scans for all subjects are shown in Figure 3.5. 7T subjective SNR was better than that of 3T in all cases.

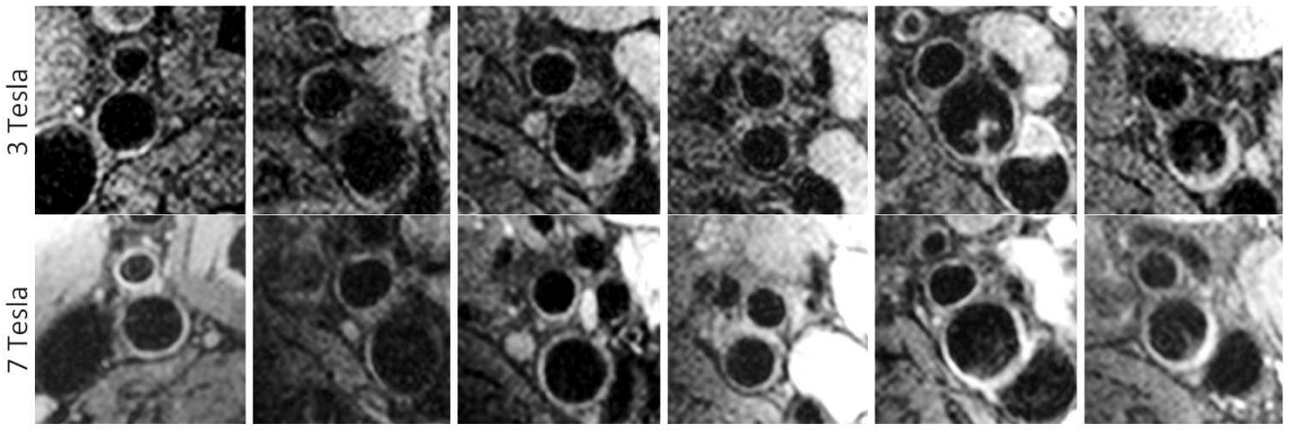

Figure 3.5 T1 weighted TSE images at 3T (upper row) and 7T (lower row) of all 6 healthy subjects.

Figure 3.6 shows T_1W, PDW and T_2W images, and B_1^+ maps after B_1^+ shimming, of two patient cases with carotid stenosis.

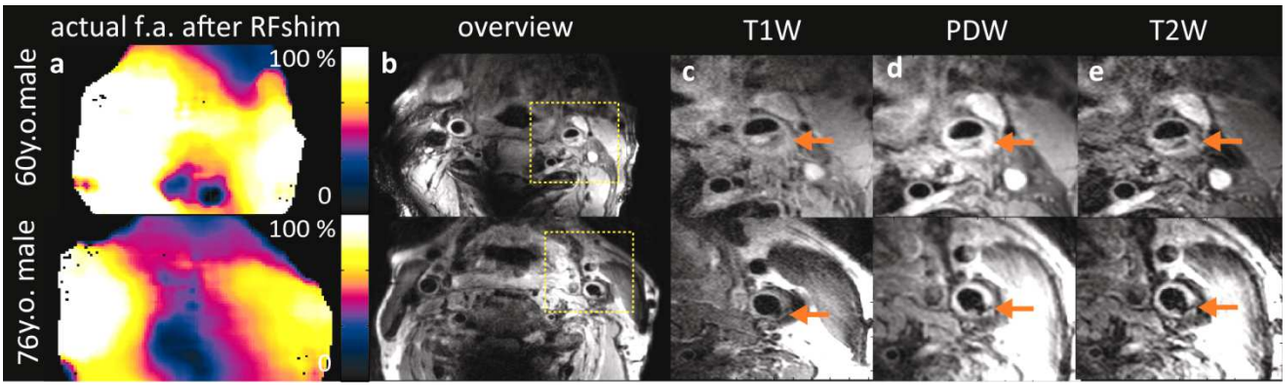

Figure 3.6 Two cases of patients (both male, age 60 and 76) with atherosclerotic plaques in the carotid artery. a) Actual flip angle maps after B1+ shimming, b) overview PDW image, and zoomed image showing c) T1W, d) PDW and e) T2W images

Figure 3.7 shows the T_1 and T_2 maps of the carotid artery of a 26 y.o. female, together with the T_1 and T_2 recovery curves and the individual Ti and T_E images of the same subject. The mean and standard deviation T_1 and T_2 over the vessel wall of each subject is given in Table 1, together with the mean and standard deviation T_1 and T_2 over all subjects.

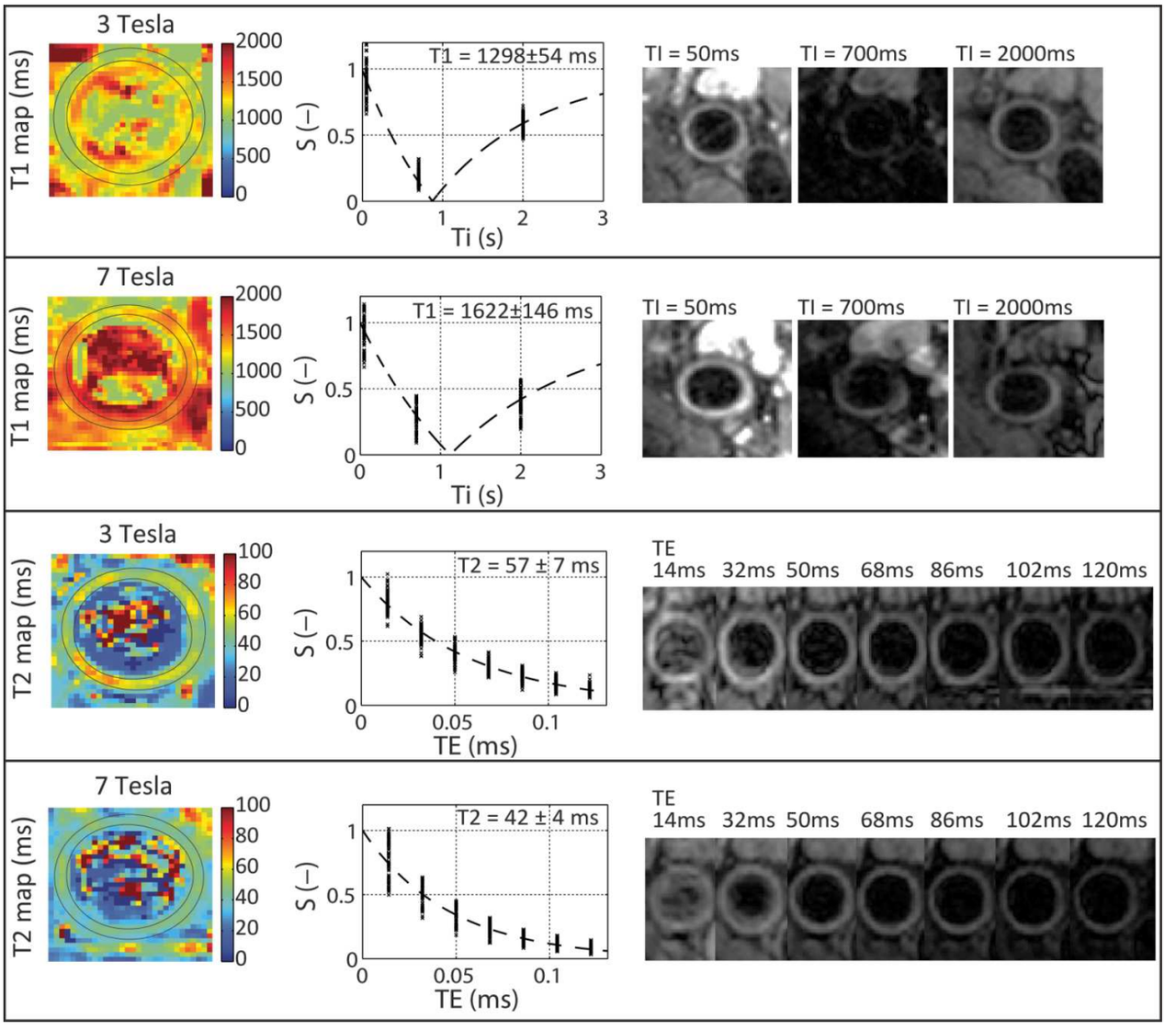

Figure 3.7 T_1 and T_2 relaxation time measurements in a normal carotid vessel wall at 3T and 7T. The left column shows the calculated T_1 and T_2 maps at both field strengths. Correspondingly, the middle column shows the relative intensities over the vessel wall, together with a fitted curve. The individual images for each inversion time (T_1 measurements) and echo time (T_2 measurements) are shown in the right column.

	T_1 3T	T_1 7T	T_2 3T	T_2 7T
Subject 1 (mean±SD of vessel wall)	1266 ± 91	1498 ± 149	77 ± 19	48 ± 6
Subject 2	1187 ± 100	1759 ± 332	47 ± 6	46 ± 7
Subject 3	1298 ± 54	1622 ± 146	56 ± 7	42 ± 4
Subject 4	1210 ± 120	1448 ± 152	46 ± 9	39 ± 8
Subject 5	1177 ± 69	1748 ± 250	53 ± 8	50 ± 7
Subject 6	1229 ± 80	1691 ± 226	50 ± 10	45 ± 7
all subjects (mean±SD of subjects)	**1227 ± 47**	**1628 ± 130**	**55 ± 11**	**46 ± 4**

Table 1: T_1 and T_2 relaxation times in the normal carotid vessel wall at 3T and 7T. Average and standard deviation over all subjects.

The combined effect on the SNR ratio 7T/3T of the changed T_1 and T_2 values, together with the gain in SNR, is shown in Figure 3.8. It shows that signal loss due to increased T_1 and reduced T_2, result in a reduction of SNR gain at 7T, depending on the chosen T_E and T_R.

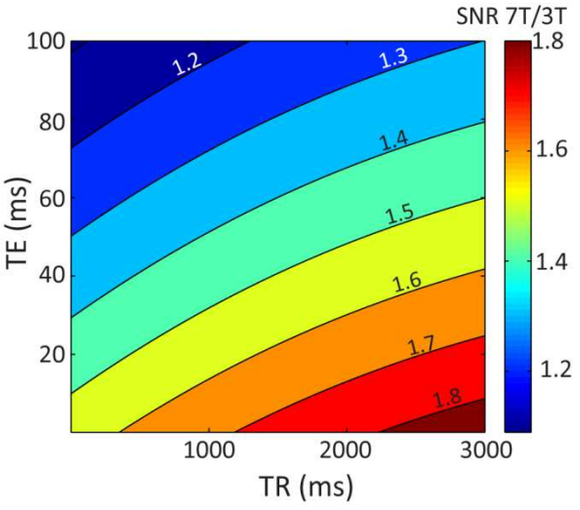

Figure 3.8 Theoretical signal gain 7T/3T for a spin echo sequence as a function of T_E and T_R (Equation 4) for the T_1 and T_2 values as given in table 1 calculated for an SNR gain of 2.0, following the SNR measurements. It shows the theoretical gain from 3T to 7T in SNR including the extra signal loss due to increased T_2 and decreased T_1. For T_R = 1000ms and T_E = 18ms, equivalent to the T_1 weighted sequence shown in Figure 3.5 and Figure 3.6, an SNR gain of 1.58 in the vessel wall is expected.

Additional signal loss due to coupling is shown in Figure 3.9. Figure 3.9a and b show the coupled

and the uncoupled image, respectively. The ratio of these is given in Figure 3.9c. In the center of the phantom an SNR ratio of 0.6 is measured, implying a SNR loss of 40% through noise coupling and noise correlation.

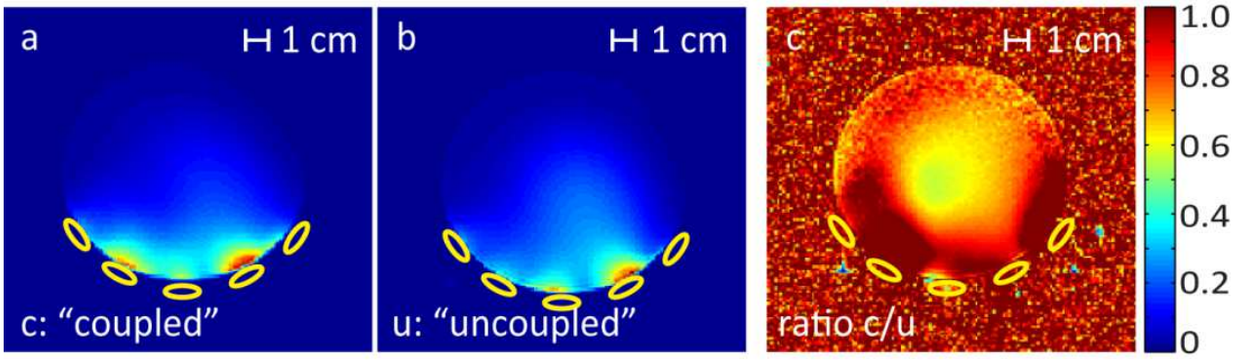

Figure 3.9 Phantom experiment giving a localized indication of the loss through coupling and noise correlation. The yellow circles indicate the high density receiver array at 7T. a) a "coupled" image (gradient echo), acquired with all elements simultaneously, b) an ideal "uncoupled" image and c) the ratio between the coupled and the uncoupled image. In the middle of the phantom up to 40 % loss is observed compared to the ideal perfectly uncoupled and noise decorrelated image.

3.4 Discussion

7T carotid MRI was evaluated by means of a quantitative comparison with 3T MRI. At both field strengths a current RF coil was used. An overall improved quality of 7T carotid MRI as compared to 3T was shown. The SNR improvement in the anatomical images was the result of different effects, such as contributions by increased sensitivity of the receive arrays, changed T_1 and T_2 relaxation parameters and increased B_1^+ field inhomogeneities. Even after B_1^+ shimming, there were still large differences in B_1^+ patterns between different subjects. This can be explained by the relatively small ROI's that were used for the B_1^+ shimming optimization. Targets in B_1^+ in the ROI's are met as far as possible with the available degrees of freedom of two transmit elements. Outside the ROI's, however, the B_1^+ is left unconstrained and can therefor show random patterns. The variability in B_1^+ patterns shows the capability of the multi transmit setup, to potentially optimize the B_1^+ for other locations such as the spine. The effect of the gradient in B_1^+ was not visible over a distance as small as the diameter of the carotid artery.

We report T_1 and T_2 relaxation times in the normal carotid vessel wall at 7T. The combination of in plane resolution of 0.5 x 0.5mm^2, and a suppressed blood signal was chosen to avoid partial voluming effects. Even a small volume of blood in a voxel containing vessel wall, can have a large effect on the quantified T_1 or T_2. This strong partial voluming effect is caused by the high signal of the freshly inflowed blood. This is why we chose a single slice TSE sequence, having inherent blood suppression, as a basis for both the T_1 and the T_2 measurement. T_2 values in the normal carotid vessel wall at 3T were in the expected range of previously published values (12 - 14). However, the

carotid vessel wall T_1 at 3T found in the current study (1227 $\pm$ 47ms) was considerable longer than the values found in earlier studies (685.9 $\pm$ 166ms (13), and 869 $\pm$ 224ms (15)) where faster methods were used to gain speed or cover a big volume. In the present study only one slice was acquired with a very long T_R of 8000ms to assure a straightforward T_1 assessment. Three inversion times resulted in a feasible scan time and a well determined fit using the two parameter model. It is a limitation of this study that only the relaxation parameters of the right carotid artery were acquired. The ROI's for the imaging and for the T_1 and T_2 measurements were too far apart to assure sufficient B_1^+ in both imaging ROI (above bifurcation) and the ROI of the T_1 and T_2 measurements (below the bifurcation).

Another possible limitation of this study is the fact that the receive arrays used at both field strengths were not the same. A greater number of smaller elements were used at 7T. However, the sizes of these elements were smaller than optimal for the depth of interest (16, 17). The ideal radius a of a loop coil for imaging an object at depth d is approximated by $a = d / \sqrt{5}$ (17). Therefore, it was assumed that the additional SNR benefit of the small element receive array at 7T was only present in the peripheral regions (at a depth of 2cm and less).At greater depths, however, the individual elements of the 3T setup were closer to optimal dimensions. From there, the parallel imaging reconstruction cancels out the bias of different individual element sizes (18), and SNR can be compared fairly. At the depths of the carotid artery, the only additional benefit of the density array at 7T compared to the 3T array, is not an increased SNR, but an increased acceleration possibility. In this research, this property was used for the time-costly T_1 maps, that were scanned with an acceleration factor of 2 at 3T, whereas at 7T an acceleration factor of 3 was applied. Overall, except for at the periphery ($<$3cm depth), the SNR gain 7T/3T was lower than the expected 7/3. The possible effect of T_1 and T_2 were already excluded by the proton density weighted SNR scan. We showed in the phantom experiment that the combined effect of noise coupling and noise correlation of the dense receiver contributed to 40% of the total noise at deeper tissues. Although the preamps are not mounted on the individual coil elements, the coupling numbers were reasonably low (7). Therefore it is expected that most of this noise contribution is caused by intrinsic similarities in field patterns of these coils, hence causing the noise correlations.

A higher variance in SNR was observed at 7T. A possible explanation could be that the small elements at 7T are more sensitive to tissue loading. Therefore, less tight positioning onto the neck could have a greater effect on 7T than it has on 3T where the individual elements were bigger. Further, the signal decreases faster with distance from the surface than for a receive array with larger elements. Hence, variation in depth of the carotid artery resulted in a larger variation in the respective SNR at 7T than it is the case at 3T. An earlier study compared carotid MRI at 7T and 3T qualitatively (19) and showed good lumen area and vessel wall area reproducibility at both fields. However, these experiments were performed with one large single loop coil per side for reception at both field strengths, while other studies apply more dedicated receiver arrays with eight (20) or

sixteen (21) elements. Another study focusing on a comparison of 3T and 7T intracranial angiography, reports an increase of CNR between lumen and surrounding of the carotid arteries of 30-40% (22). In that study, no tissue properties of the vessel wall itself were assessed, and the used head coil prohibited imaging the carotid arteries at a level as low as the bifurcation. Even when a dedicated neck coil is used, the transmit field is localized to the neck. Due to the absence of a body coil (23), conventional blood suppression strategies (Double inversion recovery (DIR) (24) and quadruple inversion recovery (QIR) (25)) could not be applied with this limited transmit field at 7T. Instead, a turbo spin echo (TSE), which has inherent black blood contrast, was used as an alternative. At 7T there is an increased specific absorption rate (SAR), which can reduce the efficiency of the SAR demanding sequences like TSE, by requiring increased TR. Alternatively, depending on the tissue T_1 and T_2 relaxation times, reducing the refocusing angles of an echo train in a TSE, can also effectively reduce SAR while controlling contrast and SNR (26). Moreover, as T_1 and T_2 relaxation times will be different between the field strengths, sequences have to be optimized specifically for 7T for optimal CNR and SNR. While the observed SNR at 7T increased with a factor of 2.0 as compared to 3T, the altered relaxation times also contributed to changes in SNR and tissue contrast.

In conclusion, an evaluation between 3T and 7T carotid MRI with optimized setups at both field strengths was performed. An increase in SNR of even greater than 7/3 was observed at the periphery of the neck. At an average depth of the carotids, still a considerable gain in SNR of a factor 2.0 was measured in a series of healthy subjects, though somewhat less than the theoretical factor of 2.33. Phantom experiments indicate that the high density receive array used at 7T suffers some loss in SNR due to coupling, but at the same time benefits from higher acceleration factors using parallel imaging techniques. In all subjects, the 7T subjective SNR was better than the 3T SNR. For the first time, T_1 and T_2 in the healthy carotid vessel wall was documented for both 3T and 7T, which are needed to perform tailored sequence optimization in the future.

References

1 **Leiner T, Gerretsen S, Botnar R, Lutgens E, Cappendijk V, Kooi E, van Engelshoven J** Magnetic resonance imaging of atherosclerosis. European Radiology. 2005; 15: 1087–99.

2 **Rothwell P, Gibson R, Warlow C** Interrelation Between Plaque Surface Morphology and Degree of Stenosis on Carotid Angiograms and the Risk of Ischemic Stroke in Patients With Symptomatic Carotid Stenosis. Stroke 2000; 31: 615–621.

3 **Saam T, Ferguson M, Yarnykh V, Takaya N, Xu D, Polissar N, Hatsukami T, Yuan C** Quantitative evaluation of carotid plaque composition by in vivo MRI. Arterioscler Thromb Vasc Biol 2005; 25: 234–9.

4 **J.M. Cai, T.S. Hatsukami, M.S. Ferfuson, R. Small, N.L. Polissar CY** Classification of Human Carotid Atherosclerotic Lesions With In Vivo Multicontrast Magnetic Resonance Imaging. Circulation. 2002; 106 (11): 1368–1373.

5 **Shinnar M, Fallon JT, Wehrli S, Levin M, Dalmacy D, Fayad Z a, Badimon JJ, Harrington M, Harrington E, Fuster V** The diagnostic accuracy of ex vivo MRI for human atherosclerotic plaque characterization. Arteriosclerosis, thrombosis, and vascular biology. 1999; 19 (11): 2756–61.

6 **Edelstein WA, Glover GH, Hardy CJ, Redington RW** The intrinsic signal-to-noise ratio in NMR imaging. Magn Reson Med. 1986; 3: 604–18.

7 **Koning W, Bluemink JJ, Langenhuizen EAJ, Raaijmakers AJ, Andreychenko A, van den Berg CAT, Luijten PR, Zwanenburg JJM, Klomp DWJ** High-resolution MRI of the carotid arteries using a leaky waveguide transmitter and a high-density receive array at 7 T. Magn Reson Med 2013; 69: 1186–93.

8 **Yarnykh VL** Actual flip-angle imaging in the pulsed steady state: a method for rapid three-dimensional mapping of the transmitted radiofrequency field. Magn Reson Med 2007; 57: 192–200.

9 **Schär M, Kozerke S, Fischer SE, Boesiger P** Cardiac SSFP imaging at 3 Tesla. Magn Reson Med 2004; 51: 799–806.

10 The internaltional Commission on Non-Ionizing Radiation Protection, Medical Magnetic Resonance (MR) procedures: protection of patients. Health Phys 2004; 87: 197-216

11 **Busse RF, Hariharan H, Vu A, Brittain JH** Fast spin echo sequences with very long echo trains: design of variable refocusing flip angle schedules and generation of clinical T2 contrast. Magn Reson Med 2006; 55: 1030–1037.

12 **Sun B, Giddens DP, Long R, Taylor WR, Weiss D, Joseph G, Vega D, Oshinski JN** Automatic plaque characterization employing quantitative and multicontrast MRI. Magn Reson Med 2008; 59(1): 174–80.

13 **Mihai G, Giri S, Sharkey-Toppen TP, Raman SV, Rajagopalan S, Simonetti OP** Quantitative T1 , T2 and T2 * Mapping of Carotid Artery Normal Wall and Atherosclerotic Plaque. Proceedings of the 19th Annual Meeting of ISMRM, 2011, Montreal, Canada.

14 **Biasiolli L, Lindsay AC, Chai JT, Choudhury RP, Robson MD** In-vivo quantitative T2 mapping of carotid arteries in atherosclerotic patients: segmentation and T2 measurement of plaque components. Journal of Cardiovascular Magn Reson, 201; 15: 69.

15 **Coolen BF, Heijtel DF, Potters WV, Nederveen AJ** 3D carotid wall T1 quantification using variable flip angle 3D Merge with steady-state recovery. Proceedings of the 21st Annual Meeting of ISMRM, 2013, Salt Lake City, USA.

16 **Hoult DI, Phil D** Sensitivity and power desposition in a high-field imaging experiment. J Magn Reson Imaging. 2000;12(1): 46-67

17 **Bottomley PA, Lugo Olivieri CH, Giaquinto R** What is the optimum phased array coil design for cardiac and torso magnetic resonance? Magn Reson Med. 1997; 37: 591–599.

18 **Roemer PB, Edelstein WA, Hayes CE, Souza SP, Mueller OM** The NMR phased array. Magn Reson Med. 1990; 16: 192–225.

19 **Kröner ES, van Schinkel LD, Versluis MJ, Brouwer NJ, van den Boogaard PJ, van der Wall EE, de Roos A, Webb AG, Siebelink H-MJ, Lamb HJ** Ultrahigh-field 7-T magnetic resonance carotid vessel wall imaging: initial experience in comparison with 3-T field strength. Investigative radiology 2012; 47: 697–704.

20 **Balu N, Yarnykh VL, Scholnick J, Chu B, Yuan C, Hayes C** Improvements in carotid plaque imaging using a new eight-element phased array coil at 3T. J Magn Reson Imaging 2009; 30: 1209–1214.

21 **Tate Q, Kim S-E, Treiman G, Parker DL, Hadley JR** Increased vessel depiction of the carotid bifurcation with a specialized 16-channel phased array coil at 3T. Magn Reson Med 2012; 69: 1486–1493.

22 **von Morze C, Xu D, Purcell DD, Hess CP, Mukherjee P, Saloner D, Kelley D a C, Vigneron DB** Intracranial time-of-flight MR angiography at 7T with comparison to 3T. J Magn Reson Imaging. 2007; 26(4):900–4.

23 **Schick F** Whole-body MRI at high field: technical limits and clinical potential. European Radiology 2005; 15: 946–59.

24 **Edelman R, Chien D, Kim D** Fast Selective Black Blood MR Imaging. Radiology. 1991; 655–660.

25 **Yarnykh VL, Yuan C** T1-insensitive flow suppression using quadruple inversion-recovery. Magn Reson Med 2002; 48: 899–905.

26 **Hennig J, Weigel M, Scheffler K** Calculation of flip angles for echo trains with predefined amplitudes with the extended phase graph (EPG)-algorithm: principles and applications to hyperecho and TRAPS sequences. Magn Reson Med 2004; 51: 68–80.

Chapter 4

Whole brain B_1^+ shimmed arterial spin labeling at 7 tesla using a multi transmit head and neck coil

W. Koning, E.T. Petersen, J.J. Bluemink, J.Hendrikse,
P.R. Luijten, J.J.M. Zwanenburg, D.W.J. Klomp

(in peer-review process)

Abstract

Purpose

Arterial spin labeling (ASL) at ultra-high field can offer an increased signal to noise ratio (SNR), due to increase of intrinsic SNR and blood T1. However, using a standard head transmission coil, RF power deposition can jeopardize feasibility of whole brain 7T ASL. The purpose of this study was to demonstrate that extension of the head coil makes 7T ASL feasible for the whole brain.

Material and methods

A 7T standard head coil was used in combination with a with a leaky waveguide transmitter around the neck, and used for pulsed labeling. In total eight subjects were scanned. Dynamic B_1^+ shimming was utilized to control B_1^+. The effect of respiration on the stability of the perfusion maps was evaluated.

Results

Whole brain ASL was acquired in all subjects. B_1^+ in the left and right carotid and vertebral arteries was 11.0±3.3, 11.9±3.9, 9.5±3.6 and 9.0±2.4μT, respectively. Perfusion maps were acquired with label delays up to 4000ms. Variability between individual label-control subtraction pairs could not be related to respiration-induced B_0 fluctuations.

Conclusion

It was shown that whole brain ASL at 7T is feasible, when extending the standard head coil with additional coils towards the neck.

4.1 Introduction

The concept of arterial spin labeling (ASL) MRI was first introduced in 1992 by Detre et al (1, 2). Since then, this concept became an important, and the only truly non-invasive, tool for measuring cerebral perfusion, often referred to as cerebral blood flow (CBF). Imaging of cerebral perfusion can be used as an early marker for cerebrovascular pathologies and as a quantitative way to monitor hemodynamic changes (3, 4) or the effect of an occlusion in the brain feeding arteries such as the carotid arteries (5). However, there are limitations. Firstly, the perfusion maps that are examined during ASL experiments are of very low signal to noise ratio (SNR). Therefore, averaging over multiple acquisitions is required to yield enough SNR. This is constraining the resolution of the perfusion weighted image that can be achieved during acceptable scan times. In addition, the ASL contrast is imposed with physiologic noise that can be caused by field fluctuations originating from breathing (6). Secondly, the tracer used in ASL is magnetically inverted blood which is decaying by T_1 relaxation. As a result, the perfusion signal in tissues with longer blood transit times will have lower SNR. This complicates perfusion measurements in for example white matter (WM), which has lower perfusion and longer blood transit times than grey matter (GM). The ability of ASL to detect WM perfusion at 3 Tesla has been debated. While identification of WM regions with altered hemodynamics is feasible (7), the quantification of this ASL signal into CBF values in WM is challenging, if possible at all at 3 Tesla (8). Thus, despite the great advances in ASL, there are still limitations and potentials for improvement.

4.1.1 Why ASL at 7T?

The current limitations of ASL (low SNR and decaying perfusion label) are mitigated by going to higher field strength. The expected benefit of a higher field strength comes from the increased intrinsic SNR as well as the increased T_1 of arterial blood, yet the effects of field fluctuations may increase. The gain in SNR of ASL at 4T compared to 1.5T was already shown by Wang et al (9). Going from 3T to 7T, there is an overall gain in SNR of the perfusion signal that was estimated to be of a factor of 2.0 – 2.5 (10), despite the shorter $T_2(*)$ relaxation times at high field (11). In addition, the increase of the blood T_1 ($T_1 \sim \omega^{0.3}$ (12)) increases the lifetime of the tagged blood signal, which allow for a longer post labeling delay (PLD). A longer PLD enables measuring perfusion signal in areas with longer blood transit times and may facilitate for example the CBF measurement in the WM parts of the brain (8).

4.1.2 The necessity of an additional labeling coil at 7T

The feasibility of 7T ASL has already been shown for both pulsed ASL (PASL) (13) as well as for pseudo continuous ASL (pCASL) (14 - 16). However, all these studies report the challenge to perform whole brain ASL at 7T. This challenge is related to reduced electromagnetic wavelength, because of which a body transmit coil (standard at 3T) is not available at 7T. Instead, a smaller

local head coil is commonly used for transmission in the head. The B_1^+ efficiency of such a head coil is significantly lower in the brain-feeding arteries towards the neck, than it is in the center of the brain (13 - 15). This will jeopardize the application of both PASL and (p)CASL in ways described next. One of the main determinants of a successful ASL experiment is a sufficiently large tagged blood volume, which is limited in a different way for PASL and (p)CASL:

Concerning PASL: the label slab will be truncated on the proximal side due to the reduced B_1^+ efficiency. As a result, the effective label thickness will be limited, resulting in a small tagged blood volume and thereby short bolus duration, insufficient to harvest the gains of the higher field strength. On top of that, the poorly defined label slab will cause errors in quantification (17). In the standard setup, the label slab (or the "reach" of the head coil) can be increased in two ways: 1) by increasing the power during labeling. However, the low efficiency can result in a power demand higher than the amplifiers can deliver. Alternatively 2), the slab can be placed further inside the coil by placing the slab higher in the brain, which compromises whole brain ASL, and restricts perfusion maps to the higher slices in the brain (13, 14). A better solution would be to extend the effective B_1^+ area in the neck region, either by adding an additional coil for labeling in the neck or, preferably, by designing a transmit coil with a larger coverage in the neck region. This in turn will enable larger label slabs with a lower specific absorption rate (SAR), as the B_1^+ field will be extended and the RF power can be distributed more efficiently.

Concerning (p)CASL: continuous arterial spin labeling CASL (18) has an advantage of a well defined and typically significantly longer bolus duration which makes quantification robust, but with the penalty that it is very SAR intensive, even at 3T. Pseudo continuous ASL, pCASL (19, 20), was introduced as an adaptation of CASL with increased efficiency (21). For pCASL to acquire whole brain perfusion maps, the label slice should be below the circle of Willis to avoid interference of the label slice with the imaging slices. Using a volume transmit coil at 7T, it has been shown that the B_1^+ efficiency at this location is severely compromised. Therefore, a relative high peak power is required to meet the B_1^+ criterea for the inversion. The resulting SAR constraints allow only very short labeling times (<500ms) (14, 15), or require a very long T_R. Therefore, the optimal parameters for maximal perfusion SNR following from the General Kinetic Model (22), cannot be met. Choosing a higher location for the label slice will increase the B_1^+ efficiency, which will allow for longer labeling times, but it will also sacrifice the lower brain slices. Similar to PASL, a better solution would be to extend the transmit coil or to add an additional coil for labeling in the neck region, which would increase the B_1^+ efficiency significantly and thereby enable longer label durations due to the significantly reduced SAR.

In summary, all previous 7T ASL studies show the challenges of performing ASL at 7T with only a head coil, and all studies mention the expected benefit of an additional neck coil. At 3T the benefit of an additional label coil (23) has been addressed as twofold: beneficial for SAR, and reduction of Magnetization Transfer (MT) effects due to off-resonance excitation in the brain. The goal of this

research was primary to prove the feasibility of whole brain ASL at 7T with an additional labeling coil. In this paper, we propose to extend the standard 7T head coil setup with a so-called leaky waveguide transmitter (24). This new type of transmit array consists of a neck pillow filled with deuterium oxide (see Figure 4.1). Traditional surface coils only distribute B_1^+ locally. The waveguide transmitter, however, utilizes the shortened wavelength at 7T and facilitates the distribution of B_1^+ around the neck, driven by dipole antennas. The dipole antennas can be mounted on the pillow on arbitrary positions, and their cumulative B_1^+ field can be controlled using B_1^+ shimming. With this setup we demonstrate the feasibility of whole brain ASL with extended labeling at 7T and we evaluate the stability of the individual perfusion maps related to respiration.

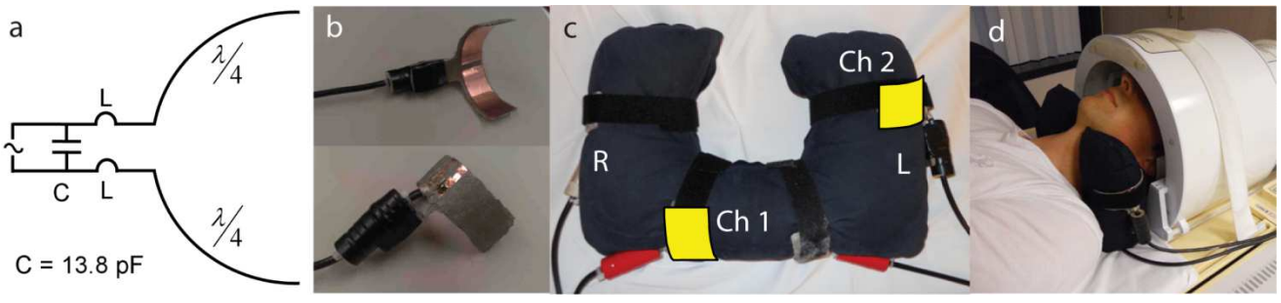

Figure 4.1 The 7T RF setup, a) schematic of the individual transmit elements (inductance L = 2cm leads), and b) a picture of the same elements showing a cable trap around the cable (in black tape).c) Antenna's on the waveguide transmitter can be placed in a flexible amount and on a flexible location. The positions of the elements as used in the experiments are annotated in yellow on the picture, based on (24). d) U-shaped leaky waveguide transmitter used in addition to standard 7T head imaging setup.

4.2 Methods

All experiments were performed on a whole-body 7T MRI scanner (Achieva 7.0T, Philips Healthcare, Cleveland, USA). In-vivo scans were performed on in total eight healthy subjects (5 male, 3 female, age 31 ± 5 year, referred to as subject #1-8) with approval of the ethics committee of the institute and in accordance with their regulations. A series of whole brain ASL experiments was performed in subject #1-6, B_1^+ shimmed territorial was demonstrated in subject #7 and B_1^+ efficiency measurements were performed in subject #8. All subjects gave written informed consent prior to the study.

4.2.1 Hardware

A birdcage transmit/receive head coil was used in combination with a 32 channel receive head coil (Nova Medical, Wilmington, MA, USA). The transmit part was combined with a 2 channel U-shaped leaky waveguide neck transmitter (MR coils BV, Drunen, The Netherlands) (24) as is shown in Figure 4.1c. The volume head coil was driven by 4 kW peak power, whereas each channel of the waveguide transmitter was also driven by 4 kW peak power. The transmit elements were directly

connected to the output of the amplifiers and could therefore not be used to receive the MR signals. RF power coupling between the head coil and the waveguide transmitter were measured as S12. Figure 4.1b shows how both antennas were positioned on the waveguide transmitter. The asymmetric position of the two elements on the U-shaped tube is the result of maximizing the asymmetric B_1^+ field in the carotid arteries (24). A respiration pressure unit (RPU) was positioned on the chest of the subjects to record the respiration phase during the experiments.

4.2.2 SAR

A simulation model of the neck coil (24) was used to keep the tissue heating for all applied sequences in accordance with the SAR regulations. SAR values were computed for using the head coil exclusively and for using the head coil combined with the waveguide neck transmitter. For these calculations the B_1^+ efficiency was needed, which was determined by measurements in a single subject (#8) as follows: for both the standard head coil setup as well as the setup combined with the waveguide neck transmitter, the B_1^+ power efficiencies ($B_1^+/\sqrt{power}$) at the label plane was measured from B_1^+ maps (AFI (25), nominal flip angle = 50º, $T_{R,1}$/ $T_{R,2}$ = 50/250ms). A measured loss of 50% through cabling and connectors was taken into account. For the head coil only setup, the B_1^+ efficiency was evaluated at the height of vertebrae C2, taken as the highest label location without affecting the lower brain regions. For the setup with the neck coil, the B_1^+ efficiency was measured in the middle of the neck coil, slightly below the jaws. SAR values were calculated for (the SAR intensive) pseudo continuous labeling. The resulting maximal label duration was calculated based on a maximum allowed SAR_{10g} of 10 $W \cdot kg^{-1}$, a B_1^+ amplitude for the label pulse of 1.7 µT (20), and a T_R of 6000ms.

4.2.3 B_1^+- and B_0 shimming

Every ASL sequence was performed in combination with a trigger to an external device, that was used to dynamically control the phase and amplitude of each individual transmit element during the scanning, also known as dynamic B_1^+ shimming (26). This enabled the application of different B_1^+ fields for control and label experiment as well as for different territorial selections. The B_1^+ shimming procedure went as follows: in order to calculate the appropriate B_1^+ phases and amplitudes, complex B_1^+ maps where acquired for both transmit elements of the waveguide transmitter, using a double T_R approach (AFI (25), nominal flip angle = 50º, $T_{R,1}$/ $T_{R,2}$ = 50 / 200ms, total scan duration 1m12s). Regions of interest (ROI's) were drawn in a shim tool written in Matlab ® and available on the scanner console. In this tool the optimal complex weighting factors for each transmit element were calculated by an iterative minimization routine. The B_1^+ target in the selected ROI's was set to 12µT. This B_1^+ shim procedure was done for each subject specifically and took approximately 3 minutes in total. The resulting single slice B_1^+ maps for the neck shim, applied during labeling, were acquired in each subject. During this B_1^+ map acquisition the head coil was transmitting as well, in order to give a combined overview of the B_1^+ fields of the head coil and the waveguide neck transmitter, as used dynamically during the ASL experiments. B_1^+

variation in the four main feeding arteries (left and right carotid and vertebral arteries) was measured as well as a 10 cm through plane B_1^+ profile, close to the feeding arteries at both left and right side. During labeling, the head coil was always assured to be switched off, by putting the corresponding B_1^+ shim amplitudes to zero. During readout, the waveguide neck transmitter was switched off in a similar manner.

A 3rd order B_0 shim was applied, optimized for the entire brain region, using image based shimming (27). For each ASL scan, an additional F_0 was determined at the location of the labeling, to compensate for frequency offsets induced by the higher order B_0 shim fields. B_0 maps were acquired after B_0 shimming using a double T_E field map with $T_R/T_{E,1}/T_{E,2}$ = 5.3/2.5/3.5 ms, and a scan duration of 18s. During the acquisition of both B_0 and B_1^+ maps, the 32 channel head receive array was used for reception in the whole field of view.

4.2.4 In-vivo ASL experiments

All ASL experiments were performed using a multi slice single shot EPI readout, SENSE acceleration factor 2, field of view (FOV) 240 * 240 mm^2 , matrix 64 * 64, 15 slices with thickness 5 mm, inter slice gap 2mm and applying SPIR fat suppression. Transversal and coronal B_1^+ maps were acquired and M_0 maps (T_R = 10s, 4 signal averages) with identical readout as the ASL experiments were acquired in every volunteer for CBF quantification. The following experiments were performed:

1) Whole brain pulsed ASL was performed on subject #1-6 using the PULSAR ASL sequence (28) with a PLD of 2000ms, T_R = 6000ms and a label slab thickness of 100mm. To minimize artifacts, T_1- and B_1 insensitive in-plane pre-saturation WET (28, 29) was applied right before the label pulse, and a 90 degree post saturation pulse was applied right after the label pulse. While the original PULSAR sequence uses an EPISTAR (30) based label scheme for MT compensation, a PICORE scheme (31) was used in this work, applying the control pulse with the same resonance offset as the label pulse, but without a slice selection gradient. A broadband FOCI pulse (32) was applied for inverting the arterial blood in a 100mm label slab. To exclude potential instability in the ASL signal due to respiration (6, 33), “Respiratory pacing” was applied: the volunteer was instructed to inhale right after hearing the readout train, assuring that the readout train was always applied in an exhaled state. The T_R of 6000 ms enabled a normal respiration frequency. A total of 30 subtraction pairs were acquired and averaged, resulting in a total scan time of 6 minutes and 6 seconds.

2) Paced versus free respiration. To determine the influence of respiration on possible instability between the different repetitions, the PASL protocols of 1) were repeated in subject #1-6 with free instead of paced respiration. This allowed the T_R to be decreased to 3200ms. The number of acquired subtraction pairs was increased to 56 to keep the total scan time equal to the other protocols. The respiration phase during the experiments was recorded in every experiment. For every subtraction pair the respiration phase difference $\Delta\phi_R$ was calculated by scaling the

respiration cycle between 0 and 1 and taking the absolute difference $\Delta\phi_R = |\phi_{R,control} - \phi_{R,label}|$. The free respiration PASL was reconstructed per voxel in three different ways:

1. by averaging over all 56 repetitions,
2. by averaging over the 28 repetitions corresponding to the lowest $\Delta\phi_R$ between control and label,
3. by averaging over the remaining 28 repetitions corresponding to the highest $\Delta\phi_R$ between control and label.

For all these three reconstructions of the free breathing PASL, as well as for the paced respiration PASL, the mean perfusion and the mean variance of the segmented grey matter pixels were calculated over the middle slice. The mean variance was used as a metric for instability.

3) Additional explorations for 7T ASL applications. As a demonstration of potential applications two additional experiments were performed on single subjects. *First*, in subject #4 the PLD was increased to 3000 and 4000ms, respectively. *Second*, B_1^+ shimming was utilized to perform territorial ASL on subject #7. Two different shim modes were applied for left and right labeling, respectively, by focusing the B_1^+ on the arteries at one side, while cancelling it on the other side. The same PASL protocol as described in the previous points was applied to acquire the territorial ASL maps.

Cerebral blood flow (CBF) was quantified for all pulsed ASL experiments by using the following model (34):

$$CBF = \frac{\Delta S \cdot \lambda}{2\alpha \cdot M_0 \cdot \tau} e^{\frac{PLD}{T_{1,blood}}} \quad (1)$$

where ΔS is the signal difference between label and control, λ is the local water partition coefficient, α is the inversion efficiency, τ the bolus length assuming a perfect squared bolus. The following constants were used for the quantification: λ = 0.98, α = 0.95, τ = 0.5 s, $T_{1,blood}$ = 2100 ms (10). The CBF maps of the individual subtraction pairs were averaged to yield the eventual CBF map.

4.3 Results

Figure 4.2 shows the B_1^+ maps in different orientations for the head coil only (Figure 4.2a) and for the head coil combined with the waveguide neck transmitter (Figure 4.2b), together with the B_0 maps (Figure 4.2c). The B_1^+ efficiency of the waveguide neck transmitter, normalized to 1 W deployed power, in the carotids at the height of the jaws was found to be approximately 0.40 µT / √W. For the head coil only, the efficiency at the height of the C2 vertebrae was estimated at 0.12 µT / √W. With the given SAR model (24), and a fixed T_R of 6000ms, this results in a maximal allowed label duration of 561ms for the head coil. With the added waveguide neck transmitter the

maximal allowed label duration will increase to 1725ms (Table 2), or 3450ms in case no RF is deployed during control. The RF power coupling (S_{12}) between head coil and the waveguide neck transmitter was measured to be less than -12 dB.

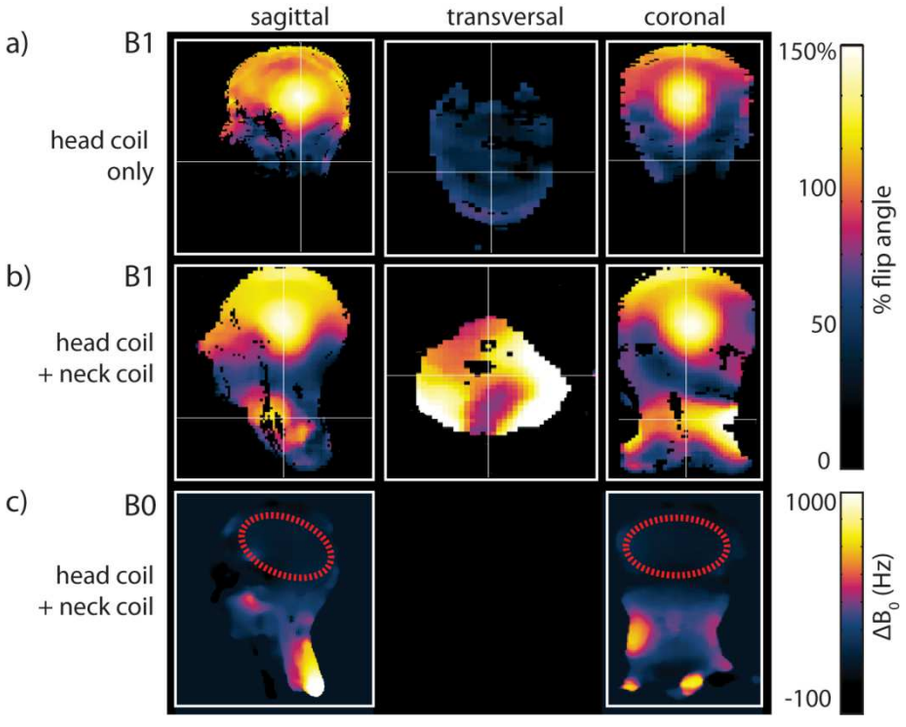

Figure 4.2 Demonstration of the necessity of an external labeling coil for full brain ASL at 7T, B1+ maps without (a) and in combination with (b) the use of an external labeling coil. a) The transversal AFI map with head coil is shown at the height of vertebrae C2 which is taken as the highest possible label location without affecting the lower brain regions. b) The transversal AFI map with both head and neck coil is shown at the label height when using an external labeling coil. c) Sagittal and coronal B0 maps: the red circle indicates the region for which the B0 was optimized by the third order B0 shimming procedure.

	Neck Array	Head coil
B_1^+/power (µT/√W)	0.40*	0.12**
max local SAR_{10g} ($W \cdot kg^{-1} \cdot W^{-1}$)	1.95	0.56
max local SAR_{10g} – 1.7 µT continuous ($W \cdot kg^{-1}$)	35	107
max duty cycle within SAR limit	29 %	9 %
max allowed label duration (for T_R = 6 sec)	**1725 ms**	**561 ms**
if no RF during control	**3450 ms**	

** B_1^+ efficiency at the height of the neck coil*

*** B_1^+ efficiency at the height of vertebrae C2*

Table 2 Maximal allowed label duration for pseudo continuous labeling with 1.7 µT amplitude.

Figure 4.3 gives an overview of the full brain pulsed ASL results in all subjects, together with the corresponding transversal B_1^+ maps at the label slab position. The average and standard deviation over the six subjects of the B_1^+ in the left and right carotid and vertebral arteries was found to be 11.0 ± 3.3, 11.9 ± 3.9, 9.5 ± 3.6 and 9.0 ± 2.4μT, respectively. The average B_1^+ in a 10 cm through plane line was 10.3 ± 3.0 and 13.4 ± 3.3μT (left and right), with an average minimum of 5.5 and 2.9μT (left and right) and an average maximum of 13.9 and 17μT (left and right). An outlier was subject #5, which showed relative poor CBF maps, which is likely to be the consequence of a poorly shimmed B_1^+ field, which is shown in the bottom row of Figure 4.3.

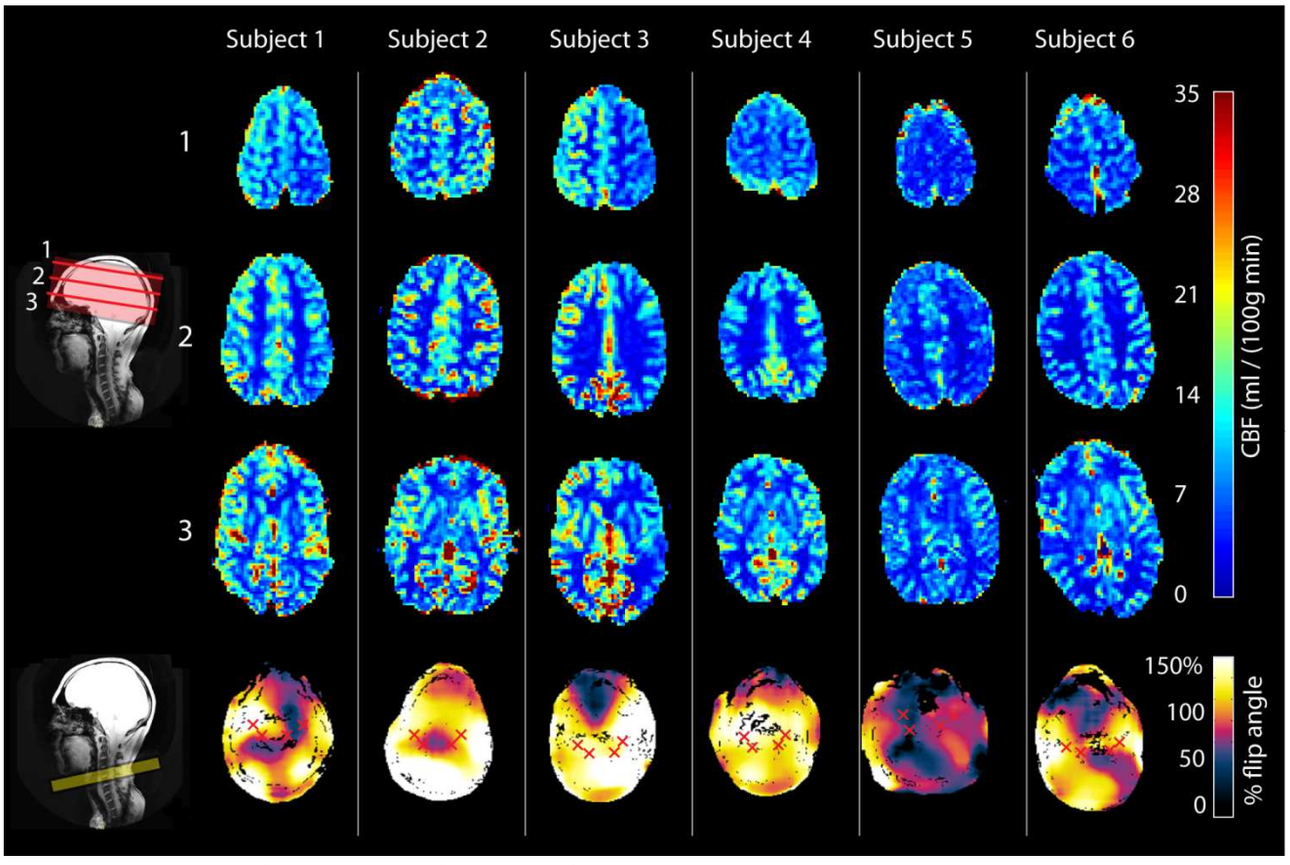

Figure 4.3 Three slices of cerebral blood flow maps of all six volunteers, post label delay = 2000 ms, 30 averages. The bottom row shows the AFI maps of the middle slice of the label slab of the corresponding subjects. The red crosses show the location of the left and right carotid and vertebral arteries. These locations were used as target in the B1+ shim procedure. Subject 5 shows poor CBF maps as well a low B1+ at the label areas.

Since the average CBF values found in the subjects were relatively low, the stability of the individual subtraction pairs was examined, which are shown for subject #2 in Figure 4.4. It shows the great variability between the individual subtraction maps during the multiple repetitions, as pointed out by the green and the red square, which indicate two extremes.

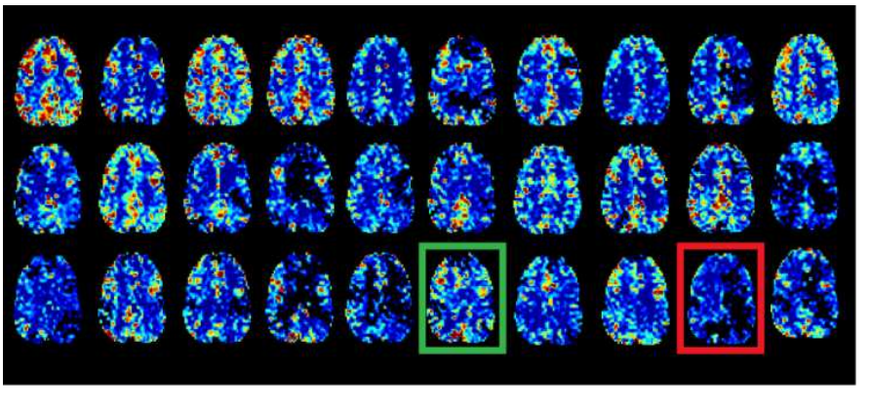

Figure 4.4 All 30 individual subtraction pairs of one slice of a pulsed ASL experiment with label delay of 2000ms in a 30 y.o. male (subject #2), showing considerable variation between maps with higher (green box) and lower (red box) perfusion weighted signal.

In Figure 4.5 the paced CBF maps (Figure 4.5a) are shown together with the three reconstructions of the free respiration CBF maps: the average of all repetitions (Figure 4.5b), the average of the repetitions with a low $\Delta\phi_R$ between control and label (Figure 4.5c) and the average of the repetitions with a high $\Delta\phi_R$ between control and label (Figure 4.5d). A sample of the corresponding respiration logging is shown in Figure 4.5e and f. Figure 4.5g shows a CBF map acquired with PASL with paced respiration, corresponding to the respiration logging shown in Figure 4.5e. Figure 4.5b-d show the three reconstructions of the free breathing PASL scans, corresponding to the respiration logging shown in Figure 4.5f. As a measure for instability, Figure 4.5g shows the mean variance and mean perfusion averaged over subjects #1-6. No significant difference was observed between the CBF maps obtained with respiratory pacing, and those obtained from the free breathing scans with different reconstructions.

In Figure 4.6 and Figure 4.7 the results of the explorative experiments (#3 in Methods) are shown to illustrate the potential of 7T ASL with an additional labeling coil. Figure 4.6 shows that it is possible to obtain signal at long PLD's. In Figure 4.1 three slices of the CBF maps of subject #4, acquired with the PLD of 2000, 3000 and 4000ms respectively, are shown. Even at a PLD of 4000ms, still perfusion is measured, although the quantified CBF value was lower.

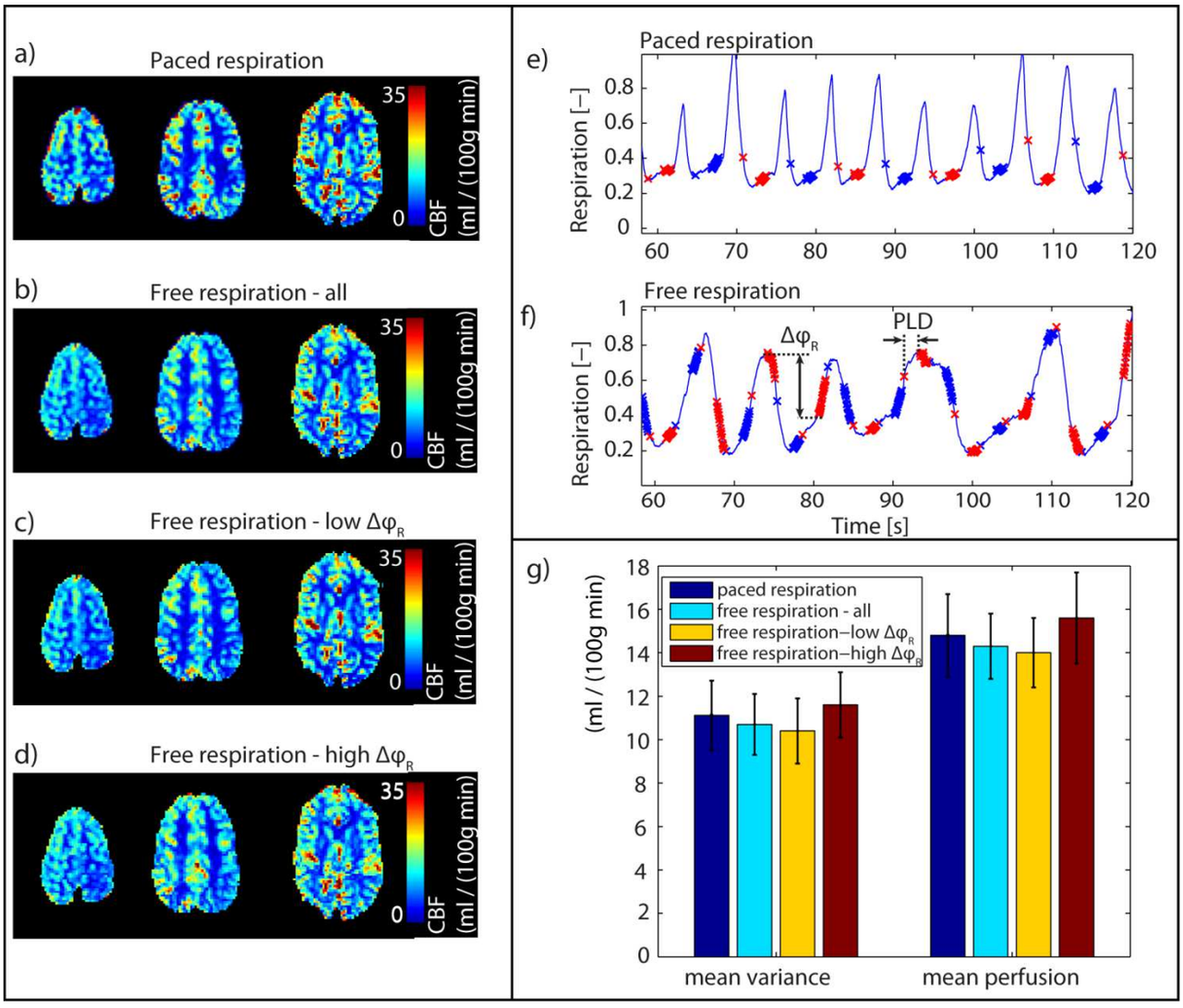

Figure 4.5 Respiration dependency of pulsed ASL perfusion maps. Two identical ASL experiments are shown in this figure, one performed with paced respiration a) and one with free respiration b) – d). e)-f): respiration logging with annotated time points of labeling and the 15 slices EPI readouts for label (red) and control (blue). In case of paced respiration all dynamics were averaged and the resulting CBF maps is shown in a). In case of free respiration, the total perfusion maps are reconstructed in three different ways: b) all dynamics averaged, c) the 50% of dynamics with the lowest ΔϕR between control and label are averaged, and d) the 50% of dynamics with the highest ΔϕR between control and label are averaged. g) A measure for instability: the mean variance and mean perfusion over the middle slice for the four perfusion maps as in a)-d), averaged over subject #1-6.

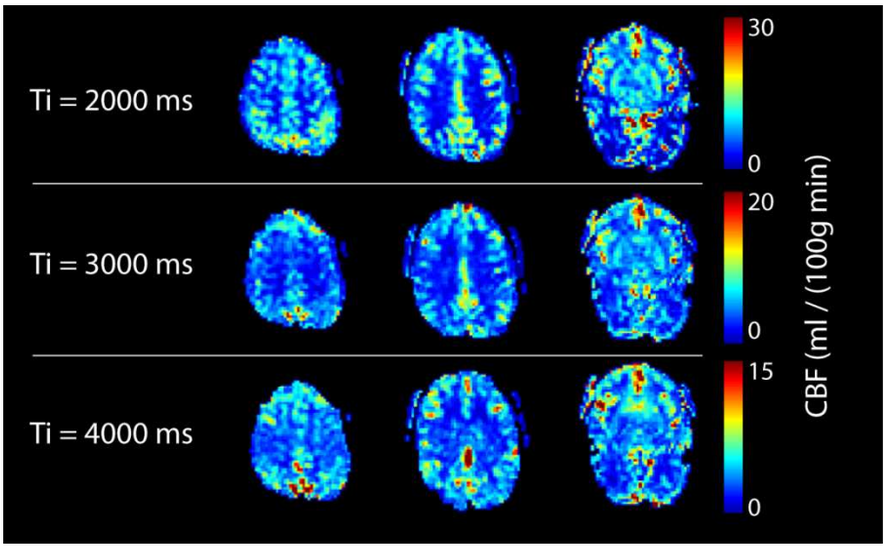

Figure 4.6 CBF maps of subject #4 (29 y.o female) acquired with pulsed ASL, using a post label delay of 2000, 3000 and 4000 ms. At all three inversion delays CBF is of a measurable value. However, note the different axes scale for each label delay, indicating that lower perfusion values were obtained at longer post labeling delays.

Figure 4.7 shows that multiple transmit elements could be used to obtain territorial ASL by B_1^+ shimming. Two shim configurations are demonstrated of which the transversal B_1^+ maps are shown in Figure 4.7d and e. In both shim configurations, both antennas are transmitting. Phases and amplitudes are set in such way to achieve maximal B_1^+ on one side, while phase cancelation nulls the B_1^+ on the opposite side. The combined result of the two scans is shown in Figure 4.7h.

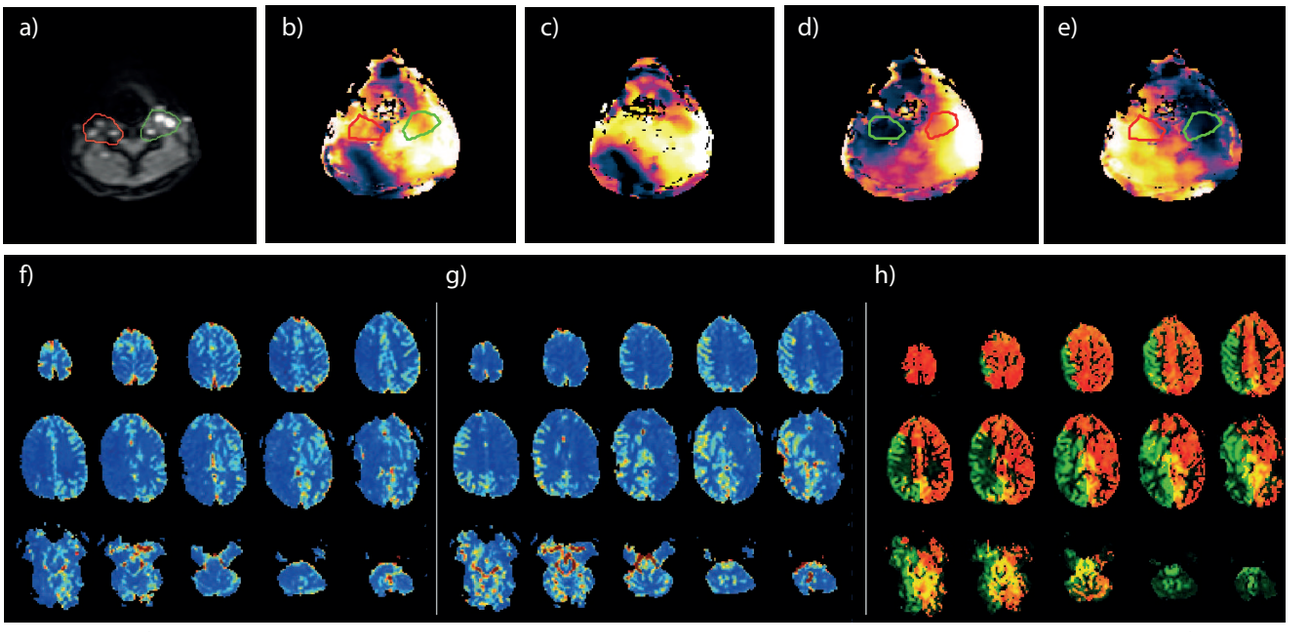

Figure 4.7 B_1^+ shimmed territorial labeling. a) shows the anatomical image used for the subject specific B_1^+ shim procedure, (b) predicted and (c) actually measured B_1^+ map for bilateral labeling, (d) and (e) show measured B_1^+ maps for selective labeling of left (d) and right (e) arteries, resulting in maps shown in (f) and (g), respectively. The combined territorial map from (f) and (g) is shown in (h).

4.4 Discussion and conclusion

Using a multi transmit approach for ASL at 7T with elements extended towards the neck, the SAR in the brain can be reduced by an order of magnitude, enabling ASL at 7T within SAR limits, and without the restriction to place the label slab too close to the brain. Feasibility of pulsed ASL was shown in healthy subjects using a waveguide neck transmitter. The waveguide transmitter allowed for combined scanning with the 7T head coils without significant coupling. The highly distributed and controllable B_1^+ in the neck assured flexible placement of the waveguide transmitter. B_1^+ Shimming was performed to control the B_1^+ field in the neck. Resulting shim settings (phases and amplitudes) showed large variations due to the high sensitivity on neck size and artery positions. Therefore subject specific shimming was necessary. The B_1^+ field was optimized only for the locations of the four main feeding arteries. There can be multiple shim configurations that lead to a good B_1^+ profile at those four locations. The neck shape and artery locations determine which solution is the best, explaining the difference of the resulting B_1^+ profile between subjects.PASL was performed with label slabs of 100 mm thickness, positioned low enough to avoid interference with the lower parts of the brain. Positioning the label slab (PASL) or slice (pCASL) low enough to enable whole brain ASL cannot be achieved using a head coil only without running into peak power limitations (PASL) or increasing the SAR dramatically (pCASL).

Using a standard head coil for pCASL at 7T would allow for a labeling duration of only 561 ms at the height of the C2 vertebrae at a T_R of 6 sec. With the additional waveguide neck transmitter, SAR limitations still would allow pCASL with a labeling duration up to 1725ms at a T_R of 6s. If the low coupling between head and neck coil, in combination with separated B_1^+ fields of the head and the neck coil, indeed results in the absence of MT effects (not assessed in this study), then the allowed label time would be approximately doubled. The low B_1^+ efficiency using a head coil only, hinders 7T ASL to benefit from the expected gain in SNR, due to reduced time efficiency (long T_R) or a severely reduced tagged blood volume, either by too narrow label slab (PASL) or by too short label times (pCASL). Using a head coil extended with additional transmitters in the neck, 7T ASL is ready to explore the expected benefits associated with the increased field strength, such as a potentially increased resolution, and longer post label delays.

4.4.1 Instability and respiration

Arterial spin labeling is a technique that relies on the subtraction of image pairs and is therefore sensitive to signal instabilities. This makes it a challenging technique, particularly at 7T, where substantial variations in B_0 can be observed. Indeed, instabilities of the subtracted images have been observed in this research. This may be caused by respiration induced B_0 changes in the brain due to respiration (35, 36). Susceptibility effects are increased at 7T, and therefore different chest volumes may cause B_0 variations in the brain. These variations in turn may influence the EPI

readout that has a very small bandwidth in phase encoding direction, causing differences between the control and label images. However, from the results shown in this paper, we could not significantly correlate these instabilities to respiration, and therefore this remains an issue to be solved. Background suppression or alternative readout schemes can be the next step to tackle these challenges.

4.4.2 Potential applications of 7T ASL

The increased T_1 at 7T should allow for increased post label delays. A post label delay increased from 2000ms to 3000 and 4000ms, although yielding lower CBF values, still clearly yielded perfusion weighted signal in a single subject. However, it requires further investigation to determine the maximal post label delay for which useful perfusion maps can be obtained.

Another opportunity of a 7T multi transmit design with an extension to the neck is RF shimmed territorial mapping. Methods for territorial mapping have previously been published (37, 38), and a theoretical framework for multi transmit territorial labeling has been described earlier (39). As proof of concept, we demonstrated territorial B_1^+ shimmed ASL. The positioning of the two channels in the neck array was optimized for a total B_1^+ coverage of the brain feeding arteries in the neck, and not for alternative shim configurations required to do RF shimmed selective excitation of separate arteries. An increased number of elements increases the degrees of freedom for controlling the B_1^+ field, and may result in a higher level of selectivity. Particularly when combining RF shimmed selection with one of the existing gradient based methods at 7T, territorial mapping may even be more selective and time efficient. The versatility in using RF shimming for either high resolution MRI of the neck or low SAR ASL may be an advantage when using the waveguide transmitter.

4.4.3 B_0 and B_1 inhomogeneities

There are reported challenges for labeling concerning the (static) B_0 offsets in the neck. At 7T these offsets can be substantial due to the use of 3rd order shim gradients to shim the B_0 in the brain, as is shown in Figure 2c. In PASL this caused a problem when the offset was higher than the bandwidth of the inversion pulse. The additional F0 determination in the neck was sufficient to tackle this problem. For pCASL, however, this is more challenging. For pCASL it is known that apart from a B_0 offset, alsothe blood flow in combination with the longitudinal gradient in B_0 in the feeding arteries, may cause problems in synchronizing subsequent sub pulses of the pseudo continuous label pulse. A low resolution prescan (16) to measure optimal phase offset between pulses, or a correction gradient to compensate the B_0 inhomogeneity (40), have been proposed to tackle this challenge. This should be subject of further research to also perform pCASL with external labeling at 7T. CASL could be a first step, since it is less sensitive to B_0 variations, though less efficient than pCASL (19, 20). The relatively large B_1^+ non-uniformity along the feet head direction (see Figure 4.2b) does not allow for background suppression by means of spin inversion.

While background suppression has shown to be beneficial for ASL (41), it will also attenuate the perfusion signal if the labeled blood is still in low B_1^+ region when background suppression is applied (42). A homogeneous RF transmit field between head and neck would enable efficient background suppression. Standard available multi-element RF transmit coils covering head and neck would therefore greatly benefit 7T ASL, but also other fields like angiographic neuro imaging.

4.4.4 Conclusion

It has been shown that using an additional external labeling coil next to the head coil allows for whole brain ASL at 7T and removes the limitations caused by the low B_1^+ efficiency when using a volume head coil only, which was restricting 7T ASL from benefiting from the potential gains of the high field strength. It has already been shown in this proof of concept that a post label delay up to 4000ms is feasible at 7T, and that a localized multi transmit approach allows for territorial mapping, but most importantly: a better power distribution. Using multi-element RF transmit coils, RF power can be directed to the label region separately, keeping SAR at a minimum. Head coil improvements with extensions towards the neck will enable to get the true benefit out of ASL at 7T.

References

1 **Williams DS, Detre JA, Leigh JS, Koretsky AP** Magnetic resonance imaging of perfusion using spin inversion of arterial water. Proc Natl Acad Sci USA 1992; 89: 212–216

2 **Detre JA, Leigh JS, Williams DS, Koretsky AP** Perfusion imaging. Magn Reson Med 1992; 23(1): 37–45

3 **Golay X, Hendrikse J, Lim TCC** Perfusion imaging using arterial spin labeling. Top Magn Reson Imaging 2004;15(1): 10–27

4 **Petersen ET, Zimine I, Ho Y-CL, Golay X** Non-invasive measurement of perfusion: a critical review of arterial spin labeling techniques. The British journal of radiology 2006; 79(944): 688–701

5 **Hendrikse J, van Osch MJP, Rutgers DR, Bakker CJG, Kappelle LJ, Golay X, van der Grond J** Occlusion Assessed at Pulsed Arterial Spin-labeling Perfusion MR Imaging at Multiple Delay Times. Radiology 2004; (233): 899–904

6 **Restom, K, Behzadi, Y, Liu, TT** (2006). Physiological noise reduction for arterial spin labeling functional MRI. NeuroImage, 31(3), 1104–15

7 **van Osch MJP, Teeuwisse WM, van Walderveen MAA, Hendrikse J, Kies DA, van Buchem MA** Can arterial spin labeling detect white matter perfusion signal? Magn Reson Med 2009; 62(1):165–73

8 **van Gelderen P, de Zwart JA, Duyn JH** Pittfalls of MRI measurement of white matter perfusion based on arterial spin labeling. Magn Reson Med. 2008; 59(4): 788–95.

9 **Wang J, Alsop DC, Li L, Listerud J, Gonzalez-At JB, Schnall MD, Detre JA** Comparison of quantitative perfusion imaging using arterial spin labeling at 1.5 and 4.0 Tesla. Magn Reson Med 2002; 48(2): 242–54

10 **Zhang X, Petersen ET, Ghariq E, De Vis JB, Webb a G, Teeuwisse WM, Hendrikse J, van Osch MJP** In vivo blood T(1) measurements at 1.5 T, 3 T, and 7 T. Magn Reson Med 2012; doi: 10.1002/mrm.24550

11 **van der Zwaag W, Francis S, Head K, Peters A, Gowland P, Morris P, Bowtell R** fMRI at 1.5, 3 and 7 T: characterising BOLD signal changes. NeuroImage 2009; 47(4): 1425–34.

12 **Rooney, WD, Johnson, G, Li, X, Cohen, ER, Kim, SG, Ugurbil, K, Springer, CS** Magnetic field and tissue dependencies of human brain longitudinal 1H2O relaxation in vivo. Magn Reson Med 2007; 57: 308–318.

13 **Gardener AG, Gowland PA, Francis ST** Implementation of quantitative perfusion imaging using pulsed arterial spin labeling at ultra-high field. Magn Reson Med 2009; 61(4): 874–82.

14 **Teeuwisse WM, Webb AG, van Osch MJP** Arterial spin labeling at ultra-high field: All that glitters is not gold. Int J Imag Syst Tech 2010; 20(1): 62–70.

15 **Ghariq E, Teeuwisse WM, Webb AG, van Osch MJP** Feasibility of pseudocontinuous arterial spin labeling at 7 T with whole-brain coverage. MAGMA 2012; 25(2): 83–93

16 **Luh WM, Talagala SL, Li TQ, Bandettini PA** Pseudo-continuous arterial spin labeling at 7 T for human brain: estimation and correction for off-resonance effects using a Prescan. Magn Reson Med 2013; 69(2): 402–10

17 **Schepers J, van Osch MJP, Bartels LW, Heukels SN, Viergever MA, Nicolay K**. The effect of B1 field inhomogeneity and the nonselective inversion profile on the kinetics of FAIR-based perfusion MRI. Magn Reson Med 2005; 53(6): 1355–62

18 **Alsop DC, Detre JA** Reduced Transit-Time Sensitivity in Noninvasive Magnetic Resonance Imaging of Human Cerebral Blood Flow. J Cereb Blood Flow Metab 1996; 16: 1236–1249

19 **Wu WC, Fernández-Seara M, Detre JA, Wehrli FW, Wang J** A theoretical and experimental investigation of the tagging efficiency of pseudocontinuous arterial spin labeling. Magn Reson Med 2007; 58: 1020–7

20 **Dai W, Garcia D, de Bazelaire C, Alsop DC** Continuous flow-driven inversion for arterial spin labeling using pulsed radio frequency and gradient fields. Magn Reson Med 2008; 60: 1488–97

21 **Wong EC, Buxton RB, Frank LR** A Theoretical and Experimental Comparison of Continuous and Pulsed Arterial Spin Labeling Techniques for Quantitative Perfusion Imaging. Magn Reson Med 1998; 40: 348–355

22 **Buxton RB, Frank LR, Wong EC, Siewert B, Warach S, Edelman RR** A general kinetic model for quantitative perfusion imaging with arterial spin labeling. Magn Reson Med 1998; 40: 383–96

23 **Talagala SL, Ye FQ, Ledden PJ, Chesnick S** Whole-Brain 3D Perfusion MRI at 3.0 T Using CASL With a Separate Labeling Coil. Magn Reson Med 2004;52:131–140

24 **Koning W, Bluemink JJ, Langenhuizen EAJ, Raaijmakers AJ, Andreychenko A, van den Berg CAT, Luijten PR, Zwanenburg JJM, Klomp DWJ** High-resolution MRI of the carotid arteries using a leaky waveguide transmitter and a high-density receive array at 7 T. Magn Reson Med 2013; 69: 1186–93

25 **Yarnykh VL** Actual flip-angle imaging in the pulsed steady state: a method for rapid three-dimensional mapping of the transmitted radiofrequency field. Magn Reson Med 2007; 57: 192–200

26 **Adriany G, Van de Moortele P-F, Wiesinger F, Moeller S, Strupp JP, Andersen P, Snyder C, Zhang X, Chen W, Pruessmann KP, et al** Transmit and receive transmission line arrays for 7 Tesla parallel imaging. Magn Reson Med 2005; 53: 434–45

27 **Schär M, Kozerke S, Fischer SE, Boesiger P** Cardiac SSFP imaging at 3 Tesla. Magn Reson Med 2004; 51: 799–806

28 **Golay X, Petersen ET, Hui F** Pulsed star labeling of arterial regions (PULSAR): a robust regional perfusion technique for high field imaging. Magn Reson Med 2005; 53: 15–21

29 **Ogg RJ, Kingsley PB, Taylor JS** WET, a T1- and B1-insensitive water suppression method for in vivo localized 1H NMR spectroscopy. J Magn Reson 1994; 104:1–10

30 **Edelman RR, Chen Q** EPISTAR MRI: Multislice Mapping of Cerebral. Magn Reson Med. 1998; 40: 800–805

31 **Wong EC, Buxton RB, Frank LR** Implementation of quantitative perfusion imaging techniques for functional brain mapping using pulsed arterial spin labeling. NMR biomed 1997; 10: 237–49

32 **Yongbi MN, Branch CA, Helpern JA** Perfusion imaging using FOCI RF pulses. Magn Reson Med 1998; 40: 938–943

33 **Jorge, J, Figueiredo, P, Van der Zwaag, W, Marques, JP** (2013). Signal fluctuations in fMRI data acquired with 2D-EPI and 3D-EPI at 7 Tesla. Magnetic resonance imaging, 31(2), 212–20

34 **Buxton, RB.** Quantifying CBF with arterial spin labeling. J Magn Reson Imaging 2005; 22: 723–726

35 **van Gelderen P, de Zwart JA, Starewicz P, Hinks RS, Duyn JH** Real-time shimming to compensate for respiration-induced B0 fluctuations. Magn Reson Med 2007; 57: 362–8

36 **Boer VO, Klomp DWJ, Juchem C, Luijten PR, de Graaf RA** Multislice 1H MRSI of the human brain at 7 T using dynamic B0 and B1 shimming. Magn Reson Med 2012; 68: 662–670

37 **Hartkamp NS, Petersen ET, De Vis JB, Bokkers RPH, Hendrikse J** Mapping of cerebral perfusion territories using territorial arterial spin labeling: techniques and clinical application. NMR biomed 2012 doi:10.1002/nbm.2836

38 **Paiva FF, Tannús A, Talagala SL, Silva AC** Arterial spin labeling of cerebral perfusion territories using a separate labeling coil. J Magn Reson Imaging 2008; 27: 970–7

39 **Yoon D, Jahanian H, Noll DC, Hernandez-Garcia L** Spatially Selective PCASL with Parallel Excitation. Proceedings of Int Soc Magn Reson Med 2011, Montreal, Canada

40 **Jahanian H, Noll DC, Hernandez-Garcia L** B0 field inhomogeneity considerations in pseudo-continuous arterial spin labeling (pCASL): effects on tagging efficiency and correction strategy. NMR Biomed 2011; 24: 1202–9

41 **Ye FQ, Frank JA, Weinberger DR, McLaughlin AC** Noise reduction in 3D perfusion imaging by attenuating the static signal in arterial spin tagging (ASSIST). Magn Reson Imaging 2000; 44: 92–100

42 **Garcia DM, Duhamel G, Alsop DC** Efficiency of inversion pulses for background suppressed arterial spin labeling. Magn Reson Med 2005; 54: 366–72

Chapter 5

Blood signal suppression for carotid MRI at high field with local excitation coils

W. Koning, T.A. van der Velden,
P.R. Luijten, D.W.J. Klomp, J.J.M. Zwanenburg

Abstract

The purpose of this study was to explore and evaluate methods for blood signal suppression in carotid MRI at high field when using local transmit coils. Seven methods for blood signal suppression were evaluated, abbreviated as SAT, iMSDE, PSDIR, PSSIR, DANTE, TSE and STEAM. Each of the suppression methods were implemented on a 7T MRI and tested in a non-pulsatile flow phantom model. Both flow suppression and static tissue signal preservation were measured for all methods, and related to the fluid velocities, ranging from 10 to 89 cm/s. The sensitivity of static tissue signal to B_1^+ as well as the increase in specific absorption rate (SAR) was quantified for each method. Finally, single slice images were acquired in vivo with all suppression methods. Based on the quantitative analysis in the flow phantom model, it was concluded that STEAM, PSDIR and PSSIR are the most promising methods for further optimization for *in vivo* application.

5.1 Introduction

Imaging the carotid arteries is important for the risk assessment of atherosclerotic plaques. A good risk assessment is important for the clinical management of patients with atherosclerotic lesions in the carotids. Acquisition of the degree of stenosis alone, now the only parameter used for intervention decisions, has shown not to be sufficient for a proper risk assessment, also the composition of the plaque is essential for this purpose (1, 2). MRI is a promising imaging modality to acquire this plaque composition. At a field strength of 1.5T and 3T several plaque components can be detected, like intra-plaque hemorrhage, a thin fibrous cap, and a lipid-rich necrotic core. These components have been correlated to stroke events (3, 4). The presence of a high blood signal can obscure these plaque components, and flow artefacts in the lumen can mimic plaques (5). A good suppression of the blood signal is therefore vital for reliable plaque analysis.

5.1.1 Blood signal suppression challenge at 7T

Carotid plaque imaging with MRI at ultra-high field (7T and up) is a challenge for reasons related to the increased Larmor frequency. In the absence of a transmit body coil at 7T, local transmit coils have to be used. An eight-channel transmit receive array was proposed (6) and in a later study we proposed and developed a separate transmit and receive array to reduce SAR and to increase receive sensitivity (7). However, all these transmit solutions focus the transmit field very locally as compared to the body coils integrated in the 3T and lower field strengths MR scanners. This poses a problem for blood signal suppression. The most conventional and effective blood signal suppression method is called Double Inversion Recovery (DIR) (8) or a Quadruple Inversion Recovery (QIR) (9). The principle of DIR is as follows: a non-selective inversion is followed by a slice- or slab selective inversion in the imaging slice or volume. As a result, the imaging slice/volume ends up non-inverted while the inflowing blood is inverted. A substantial “waiting time” is added after the inversion (inversion delay), typically $>$500ms, during which the inverted blood flows into the imaging slice or volume. After this specific inversion delay, the net longitudinal magnetization of the blood is zero, and the measurement is performed, resulting in a black blood signal. The limited longitudinal B_1^+ coverage at 7T will result in a smaller volume of inverted blood, which may therefore completely pass the area of interest before the imaging readout starts (see Figure 5.1). The increase of blood T1 relaxation time at 7T (10) even increases the required coverage, since the inversion delay required for nulling the blood is consequently increased as well. This implies the blood will travel even a greater distance during the signal-nulling delay, and is more likely to flow out of the image slice before being imaged. A straightforward alternative to create black blood images is a TSE sequence (7, 11). However, with a TSE sequence it is difficult to acquire a pure T_1 weighted image, because SAR restrictions prohibit a short T_R and the echo train introduces T_2 contamination (12). Acquiring black blood images with heavy T_1 weighting (an important contrast for plaque imaging and intraplaque

hemorrhage detection (13)), therefore, requires alternative blood signal suppression methods for 7T.

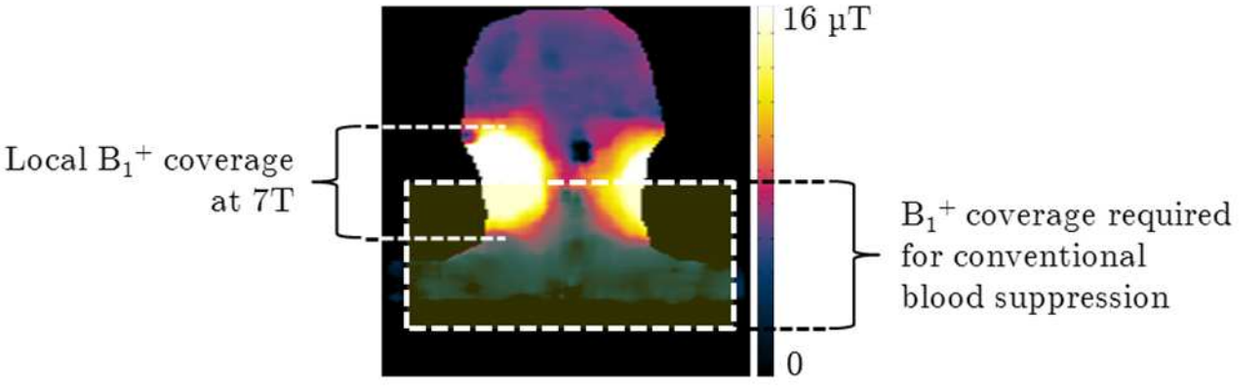

Figure 5.1 A local B_1^+ field that is sufficient for imaging the carotid artery, but does not reach far enough to apply the conventional (DIR) blood signal suppression pre-pulses.

5.1.2 Blood signal suppression methods

Even though widely used, the DIR (or similar) methods are not the only blood signal suppression methods that have been reported. The methods for blood signal suppression can roughly be divided in four groups with different mechanisms for blood signal suppression:

1. *Blood nulling by inversion or saturation* (8, 14). Before the blood passes the region of interest, it is saturated or inverted (DIR) in a large slab prior to the slices of interest.
2. *Motion dependent phase dispersion* (15-18). In these mechanisms a combination of field gradients and RF pulses are applied in a way to create a signal loss by phase dispersion in voxels that undergo motion, while static voxels are rephrased and therefore remain their signal.
3. Techniques based on *phase sensitive reconstruction* (17,19) typically use an inversion pulse to create a 180° phase difference between flowing blood and static tissue.
4. *spin echo refocusing*. With this we solely refer to the intrinsic blood signal suppression property of a spin echo sequence, meaning that only tissue that has received both excitation and refocusing pulse, will create a detectable echo.

5.1.3 Aim

The aim of this paper is to evaluate techniques for blood signal suppression in the carotid artery at 7T. Even though various methods for blood signal suppression have been reported, it remains unclear how these methods perform at high field using local excitation coils. In this research, we inventoried all blood signal suppression methods that do not need a (large) preparation volume

outside the reach of the local excitation coils. These reported methods, plus two new methods that we introduce in this paper, will be evaluated on a phantom flow model of a carotid artery, while using a local transmit coil at 7T, and tested on the following criteria:

1. suppression performance
2. static tissue signal preservation,
3. sensitivity to B_1^+ inhomogeneity and
4. specific absorption rate (SAR).

5.2 Theory

In this section the underlying mechanism of each of the seven evaluated methods, as they are applied in this research, are described. The following aspects will be briefly discussed for each method: the suppression *mechanism* is explained, the potentially unwanted but inevitable *induced contrast* weighting in the static tissue is described, and finally the requirement of *additional B_1^+ coverage* adjacent to the slice of interest is discussed. This is all summarized in Table 3.

5.2.1 Regional saturation

Regional saturation is the first reported blood signal suppression technique and was described by Felmlee et al in 1987 (14) as a method to improve 'the blackness of the flow voids in vessels and cardiac chambers.' Nowadays this method is known as Regional Saturation Technique (REST or SAT). *Mechanism:* a slice selective excitation pulse is applied proximal to the slice of interest followed by a crusher gradient. Then the saturated spins flow into the slice of interest and will not produce a signal when imaging the slice. *Induced contrast:* There is no direct induced contrast, but when high B_1^+ values and short T_R is used for the saturation slab, the contrast in the imaging slice might be affected by magnetization transfer (MT) effects. *Additional B_1^+ coverage:* The saturation method requires additional B_1^+ coverage adjacent to the slice of interest. The reach of the B_1^+ field determines the maximum size of the saturation slab and thus the maximum time to acquire readouts before distal, non-saturated blood will enter the imaged tissue.

5.2.2 MSDE / iMSDE

The use of a diffusion preparation pulse (15) for blood signal suppression was proposed by Wang et al. (16) and named Motion-Sensitized Driven-Equilibrium (MSDE). *Mechanism:* A flow-suppression preparation is applied that consists of a 90° pulse, a single 180° refocusing pulse and a -90° pulse. All pulses are non-slice-selective pulses. A symmetric gradient pair is surrounding the 180° pulse. A spoiler gradient is applied and followed by the imaging part of the sequence. The spins of the static tissue will refocus after the 180° pulse and will be placed back in the longitudinal direction by the third pulse. The moving spins will refocus as well, but the phase will depend on the displacement of the spin. As a voxel contains spins with different speeds there is no phase

coherence inside the voxel. This leads to a net longitudinal magnetization of 0 after the -90° pulse. This results in a suppression of the signal of the flowing spins. The improved MSDE (17) is the same but uses two instead of one 180° pulses. Because there is a pair of refocusing pulses, these pulses can be adiabatic, making it less sensitive to B_1^+ inhomogeneity's (20). The gradients are replaced by two sets of bipolar gradients to reduce the effects of eddy currents. *Induced contrast*: T_2 weighting and diffusion weighting is introduced in the static tissue by the preparation pulse. The strengths of these effects depend on the duration of the preparation and on the gradient strength. *Additional B_1^+ coverage:* (i)MSDE requires additional B_1^+ coverage adjacent to the slice of interest. The reach of the B_1^+ field (see Figure 5.1) determines the maximum size of the prepared slab in which the blood signal is crushed and thus the maximum time to acquire readouts.

5.2.3 PSDIR

Mechanism: Phase Sensitive Double Inversion Recovery (PSDIR), described by Abd-Elmoniem et al. (19), is a flow suppression preparation that consists of two inversion pulses. The first pulse is a slice-selective inversion pulse, while the second is a non-slice-selective inversion pulse. This results in a slice with normal magnetization, while the rest of the volume has an inverted magnetization. Instead of waiting until the inverted blood passes the longitudinal zero point (as in DIR), the imaging starts as soon as inverted blood has flown into the imaging slice. As the blood and the static tissue have opposite magnetizations (Figure 5.2), a phase difference of $180°$ will be present between the two, which can be measured by phase sensitive reconstruction.

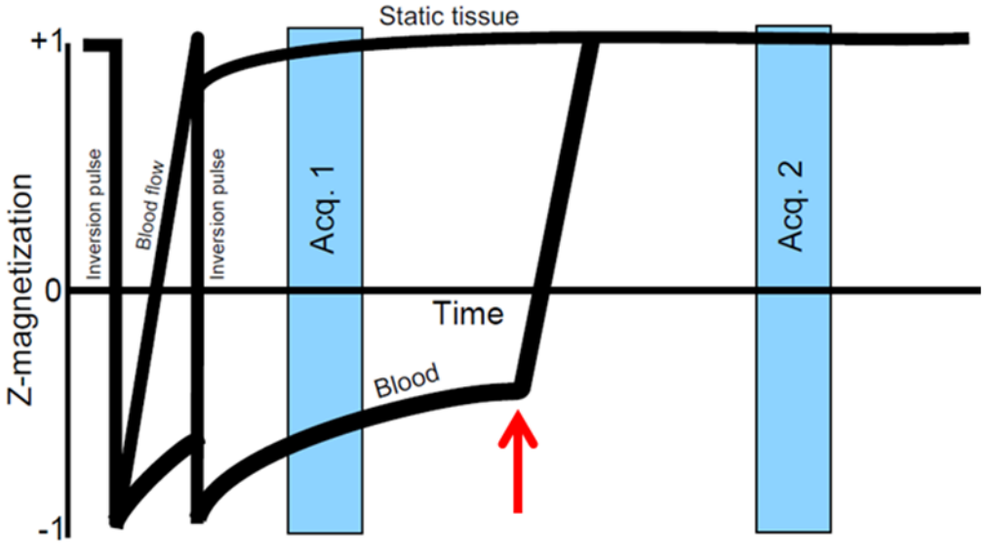

Figure 5.2 Schematic overview of the longitudinal magnetization of static tissue and flowing blood during a PSDIR experiment. During acquisition 1, the phases of the blood and the static tissue are opposite. During acquisition 2, the phases of the blood and the static tissue are equal. The red arrow corresponds to the end of the B_1^+ coverage, since at that time point, uninverted blood flows into the slice.

In contrast to Abd-Elmoniem et al., we adapted this sequence by adding a second identical scan without the non-selective inversion pulse. The magnitude of the summed complex signals of both acquisitions is calculated in each pixel (see Equation 1):

$$I(x,y) = \left| M_1(x,y)e^{i(\varphi_1(x,y))} + M_2(x,y)e^{i(\varphi_2(x,y))} \right| \quad (1)$$

Where *I(x,y)* is the eventual intensity in pixel *(x,y)*, M_1 and M_2 are the pixel magnitudes during acquisition 1 and 2, respectively, and φ_1 and φ_2 are the pixel phases in acquisition 1 and 2, respectively. For the static tissue this results in an extra signal average. For the flowing blood this results in signal cancelation because the phase of the blood is opposite in the two instances. *Induced contrast*: there is no induced contrast, since the static tissue is net unaffected after two inversion pulses, although the two (potentially adiabatic) inversions may induce MT effects. *Additional B_1^+ coverage:* Even though PSDIR needs only a much smaller coverage than the conventional DIR (as one does not need to wait till the blood signal is nulled), still it requires additional B_1^+ coverage adjacent to the slice of interest. The reach of the B_1^+ field (see Figure 5.1) determines the maximum size of the inverted slab and thus the maximum time to acquire readouts.

5.2.4 PSSIR

We introduce Phase Sensitive Single Inversion Recovery (PSSIR) as a flow-suppression preparation that uses only a single slice-selective inversion pulse. *Mechanism:* The magnetization of the spins in the slice of interest is inverted. After a small delay, where non-inverted blood has time to flow into the slice of interest, the readout is acquired. To obtain a normal, non-inverted, contrast and to remove the background phase differences, every line in k-space is measured a second time, but without the pre-pulse. As the static tissue has an inverted magnetization and the blood has not, a phase difference will be measured (Figure 5.3).

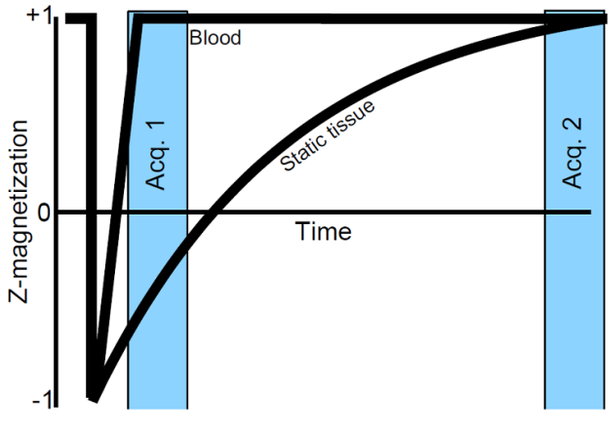

Figure 5.3 Schematic overview of the longitudinal magnetization of static tissue and flowing blood during a PSSIR experiment. During acquisition 1, the phases of the blood and the static tissue are opposite. During acquisition 2, the phases of the blood and the static tissue are equal.

To retrieve the image with suppressed blood signal, the image is reconstructed pixel by pixel with Equation 2:

$$I(x,y) = -1 \cdot Re\left(|M_2(x,y)| \cdot e^{i(\varphi_1(x,y)-\varphi_2(x,y))}\right) \quad (2)$$

where $I(x,y)$ is the eventual intensity in pixel (x,y), M_2 is the pixel magnitude during acquisition 2, and φ_1 and φ_2 are the pixel phases in acquisition 1 and 2, respectively. As a result, pixels from flowing blood will be nulled. *Induced contrast*: unless the T_R is very long, there will be some introduced T_1 contrast. Note that the T_1 contrast in the first acquisition does not enter the reconstructed image, as only the signal phase of this acquisition is used. *Additional B_1^+ coverage:* PSSIR requires no additional coverage of the B_1^+ field, since only the slice of interest itself has to be inverted.

5.2.5 DANTE preparation

Dante pulse trains have been used in applications for spectroscopy (21) and MR tagging (22), and have recently been proposed for blood signal suppression (18). *Mechanism:* As a preparation before the readout, a train of block pulses with gradients in between is applied. According to a Steady State Free Precession (SSFP) mechanism, a steady state occurs. Static spins will have a constant phase increment, leading to a phase coherent steady state. Flowing spins however, have a phase increment that increases with time. This will result in a phase dispersion, or spoiling of the signal. Degrees of freedom of the DANTE train are the flip angle, the length of the pulse train and the interpulse interval. *Induced contrast*: additional T_1 weighting can be introduced (18). *Additional B_1^+ coverage:* DANTE preparation requires additional B_1^+ coverage adjacent to the slice of interest. The reach of the B_1^+ field determines the maximum size of the prepared slab and thus the maximum time to acquire readouts.

5.2.6 Turbo spin echo

Like a spin echo, a turbo spin echo is inherently blood suppressed. *Mechanism*: Only static tissue that experiences both excitation and refocusing pulses creates an echo. Flowing spins that only experience one of them do not create an echo. As long as the flowing spins that experienced the first (excitation) pulse are still in the imaging slab, the refocusing pulses do create an echo. By adding start-up echoes, these can be removed. *Induced contrast:* Addiontal T_2 weighting is introduced, depending on the flip angles of the train of refocusing pulses and the ordering in k-space. *Additional B_1^+ coverage:* No additional coverage is required.

5.2.7 STEAM

We propose to use a stimulated echo, first described by Hahn in 1950 (23), can be used to obtain a black blood image. *Mechanism*: similar as the TSE, however, instead of one excitation pulse, the sequence starts with two 90ºpulses. The second pulse puts all spins in the longitudinal state, the

so-called Z_1 state (24, 25). After that follows a series of RF pulses with flip angle α. Each of these RF pulses puts part of the phase coherent population stored in the longitudinal (Z_1) state into the transversal state, creating an echo. Consequently, the population in the Z_1 state will be depleted after a certain number of RF pulses. *Induced contrast*: where a normal TSE has inherent T_2 weighting, here every echo has a short equivalent T_E (12), and therefore no extra contrast weightings are introduced. However, there is an inherent 50% signal loss of the stimulated echo, and every next echo has reduced intensity. *Additional B_1^+ coverage:* No additional coverage is required.

Suppression method	Abbreviation	Mechanism category	Requires B_1^+ coverage proximal to imaging slice	Added contrast weighting
Regional saturation	SAT	Blood nulling by saturation	yes	none
Improved Motion Sensitized Driven Equilibrium	iMSDE	Motion dependent phase dispersion	yes	T_2
Delay Alternating with Nutation for Tailored Excitation (DANTE) - preparation	DANTE	Motion dependent phase dispersion	yes	T_1
Phase Sensitive Double Inversion Recovery	PSDIR	Phase Sensitive reconstruction	yes	none
Phase Sensitive Single Inversion Recovery	PSSIR	Phase Sensitive reconstruction	no	T_1
Turbo Spin Echo	TSE	Spin echo refocusing	no	T_2
Stimulated Echo Acquisition Mode	STEAM	Spin echo refocusing	no	none

Table 3 Overview of evaluated blood signal suppression methods, their mechanism category and basic properties.

5.3 Material and methods

5.3.1 Hardware

All methods were tested on a Philips Achieva 7.0 tesla MR scanner (Philips Healthcare, Cleveland, Ohio). A dielectric waveguide transmitter was used in combination with a 30 channel small element array, both designed for neck imaging (7).

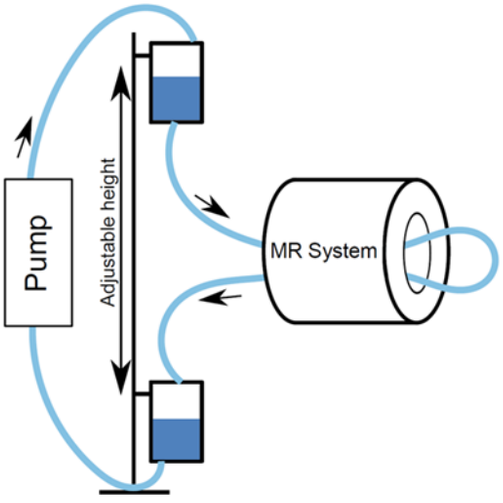

Figure 5.4 Experimental setup. The adjustable height of the column determines the amount of flow in the phantom.

5.3.2 Carotid flow model

A 1.5 l plastic bottle filled with a 3 g/l NaCl solution was used as the basis of a model for blood flow through the carotids. Through the middle of the bottle a tube with an inner diameter of 0.6cm was led, similar as the lumen diameter of an average carotid artery (26). By means of a static column pressure a constant flow between 10 and 89cm/s could be generated through the tube, by adjusting the height of the column (Figure 5.4). The static fluid in the bottle represented the tissue; the flowing fluid through the tube in the bottle represented the blood.

5.3.3 Experimental design

All quantitative experiments were performed on the phantom model. Additionally, a preliminary exploration of these techniques was applied *in-vivo*. Both in the phantom and the *in-vivo* experiments, B_0 and B_1^+ shimming was performed prior to the blood signal suppression experiments, as described before (27).

Phantom experiments: The following scans were performed in the phantom.

1. *All 7 blood suppressed sequences*. To assess the blood suppression properties of the preparation methods as pure as possible, only a basal readout was used, without accelerations by acquiring multiple k-lines per preparation. Every method, except the TSE, was acquired with a readout with the following parameters: 2D single slice gradient echo (GE), flip angle 30deg, T_R/T_E = 1000/4.5ms, FOV = 140 * 140mm^2, voxel size 0.5 * 0.5 * 2.0mm^3, readout bandwidth 504Hz. All methods, except the TSE, were tested acquiring just one k-line per preparation. In case an adiabatic inversion pulse was applied in the sequence (method 3 and 4), a hyperbolic secant pulse of 12ms length, a peak B_1^+ of 12μT

and a 1400Hz bandwidth was used. A 30ms for inflow/outflow delay was used in all methods with prepulse. Additional method specific parameters are given in Table 4.

2. *A reference scan*: an identical scan with the same parameters but without the suppression preparation. This reference scan was used to quantify the suppression efficiency.
3. *A quantitative flow map*. The flow in the tube is not homogeneous. In order to be able to correlate the suppression in a voxel to the exact speed of the fluid, a quantitative phase based flow map was acquired with the same imaging dimensions and resolution.

This whole set of scans was repeated 5 times. Each time an increased average flow in the tube was realized by using an increased height of the water column. In this way data was acquired from a flow distribution as large as possible with the given setup. Additionally, a single B_1^+ map (Actual Flip angle Imaging (AFI) (28), $T_{R,1}/T_{R,2}$ = 25/125ms, flip angle: 50º, gradient echo (GE), 220 x 220 x 55mm^3) was acquired to monitor the B_1^+ dependence of the static tissue preservation.

In vivo experiments: To give an impression of the current status of these 7 techniques when applied *in vivo*, preliminary single slice acquisitions were obtained on different healthy volunteers. The same readout parameters as used in the phantom experiments were applied. Other scan parameters are shown in Table 4.

iMSDE – prepulse:	Inversion pulses	adiabatic: hyperbolic secant
	surface per gradient	20 mT m^{-1} ms^{-1}
	prep duration	31 ms
DANTE – prepulse train:	Train length	64
	flip angle	15 deg
	pulse interval	0.8 ms

Table 4 specific sequence parameters for the iMSDE and the DANTE method.

5.3.4 Analysis

The **suppressed signal ratio** $\mathrm{SSR}(\mathrm{x},\mathrm{y})$ was defined as

$$SSR(x,y) = \frac{|S_s(x,y)|}{|S_R(x,y)|} \tag{3}$$

where $|S_s(x,y)|$ is the signal modulus of a voxel of the suppressed scan, and $|S_R(x,y)|$ is the signal modulus of a voxel in the reference scan without suppression. In all voxels the *SSR* was calculated. Consequently, SSR=0 corresponds to 100% signal *suppression*, and SSR=1 means 100% signal *preservation*. For method 6 (TSE) and 7 (STEAM), no reference was available and therefore also for these methods the unsuppressed gradient echo scan was used as reference scan S_R. The

static tissue *SSR* in the method 6 (TSE) is undefined and therefore not shown. For method 7 (STEAM) the static tissue of the TSE is used as reference S_R to calculate the *SSR* in the static tissue, because both scans are based on spin echoes.

Suppression data was organized in two ways:

1. *Flowing spins:* suppression *SSR* of voxels in the flow tube were plotted against the corresponding velocity measured in the quantitative flow measurement.
2. *Static spins*: suppression *SSR* of voxels from the static voxels outside the tube were plotted against the measured B_1^+ from the B_1^+ map. Since the phantom was positioned in a fixed place during all experiments, a perfect registration between suppression sequences, quantitative flow measurement and B_1^+ map was assumed. The effects of remaining B_0 inhomogeneity's after B_0 shimming were not studied.

5.3.5 SAR calculation

For all 7 blood suppressed imaging sequences, their proportional energy deposition was calculated by averaging the squared B_1^+ over a period of T_R = 1000ms. The resulting values were normalized by the value as calculated for the gradient echo sequence without any blood signal suppression pre-pulse (the reference scan).

5.4 Results

The calculated relative power deposition for the different suppression methods is given in Table 5:

Method	Normalized relative power deposition [-]
GRE	1
SAT	5.56
iMSDE	17.2
PSDIR	14.5
PSSIR	7.73
DANTE	15.8
TSE	12.6
STEAM	3.78

Table 5 Relative power deposition, normalized to the reference scan GRE without blood signal suppression pre-pulse.

The highest power deposition is demanded by the iMSDE sequence, which has a 17.2 fold power deposition compared to the non-suppressed gradient echo (GRE). The lowest power deposition is required for the STEAM method, with only an almost 4 fold power deposition compared to GRE.

In Figure 5.5, example images of the flow phantom experiments are shown. Figure 5.5a shows the image of the reference scan, the gradient echo without any suppression. Figure 5.5b-h show the images of the seven suppression methods. In all blood suppressed images reduced signal intensity

inside the tube can be seen, as compared to the static spins outside the tube. Also inhomogeneity's in the static tissue can be seen that are related to B_1^+, B_1^- or B_0 inhomogeneity's.

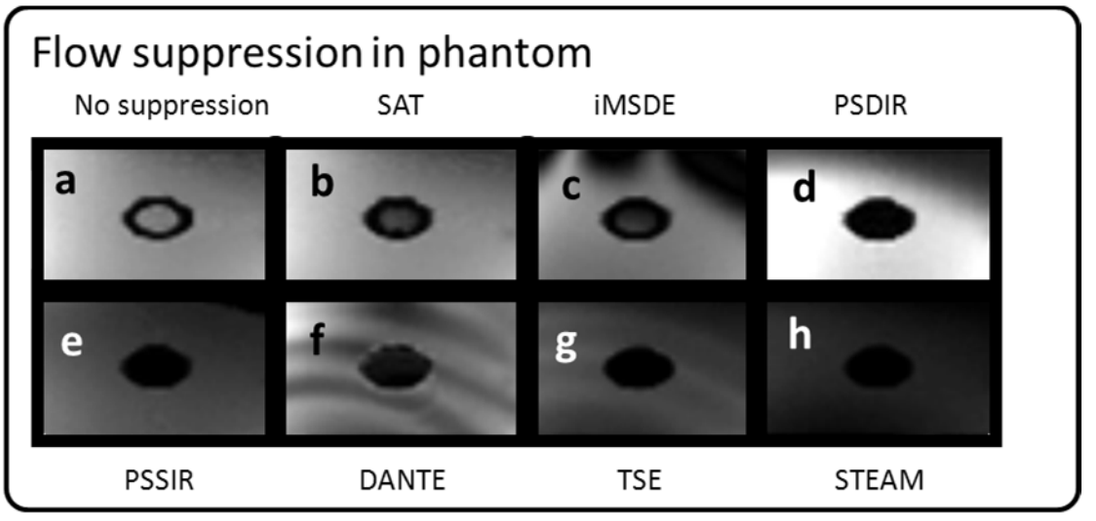

Figure 5.5 Transversal images of the flow phantom. a) Reference image: a gradient echo without any suppression pre-pulse, b)-h) show example images of the 7 different suppression methods (as listed in Table 3). The same window and level settings were applied at each image. The abbreviations of the method are listed in Table 3.

The quantified suppression *SSR* as a function of velocity is shown in Figure 5.6. Every voxel inside the flow tube is represented by a circle. A summary of the data from Figure 5.6 is shown in Figure 5.7a, where the same data is shown in a bar plot with individual voxels binned into four groups of flow ranges. With methods 3-7, the signal of flowing spins is reduced to maximal 20% for all flows, while the result with method 1 and 2 is less coherent. Method 1 (SAT) results in a highly flow dependent suppression, and method 2 (iMSDE) shows a highly distributed suppression.

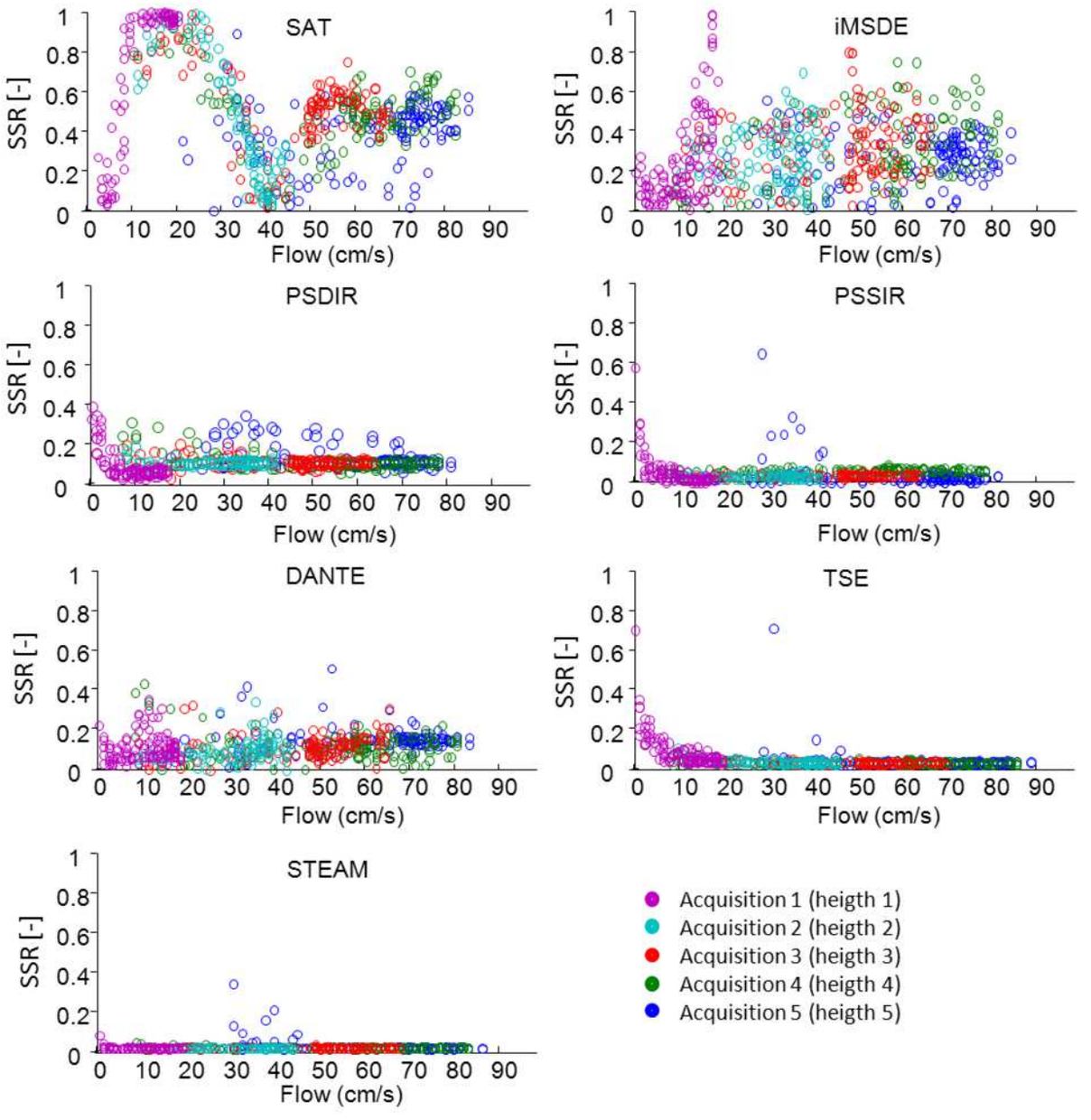

Figure 5.6 Suppressed signal ratio SSR as a function of flow. Each circle in the graphs represents a voxel in the flow tube. Five acquisitions were performed. Each acquisition is performed with a different average flow in the tube, set by the height of the water column, and measured for each pixel. The data of all the pixels of the five acquisitions with different heights were put together to achieve a flow range up to 90cm/s. A suppression of SSR=0 corresponds to 100% suppression, and SSR=1 means 0% suppression (equivalent to 100% signal preservation).

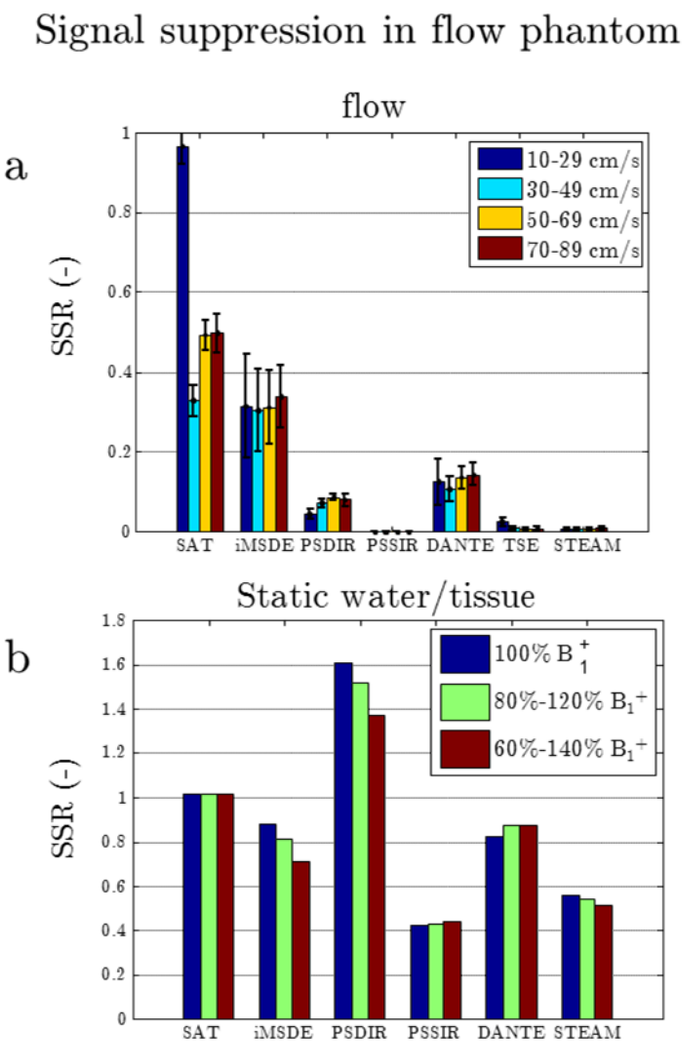

Figure 5.7 a) Flow suppression p in the flow tube for 10-29cm/s (blue), 30-49cm/s (turquoise), 50-69cm/s (yellow) and 70-89cm/s (red). *SSR*=0 means 100% suppression. b), flow suppression p in the static voxels for 100% B_1^+ (blue), 80 – 120 % B_1^+ (green) and 60-140% B_1^+ (red). A value of *SSR*=1 is optimal and means no suppression at all (equivalent to 100% signal preservation). The TSE is left out since no reference scan for the static tissue could be defined.

Figure 5.7b shows the suppression p in the static water ('tissue') outside the tube. A value of *SSR*=1 corresponds to no signal loss at all. This is only the case for method 1 (SAT), in which the preparation takes place completely outside the slice of interest, and does not affect the static tissue in the slice of interest. Figure 7b shows a value of $SSR > 1$ for the PSDIR method. This means the static signal is higher than the static signal of the reference scan. This is because in the PSDIR method an additional phase reference readout is acquired and added to the signal.

In Figure 5.8 the results of the *in vivo* experiments are shown. Figure 5.8a shows one of the reference scans, a gradient echo without any blood signal suppression. Figure 5.8b-h show the

blood suppressed images obtained in different subjects using the different techniques. In all the explored methods blood signal suppression can be observed except in the DANTE method.

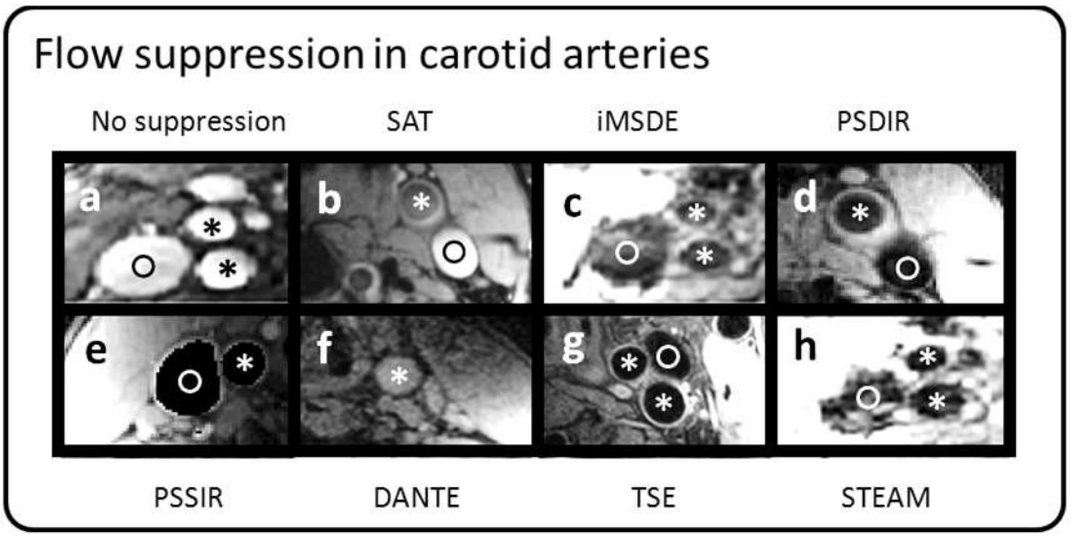

Figure 5.8 Test protocols performed in different healthy volunteers, showing that all methods can be applied in vivo. Carotid arteries are marked with an asterisk (*) and veins are marked with a circle (o).

5.5 Discussion and conclusion

In this research, seven methods for obtaining blood signal suppression were evaluated to gain insight in their behavior and characteristics, as an alternative is needed for the standard black blood methods such as DIR and QIR at clinical field strengths (1.5T and 3T), which are not available at 7T due to the lack of a transmit coil with large coverage. The results of this research demonstrate that many successful black blood techniques can be applied at 7T even in the absence of a body transmit coil. The performance of these seven techniques is quantified in terms of imaging performance versus RF power deposition in a well-controlled phantom setup, which can be used to develop one of these alternative methods eventually into a protocol that can be used in patients with atherosclerotic plaques.

Imaging performance was quantified for the four following criteria: flow suppression performance, signal attenuation in static tissue, sensitivity to B_1^+, and RF power deposition. The flow suppression performance, the *first* criterion, was quantified in the phantom model. Compared to the "golden standard" at 7T black blood imaging, the TSE, only the PSSIR and the STEAM method resulted in comparably good suppression levels of $SSR < 0.05$. Also the PSSIR and the DANTE method did reasonably well, $SSR < 0.2$ for all measured flows. The SAT and iMSDE method performed less well, with suppression levels of $SSR > 0.4$.

A good blood signal suppression method should leave the static tissue intact. Therefore the static tissue signal preservation (*second* criterion) was evaluated, together with its dependency on the

B_1^+ inhomogeneity (*third* criterion). In the PSSIR and STEAM method the static tissue was suppressed with $SSR < 0.6$, indicating a signal loss of more than 40%. The other methods only suffered up to 20% signal loss, and the PSDIR even gain signal, because of the additional echo that was acquired for phase correction. In none of the methods the static tissue showed to be very sensitive to B_1^+ inhomogeneity. Only the MSDE sequence (data not shown) was found to be very sensitive to small deviations of B_1^+, and therefore impractical for use with a local transmit coil. Instead, the iMSDE sequence was used in this paper, which is less B_1^+ dependent, due to the use of adiabatic RF pulses. However, this went along with an increased SAR, which was the *fourth* and last criterion that was evaluated. The PSDIR (rel. SAR = 14.5), iMSDE (rel. SAR = 17.2) and DANTE (rel. SAR = 15.8) were the most SAR intensive preparations, due to the adiabatic inversion pulses that were applied. The REST, PSSIR and STEAM all have a rel. SAR < 10. To put these SAR numbers into perspective the sequences should be seen in combination with the ability to share preparation pulses. The number of readouts that can be acquired after one preparation determines the overall SAR efficiency, which is essential to assess the feasibility of translating the sequence into a clinically useful protocol. The amount of readouts that can share one suppression preparation depends on factors like T_1 (PSSIR) and longitudinal B_1^+ coverage and determines the eventual efficiency and scan duration. The methods where the maximal amount of readouts per preparation was limited by the longitudinal B_1^+ coverage were SAT, iMSDE, PSDIR and DANTE. In these experiments even the fastest spins measured (89 cm/s) were still suppressed. This means that the reach of the preparation pulse, confined by the reach of the B_1^+ field of the transmit coil, was large enough for these spins, and possibly more readouts could be performed before un-prepared spins flow into the imaging slice. The PSSIR, TSE and STEAM methods do not need coverage outside the slice. The amount of readouts that can be acquired during one PSSIR preparation is determined by the T_1 decay: readouts can be acquired as long as the longitudinal magnetization does not pass zero (Figure 5.3). Increased T_1 relaxation time at 7T therefore increases the time efficiency of PSSIR. Using a STEAM preparation, feasibility of sharing a preparation with multiple readouts depends on the flip angle. Multiple readouts are possible, but will result in decreasing signal per readout proportional to the flip angle, because of the depletion of the Z_1 state (24).

The need for a pure T_1 weighted blood suppressed sequence at 7T was an important motivation for this study. Inherent contrast was added by some of the suppression methods. However, SAT, PSDIR and STEAM do not add any contrast weighting to the sequence. This leaves full control of the contrast weighting to the design of the readout. The iMSDE preparation adds T_2 weighting, which is a drawback for designing a T_1 weighted black blood sequence. PSSIR and DANTE add T_1 weighting which can actually be a benefit for designing a T_1 weighted black blood sequence.

An aspect that was not taken into account in the phantom experiments, but can be very important for the clinical feasibility of a sequence, is motion sensitivity. Since the phantom was well fixated, there was no loss of signal of the static tissue because of motion. However, especially methods

based on motion dependent phase dispersion (iMSDE, DANTE) can be subjected to motion induced signal loss. Methods that are purely based on inversion and inflow (SAT, PSSIR and PSDIR) are much less sensitive to motion.

The choice of parameters was not optimized for in vivo imaging, but to focus on the properties of the black blood preparation only. For this reason, no acceleration techniques were performed, like multiple k-lines per black blood preparation. This allows fair comparison between the blood signal suppression performance and SAR demand of the various suppression methods. However, for an in vivo optimized protocol, a thorough sequence optimization should be done for each of the methods, which should focus on the imaging efficiency, image contrast, and robustness. This is not straightforward, and requires future work.

In summary, in all seven alternative black blood techniques, static (tissue) signal has a relatively low sensitivity to the B_1^+ field, hence can be applied at ultra-high field MRI where B_1^+ fields are often non uniform or even focused to the area of interest only. Of all investigated sequences, the PSDIR, PSSIR, TSE and STEAM provide more than 10 fold signal attenuation throughout the different flow velocities. Whereas the increased blood T_1 at 7T is making the conventional DIR suppression technique less feasible than it already is, it is actually beneficial for the PSDIR and the PSSIR technique, allowing for more readout pulses. While PSDIR shows highest intrinsic signal to noise and therefore the method of choice for the given imaging parameters, the STEAM provides the lowest SAR of all methods. Consequently, depending on imaging volume, spatial resolution and temporal resolution, the STEAM may be a more time efficient method to obtain black blood MRI at 7T. PSSIR results in complete blood signal suppression and can work even with very local B_1^+ fields. It is therefore our conclusion that STEAM, PSDIR and PSSIR are the most promising methods for further optimization for *in vivo* application.

References

1 **Falk E** Why do plaques rupture? Circulation 1992; 86(6 Suppl):III30-42

2 **Naghavi M, Libby P, Falk E, Casscells SW, Litovsky S et al** From vulnerable plaque to vulnerable patient: a call for new definitions and risk assessment strategies: Part I. Circulation 2003; 108(14): 1664-1672

3 **Gupta A, Baradaran H, Schweitzer AD, et al** Carotid plaque MRI and stroke risk: a systematic review and meta-analysis. Stroke 2013; 44: 3071-3077

4 **Saam T, Hetterich H, Hoffmann V, et al** Meta-analysis and systematic review of the predictive value of carotid plaque hemorrhage on cerebrovascular events by magnetic resonance imaging. J Am Coll Cardiol 2013; 62: 1081-1091

5 **Steinman, DA, Rutt, BK** On the nature and reduction of plaque-mimicking flow artifacts in black blood MRI of the carotid bifurcation. Magn Reson Med 1998, 39(4), 635–641

6 **Kraff, O, Bitz, A, Breyer, T, Kruszona, S, Maderwald, S** Transmit / Receive Radiofrequency Array for Imaging the Carotid. Investigative Radiology 2011, 46, 246 – 254

7 **Koning, W, Bluemink, JJ, Langenhuizen, EAJ, Raaijmakers, AJ, Andreychenko, A, Van den Berg, CAT, Luijten, PR, et al** High-resolution MRI of the carotid arteries using a leaky waveguide transmitter and a high-density receive array at 7 T. Magn Reson Med 2012, 69(4), 1186–1193

8 **Edelman, R, Chien, D, Kim, D** Fast Selective Black Blood MR Imaging. Radiology 1991 (181): 655–660

9 **Yarnykh, VL, Yuan, C** T1-insensitive flow suppression using quadruple inversion-recovery. Magn Reson Med 2002, 48(5), 899–905

10 **Zhang, X, Petersen, ET, Ghariq, E, De Vis, JB, Webb, AG, Teeuwisse, WM, Hendrikse, J, et al** In vivo blood T(1) measurements at 1.5 T, 3 T, and 7 T. Magn Reson Med 2013; 70(4):1082-1086

11 **Rotte, AA, Koning, W, Truijman, MT, et al** Seven-Tesla Magnetic Resonance Imaging of Atherosclerotic Plaque in the Significantly Stenosed Carotid Artery – A feasibility study. Invest. Radiol 2014, PMID: 24918464

12 **Busse, RF, Hariharan, H, Vu, A, Brittain, JH** Fast spin echo sequences with very long echo trains: design of variable refocusing flip angle schedules and generation of clinical T2 contrast. Magn Reson Med, 55(5), 1030–1037

13 **Moody, AR, Murphy, RE, Morgan, PS, Martel, AL, Delay, GS, Allder, S, MacSweeney, ST, et al** Characterization of complicated carotid plaque with magnetic resonance direct thrombus imaging in patients with cerebral ischemia. Circulation 2003, 107(24), 3047–52

14 **Felmlee, P and Ehman, L** Spatial Presaturation: A Method for suppressing flow artifacts and improving depiction of vascular anatomy in MR imaging. Radiology 1987, 164(2): 559-564

15 **Ioannis Koktzoglou, Anish Kirpalani, Timothy J Carroll, Debiao Li, and James C Carr** Dark-blood MRI of the thoracic aorta with 3D diffusion-prepared steady-state free precession: initial clinical evaluation. AJR. American journal of roentgenology, 189(4):966–972, 2007

16 **Jinnan Wang, Vasily L Yarnykh, Thomas Hatsukami, Baocheng Chu, Niranjan Balu, and Chun Yuan** Improved Suppression of Plaque-Mimicking Artifacts in Black-Blood Carotid Atherosclerosis Imaging Using a Turbo Spin-Echo (TSE) Sequence. Magn Reson Med 2007, 58(5):973– 981

17 **Jinnan Wang, Marina S Ferguson, Niranjan Balu, Chun Yuan, Thomas S Hatsukami, and Peter Bo** Improved Carotid Intraplaque Hemorrhage Imaging Using a Slab-Selective Phase- Sensitive Inversion-Recovery (SPI) Sequence. Magn Reson Med 2010, 64(5):1332–1340

18 **Li, L, Miller, KL, Jezzard, P** DANTE-prepared pulse trains: a novel approach to motion-sensitized and motion-suppressed quantitative magnetic resonance imaging. Magn Reson Med, 68(5), 1423–1438

19 **Khaled Z Abd-Elmoniem, Robert G Weiss, and Matthias Stuber** Phase-sensitive black-blood coronary vessel wall imaging. Magn Reson Med 2010, 63(4):1021–30

20 **Robin A D E Graaf and Klaas Nicolay** Adiabatic rf Pulses : Applications to In Vivo NMR. Concepts in Magnetic Resonance, 9(4):247–268, 1997

21 **Morris, GA, Freeman, R** Selective Excitation in fourier transform nuclear magnetic resonance. J Magn Reson 2011; 213(2): 214-243

22 **Mosher TJ, Smith MB** A DANTE tagging sequence for the evaluation of translational sample motion. Magn Reson Med 1990;15:334–339

23 **Hahn, EL** Spin echoes. Physical Review, 80(4):580–594, 1950

24 **Hennig, J** Echos - How to generate recognize use or avoid them in MR Imaging Sequences. Conc Magn Reson 1991; 3: 125-143

25 **Scheffler, K** A pictorial description of steady-states in rapid magnetic resonance imaging. Conc Magn Reson 1999, 11(5), 291–304

26 **Krejza, J, Arkuszewski, M, Kasner, SE, et al** Carotid artery diameter in men and women and the relation to body and neck size. Stroke; J Cereb Circ 2006; 37(4):1103–1105

27 **Koning, W, Rotte, AAJ de, Bluemink, JJ, Velden, TA van der, Luijten, PR, Klomp, DWJ, Zwanenburg, JJM** MRI of the Carotid Artery at 7 Tesla : Quantitative Comparison With 3 Tesla. J Magn Reson Imaging 2014. doi:10.1002/jmri.24601

28 **Yarnykh, VL** Actual flip-angle imaging in the pulsed steady state: a method for rapid three-dimensional mapping of the transmitted radiofrequency field. Magn Reson Med 2007, 57(1), 192–200

Chapter 6

7 tesla MRI of atherosclerotic plaque in the significantly stenosed carotid artery

A.A.J. de Rotte, W. Koning, M.T.B. Truijman,
A.G. den Hartog, S.M. Bovens, A. Vink, S. Sepehrkhouy, J.J.M. Zwanenburg,
D.W.J. Klomp, G. Pasterkamp, F.L. Moll, P.R. Luijten, J.Hendrikse, G.J. de Borst

(published in *Investigative Radiology*, 2014, PMID: 24918464)

Abstract

Objectives

The objective of this study was to assess the feasibility of carotid vessel wall imaging at 7.0T for magnetic resonance imaging (MRI) in a series of patients with a symptomatic greater than 70% stenosis of the internal carotid artery.

Materials and Methods

First, a series of 6 healthy volunteers were scanned at 3.0T and 7.0T MRI to perform a signal-to-noise ratio comparison between these 2 field strengths. Second, in patients with a greater than 70% stenosed carotid artery, a 7.0T MRI protocol, consisting of a dual-echo turbo spin echo sequence (echo times of 45 and 150 milliseconds) and a T_1-weighted turbo spin echo sequence, was obtained. Lumen and vessel wall were delineated for interobserver and intraobserver reproducibility, and signal intensity distribution in the most severely stenosed part of the internal carotid artery was correlated with different plaque components on histopathologic findings.

Results

The mean (SD) signal-to-noise ratio in the vessel wall was 42 (12) at 7.0T and 24 (4) at 3.0T. Nineteen patients were included, but technical issues yielded carotid MRI data of 14 patients available for the final analysis. Of these patients, 4 were diagnosed with stroke, 7 were diagnosed with a transient ischemic attack, and 3 were diagnosed with amaurosis fugax. Intraclass correlation coefficient of the agreements of lumen and vessel wall determination between two observers and between the repeated measures of 1 observer were above 0.80 in both 3.0T and 7.0T data sets of the healthy volunteers and also in the 7.0T data set of the patients. Signal hyperintensity in the 7.0T magnetic resonance images was inversely proportional to calcification. Other correlations between plaque components and signal intensity could not be confirmed.

Conclusions

This first series of patients with carotid atherosclerotic plaque who were scanned at 7.0 T MRI shows that 7.0T MRI enables to adequately determine lumen and vessel wall areas. Signal hyperintensity in these 7.0T magnetic resonance images was inversely proportional to calcification. However, at this stage, no other correlations between histologic findings and vessel wall contrast were found. Implementation of in vivo high-resolution 7.0T MRI of plaque components for risk stratification remains challenging. Future development of hardware and software is still needed to attain a more robust setup and to enable complete plaque characterization, similar to what is currently possible with multiple MRI sequences at 1.5T and 3.0T MRI.

6.1 Introduction

Several magnetic resonance imaging (MRI) studies have shown that vulnerability of atherosclerotic carotid artery plaques can be determined by its components.[1-3] Hence, intraplaque hemorrhage (IPH) and a thin fibrous cap on top of a lipid-rich necrotic core (LRNC) can be used for risk stratification of the occurrence of cerebrovascular events.[4-8] The criterion standard to assess these different plaque components ex vivo is histopathology.[9] However, in vivo identification of different components may enable to identify subgroups of patients with a high risk for (recurrent) cerebrovascular ischemia. Thus far, most MRI studies on in vivo carotid plaque imaging have been performed at field strengths of 1.5 and 3.0T with successful results.[10-12] Multisequence MRI seems to be sufficient to reliably visualize different plaque components in vivo.[11,13,14] Still, the ability of MRI to detect local heterogeneity within a plaque, because of different components, strongly depends on signal-to-noise ratio (SNR) and contrast-to-noise ratio. Because histology shows that details of the plaque architecture often are at a submillimeter scale and beyond the resolution capacity of MRI in general, it is important to aspire for the highest possible spatial resolution. Accordingly, local surface coils in combination with an ultrahigh magnetic field strength of 7.0T may provide an SNR enabling plaque imaging with an increased spatial resolution. Despite the fact that 1.5 and 3.0T yield good results in plaque component imaging already,[1,3,4] an even higher field strength might enable the visualization of more subtle changes of the carotid artery wall in the early stages of plaque formation. In addition, changed relaxation parameters and susceptibility effects at 7.0T may eventually lead to altered and increased contrast between different plaque components. Except for 1 study that showed 7.0T MRI of an ulcerating plaque and 50% stenosis in the internal carotid artery in a single patient, no patient studies have been reported yet at 7.0T MRI.[15] The aim of the current study is to investigate the feasibility of carotid vessel wall imaging at 7.0T MRI in a series of patients with a greater than 70% internal carotid artery stenosis, who were scheduled for carotid endarterectomy (CEA). All patients were symptomatic because the decision to perform CEA in daily practice is based on symptoms and the stenosis grade. Magnetic resonance image quality and signal intensity were evaluated and correlated with histopathologic assessment of the surgically derived carotid artery plaque. To assess a measure for performance and reproducibility relative to 3.0T, an additional group of healthy volunteers was scanned at both 3.0 and 7.0T.

6.2 Methods

6.2.1 Participants

A 7.0T MRI protocol dedicated for carotid vessel wall imaging was obtained in the patients. All patients were diagnosed with a symptomatic carotid artery stenosis of greater than 70% and were

scheduled for CEA. Exclusion criteria were inability to undergo a 7.0T MRI scan, due to contraindications for 7.0T MRI (e.g. pacemakers, nerve stimulators, and other metallic implants). In addition, the healthy volunteers without contraindications to undergo both 3.0T and 7.0T MRI were scanned for a 3.0T versus 7.0T SNR comparison. Institutional review board approval was obtained for this prospective study, as previously described[16], and all participants gave written informed consent.

6.2.2 Magnetic Resonance Imaging

Ultra-high field strength MRI was performed on a 7.0T whole-body MRI system (Philips Healthcare, Cleveland, OH) with a leaky waveguide transmitter and high-density receive array (MR Coils B.V., Drunen, the Netherlands), designed for high-resolution carotid artery imaging at 7.0T MRI[17] (Figure 6.1).

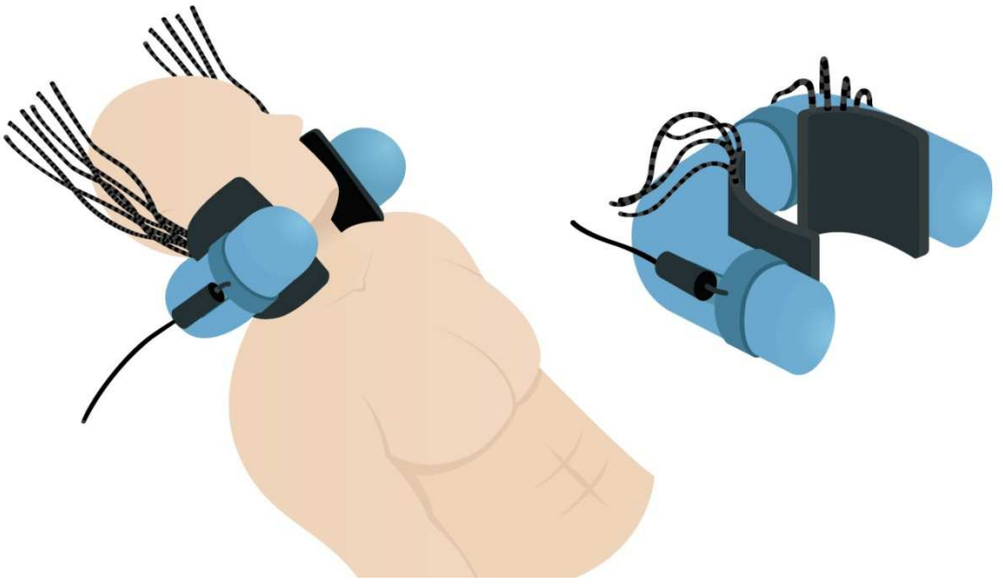

Figure 6.1 Carotid arteries setup at 7.0T MRI. The leaky waveguide transmitter, illustrated in blue, is positioned around the neck as shown on the left. The high-density receive arrays, illustrated in gray, are positioned between the neck and the leaky waveguide transmitter.

The receive array consisted of 30 receive channels bilaterally (15 elements per side). The optimal phase depends on both neck size as well as artery location and needed to be optimized for each individual participant. Because the transmit array consisted of 2 separate transmit channels, the B_1^+ fields could be optimized for a certain desired region using B_1^+ shimming.[17,18] For the B_1^+ shimming procedure, actual flip angle imaging maps were acquired for each of the 2 transmit channels using a double repetition time (T_R) method, with $T_{R,1}/T_{R,2}$ of 50/200 milliseconds, a nominal flip angle of 50 degrees, and a total duration of 1 minute 12 seconds.[19] With the use of actual flip angle imaging maps, the B_1^+ could be focused on both carotids or primarily on the carotid artery scheduled for CEA. High-field strength MRI was performed on a 3.0T whole-body

MRI system (Philips Achieva; Philips Healthcare, Best, The Netherlands) with an 8-channel phased-array coil (Shanghai Chenguang Medical Technologies Co, Shanghai, China) dedicated for carotid artery imaging.

The imaging protocol on both 3.0T and 7.0T MRI consisted of a dual-echo turbo spin echo (TSE) sequence and a T_1-weighted TSE sequence. The black blood T_1-weighted TSE sequence was developed after the start of the study and therefore not obtained in all patients. Scan parameters of all used sequences are shown in Table 6. A specific absorption rate (SAR) model specific for this transmit array[17] was used to ensure that all 7.0T protocols were acquired within the restrictions of the SAR guidelines, based on a maximum allowed SAR_{10g} of 10 W kg^{-1}.[20]

6.2.3 SNR analysis

The dual-echo TSE sequence as described previously and in Table 6 (page 98) was used for the SNR analysis of the carotid vessel wall.[21] The first echo of this sequence yields a proton density weighted (PDW) image, in which the SNR analysis was performed, and was acquired with a readout bandwidth of 224Hz. This measurement was performed in both carotid arteries of the 6 healthy volunteers at 7.0 and 3.0T. MeVisLab 2.4 (MeVis Medical Solutions AG, Bremen, Germany) was used for vessel wall segmentation, noise determination, and SNR calculation.

6.2.4 Image quality

In all participants, both the healthy volunteers and the patients, lumen and vessel wall were determined with VesselMass (Department of Radiology, Leiden University Medical Center, Leiden, the Netherlands). The available sequences were used to delineate both areas in all obtained slices, covering the common carotid artery and the internal carotid artery. The measurements were performed by two observers (A.R. and M.T.), both well trained in vessel wall analysis. With the assumption that a qualitative nondiagnostic image quality would give a lower intraclass correlation coefficient (ICC), this quantitative delineation of lumen and vessel wall is used to quantify the image quality.

6.2.5 Plaque analysis

Histology

Histology is analyzed according to the Athero-Express protocol previously described.[22] During the surgery, the distance between the distal side of the external carotid artery and the most severely stenosed part of the internal carotid artery was measured, as well as the length of the plaque. Both measurements were performed in situ and ex vivo after surgical removal. Subsequently, the internal and external carotid arteries as well as the most severely stenosed part of the internal carotid artery were marked with stitches. The endarterectomy specimens were fixed in formalin and embedded in paraffin. According to the Athero-Express protocol, only the most severely

stenosed part of the internal carotid artery was analyzed. On this section, 4 different stainings were applied to identify different plaque components: hematoxylin and eosin for the identification of calcification, IPH, and thrombus; Sirius red for collagen identification and measurement of the fibrous cap thickness; >-actin for smooth muscle cells; and CD68 for macrophage identification. The slides were scanned with a ScanScope XT scanner (Aperio Technologies, Inc, Vista, CA) and analyzed using Imagescope (Aperio Technologies). The percentage of the different plaque components (atheroma, collagen, smooth muscle cells, and calcification) was determined. The presence of IPH and luminal thrombus was determined, and macrophages were semi quantitatively scored as minor, moderate, or heavy. Subsequently, all plaques were classified according to the modified American Heart Association classification.[23] Finally, in plaques with a (thin) fibrous cap atheroma, the thickness of the fibrous cap was measured.

Table 6. Scan parameters of the 3.0T and 7.0T protocol used for the healthy volunteers and the patients

	3.0T		**7.0T**	
	dual-echo TSE	**T_1w TSE**	**dual-echo TSE**	**T_1w TSE**
FOV (mm)	150x179x31	180x180x26	150x179x31	180x180x26
Acquired voxelsize (mm^3)	0.50x0.51x2.00	0.40x0.41x1.50	0.50x0.51x2.00	0.40x0.41x1.50
Reconstructed voxelsize (mm^3)	0.28x0.28x2.00	0.19x0.19x1.50	0.28x0.28x2.00	0.19x0.19x1.50
TR/TI (ms)	3000/-	1000/-	3000/-	1000/-
TE	45*/150†	28	45*/ 150†	29
equivalent TE (ms)	27/70‡	18	27/70‡	19
Flip angle (degrees)	90	100	90	100
Reduced refocusing angles (degrees)	50	50	50	50
TSE-factor	16	8	16	8
NSA	1	2	1	2
SENSE factor (APxRL)	1x -	2x -	1x -	2x -
Fat suppression	SPIR	SPIR	SPIR	SPIR
Duration (min:sec)	4:36	3:56	4:36	3:52

Images were acquired in transversal orientation.

* First echo and

† Second echo;

‡ Equivalent echo time for a spin echo sequence with full 180-degree refocusing pulses, yielding similar T_2-weighting for tissues with T_1/T_2 approximately 2000/50ms;

AP indicates anterior-posterior; FOV, field of view; NSA, number of signal averages; SENSE, factor in the AP direction and RL direction; RL, right-left; SPIR, spectral presaturation with inversion recovery; T1w, T1-weighted; TE, echo time; TI, inversion time; TR, repetition time; TSE factor, echo train length (number of refocusing pulses); TSE, turbo spin echo.

MRI

Seven-tesla magnetic resonance images of the PDW sequence were used for signal intensity analysis (Figure 6.2). Signal intensities of the plaque were described, relative to the signal intensity of adjacent muscles, on the first echo of the dual-echo TSE sequence. Within the slice, associating with the most severely stenosed part of the internal carotid artery, each voxel of the vessel wall was defined as being hypointense, isointense, or hyperintense relative to the longus colli muscle. Hypointensity was defined as 2 standard deviations (SD) lower than longus colli muscle signal intensity and hyperintensity was defined as 2 SDs above longus colli muscle signal intensity. This signal intensity assessment was performed in a script build in MATLAB, version R2013a (The MathWorks, Inc, Natick, MA). A signal intensity correction was applied to correct for receive field inhomogeneity.

6.2.6 Statistics

For the interobserver and intraobserver reproducibility, 1 observer (A.R.) performed the analysis twice with 2 weeks in between. For the lumen and vessel wall, delineations were calculated. The ICC and Bland-Altman plots[24] were calculated for the intraobserver and interobserver reproducibility. Associations between different histological characteristics and signal intensities on MRI were evaluated with a simple binary logistic regression. Statistical analyses in this study were performed in IBM SPSS Statistics version 20 (IBM Corporation, Armonk, NY).

6.3 Results

6.3.1 Patient characteristics

In total, 19 symptomatic patients with severe stenosis (>70%) of the carotid artery, scheduled for CEA, were included between May 2011 and September 2013. Images of 2 patients were not available for the final analyses because of severe movement artifacts. In 1 patient, the B_1^+ shimming procedure failed; in 1 patient, F_0 determination failed; and in 1 patient, the histopathologic finding was not available because of fragmentation of the specimen. The final analyses were performed on 14 patients (10 men) with a mean age of 68 (range, 54-83) years. In 4 patients, stroke was diagnosed; in 7 patients, a transient ischemic attack was diagnosed; and in 3 patients, amaurosis fugax was diagnosed. Carotid endarterectomy was planned on the left carotid artery in 9 patients and on the right side in the remaining 5 patients.

6.3.2 SNR analysis

The SNR analysis was performed in the 6 healthy volunteers (2 men) with a mean age of 26 (range 23-33) years. Overview of all SNR measurements is given in Table 7. The mean (SD) SNR in the vessel wall was 42 (12) at 7.0T and 24 (4) at 3.0T.

Table 7. SNR measurement of the Carotid vessel wall on 3.0T and 7.0T in the 6 healthy volunteers

Depth, mm*			3.0T			7.0T		
Volunteer	**Left**	**Right**	**Left**	**Right**	**Mean**	**Left**	**Right**	**Mean**
1	23	22	17.5	24.4	21.2	70.4	62.3	66.3
2	28	29	25.0	32.0	28.5	39.5	31.5	35.5
3	23	22	29.1	27.6	28.3	52.2	25.0	38.6
4	26	25	18.5	24.5	21.5	41.5	22.3	31.9
5	24	27	28.2	27.8	28.0	46.5	39.8	43.2
6	25	26	16.4	20.5	18.4	34.2	43.2	38.7

* Depth of the common carotid artery, just beneath the bifurcation. Shortest distance from the middle of the arterial lumen to the skin surface is measured on the 3.0T MR images.

6.3.3 Image quality

First, 3.0T and 7.0T scans of the healthy volunteers were evaluated. An example of the 3.0T and 7.0T images of 1 healthy volunteer is given in Figure 6.3. For both inter-observer and intra-observer agreement, the ICCs for the lumen and vessel wall delineation were strong. In all categories, scores were above 0.90, except for the inter-observer agreement of the 7.0T data in the healthy volunteers (lumen: ICC = 0.87, 95% confidence interval (CI) = 0.80-0.90, $P < 0.001$; outer vessel wall: ICC = 0.84, 95% CI = 0.70-0.91, $P < 0.001$). Regarding the patient data, the ICCs for both inter-observer and intra-observer agreement of lumen and vessel wall delineation were 0.95 or stronger. These strong ICCs in both the healthy volunteers and the patients correspond with a minimal difference between both observers and between the repeated measurements as can be seen from the Bland-Altman plots.

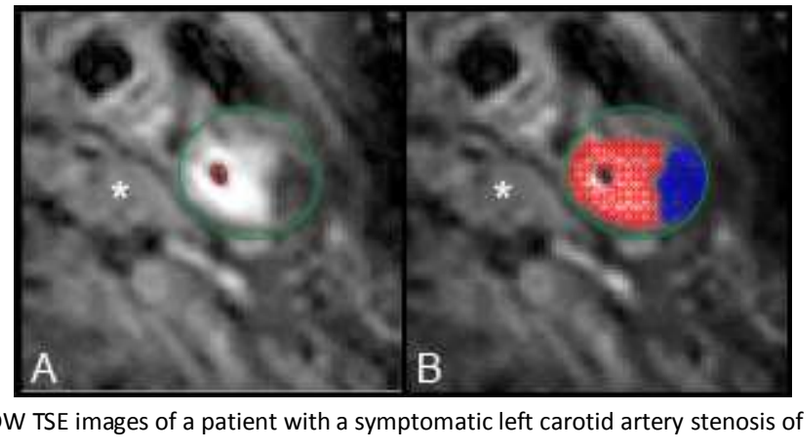

Figure 6.2 The PDW TSE images of a patient with a symptomatic left carotid artery stenosis of greater than 70% (male; 73 years). Example of signal intensity analysis with original image (A) and image with analysis (B). Red markers indicate hyperintense voxels and blue markers indicate hypointense voxels. Voxels with no marker

within the vessel wall represent isointense voxels relative to the adjacent muscle (*).

The agreements in the lumen and vessel wall measurements are provided in Table 8. The Bland-Altman plots of the patient evaluation are shown in Figure 6.4; the Bland-Altman plots of the healthy volunteer evaluation can be found in the electronic supplementary material (Supplemental Digital Content 1, http://links.lww.com/RLI/A1).

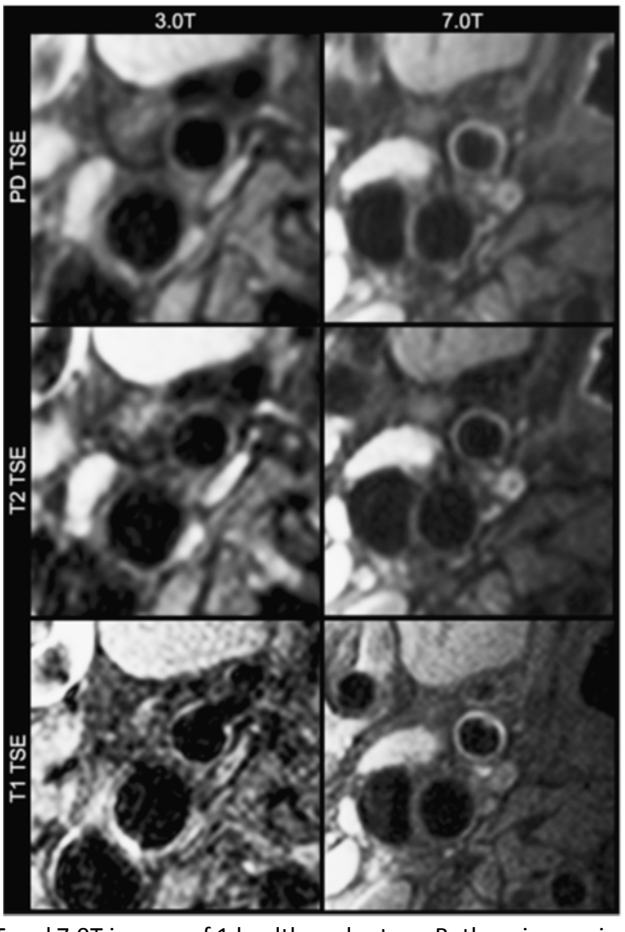

Figure 6.3 Example of 3.0T and 7.0T images of 1 healthy volunteer. Both series are just above the bifurcation of the right common carotid artery.

Table 8. ICCs of intra-observer and inter-observer reproducibility for determination of the lumen and the outer vessel wall

Intra-observer

		ICC	95%CI Lower	95%CI Upper	Mean	95%LoA Lower	95% LoA Upper
7.0T Patients	Lumen	0.95*	0.94	0.96	-0.01	-0.09	0.08
7.0T Patients	Outer	0.97*	0.96	0.97	0.58	-0.13	0.14
3.0T Volunteers	Lumen	0.98*	0.97	0.99	0.00	-0.05	0.04
3.0T Volunteers	Outer	0.98*	0.96	0.99	0.02	-0.07	0.10
7.0T Volunteers	Lumen	0.98*	0.97	0.99	0.00	-0.05	0.04
7.0T Volunteers	Outer	0.98*	0.97	0.99	0.01	-0.05	0.08

Inter-observer

		ICC	95%CI Lower	95%CI Upper	Mean	95%LoA Lower	95% LoA Upper
7.0T Patients	Lumen	0.95*	0.93	0.96	0.01	-0.09	0.11
7.0T Patients	Outer	0.94*	0.90	0.96	-0.04	-0.26	0.17
3.0T Volunteers	Lumen	0.98*	0.96	0.98	-0.01	-0.06	0.04
3.0T Volunteers	Outer	0.95*	0.70	0.98	-0.05	-0.14	0.05
7.0T Volunteers	Lumen	0.87*	0.80	0.91	0.00	-0.12	0.11
7.0T Volunteers	Outer	0.84*	0.70	0.91	-0.05	-0.24	0.14

A two-way random effects model was used, where both people effects and measures effects are random
* $P < 0.001$;
CI indicates confidence interval; ICC, intraclass correlation coefficient; LoA, limits of agreement.

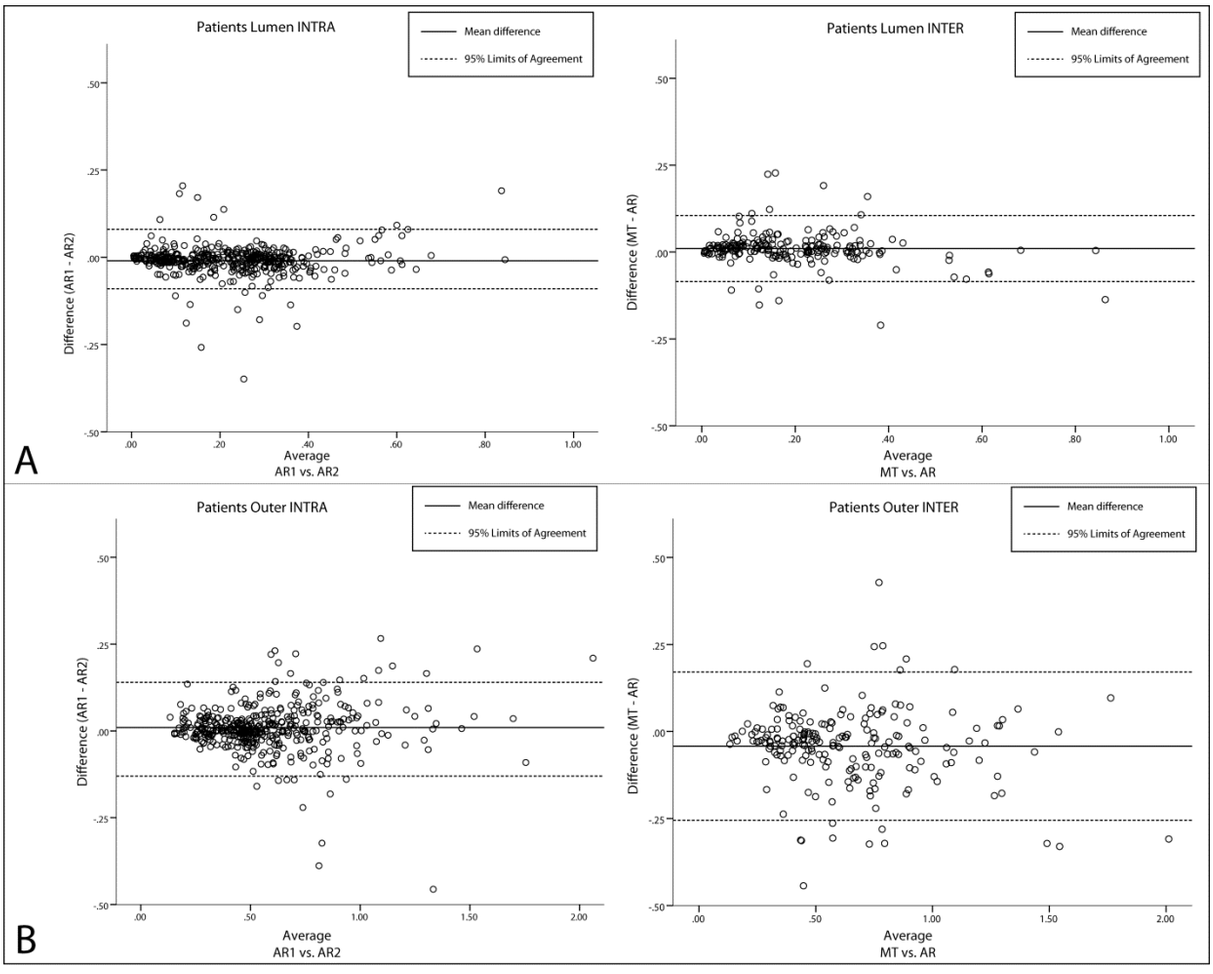

Figure 6.4 Bland-Altman plots of intraobserver and interobserver reproducibility of patient analysis. The plots of the healthy volunteers could be found in the Supplementary Material (Supplemental Digital Content 1, http://links.lww.com/RLI/A1). Intraobserver (left) and interobserver reproducibility (right) of lumen determination in patients (7.0T MRI) (a). Intraobserver (left) and interobserver reproducibility (right) of outer vessel wall determination in the patients (7.0T MRI) (b).

6.3.4 Plaque intensity

In Figure 6.5, an example of histopathologic finding with the corresponding slice on 7.0T MRI is shown. Simple binary logistic regression analysis demonstrated that the odds of having calcification in the atherosclerotic plaque decreased proportionally to the increase of magnetic resonance signal hyperintensity in the corresponding slice of the carotid plaque (Nagelkerke R2 = 0.55, X2 = 7.41, P = 0.006, odds ratio = 0.92 [95% CI = 0.00-0.97, P = 0.02]). The P value and 95% CI were based on a bootstrap of 1972 samples.

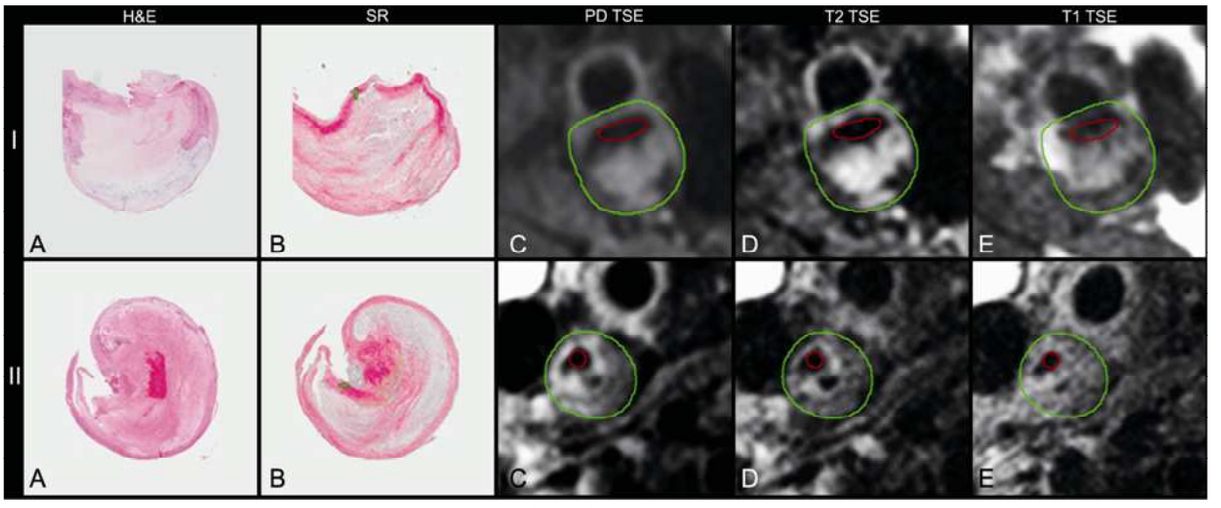

Figure 6.5 An overview of a 68-year-old patient (male) with a symptomatic stenosis in the left internal carotid artery (I) and an overview of a 75-year-old patient (male) with a symptomatic right internal carotid artery (II). Hematoxylin and eosin (A) and Sirus Red (B) stains of the most severely stenosed part of the internal carotid artery as well as PDW TSE (C), T2-weighted TSE (D), and T1-weighted TSE (E) sequence of the corresponding slice on 7.0 T.

Although IPH was seen on the histopathologic analysis in 4 of the 14 patients, a similar analysis could not demonstrate a significant relation between signal intensity of the atherosclerotic plaque (on the PDW images) and IPH. A relation between signal intensity and macrophage infiltration and lipid accumulation in the most severely stenosed part of the internal carotid artery could not be demonstrated. Interestingly, when looking at slices not representing the most severe stenosis, 2 cases showed a hyperintense signal in the plaque predominantly located in the region of the plaque-lumen interface on the first and second echoes of the dual-echo TSE sequence (Figure 6.3). In 2 patients, a suggestion of discontinuity at the location of the plaque-lumen interface on the first echo of the dual-echo TSE sequence was found. This discontinuity was also not on the level of the most severe stenosis of the internal carotid artery. Bilateral images of one of these patients are demonstrated in Figure 6.7. Because these were findings on slices not representing the most severe stenosis, no comparison could be made with histopathologic findings.

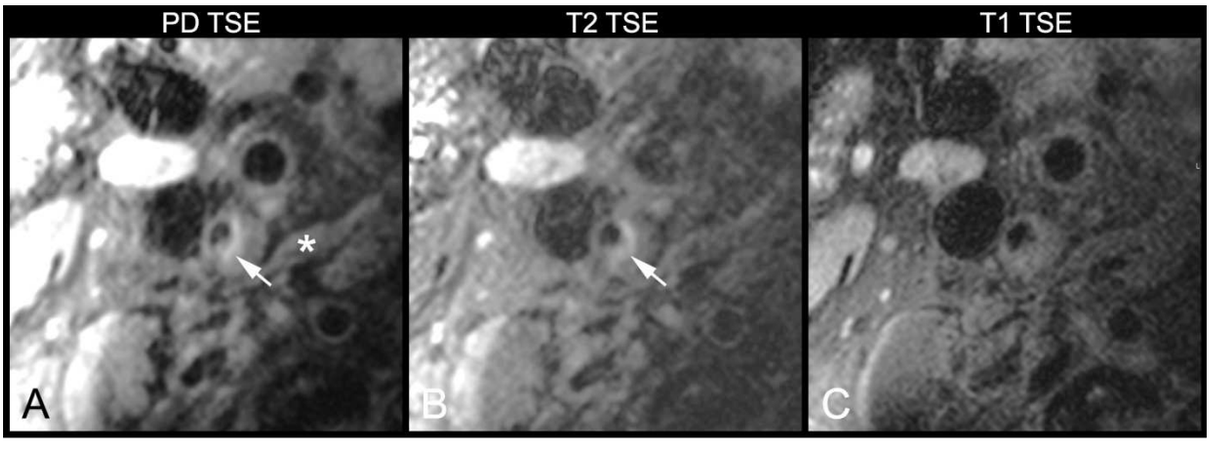

Figure 6.6 A PDW TSE (A), a T_2-weighted TSE (B), and a T_1-weighted TSE (C) sequence of 75-year-old patient (male) with transient ischemic symptoms in the right hemisphere based on a greater than 70% stenosis of the right internal carotid artery. One slice (slice thickness, 2.0 mm) above the level of the most severely stenosed part of the internal carotid artery, which is histopathologically analyzed. A hyperintense signal, relative to the adjacent muscle (*), is visible on the plaque-lumen interface (arrow). This hyperintense signal might be suggestive of a fibrous cap on top of a LRNC.

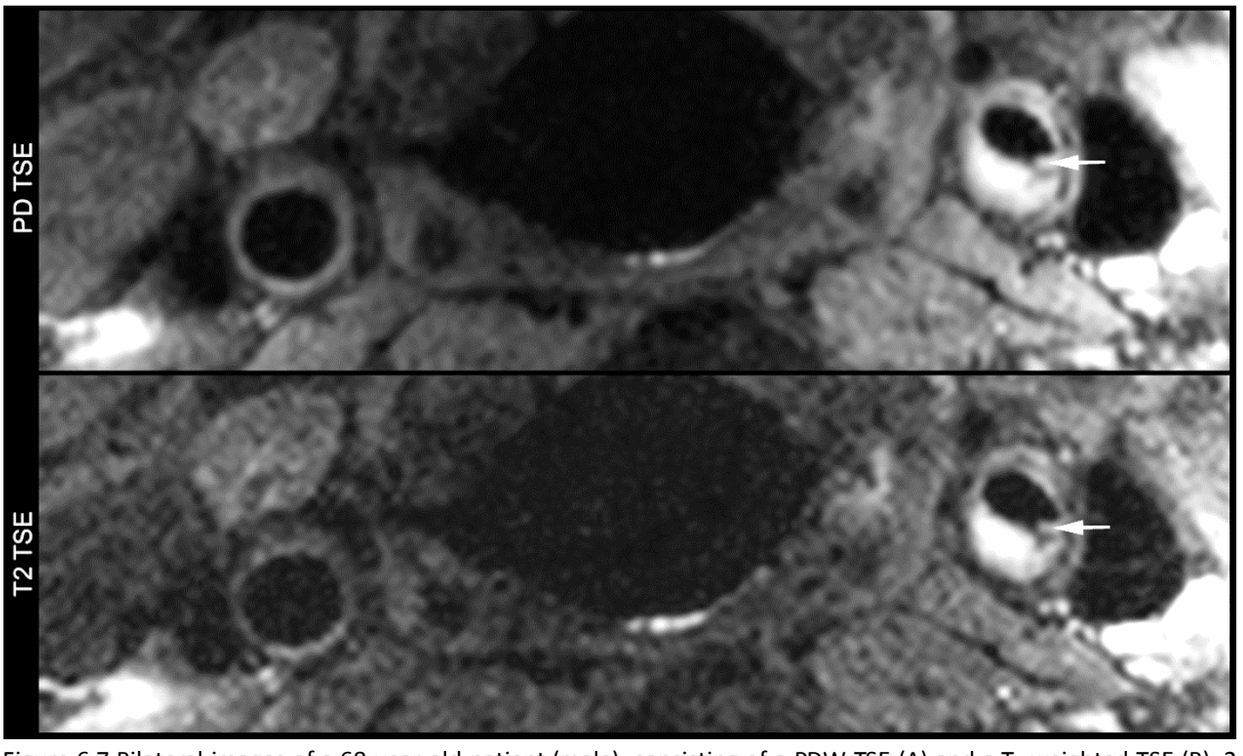

Figure 6.7 Bilateral images of a 68-year-old patient (male), consisting of a PDW TSE (A) and a T_2-weighted TSE (B), 2 slices (slice thickness, 2.0mm) beneath the level of the most severely stenosed part of the internal carotid artery, which is histopathologically analyzed. A suggestion of discontinuity of the plaque-lumen interface (arrow).

6.4 Discussion

Our study confirms that 7.0T MRI is feasible for carotid vessel wall imaging in a series of patients with a symptomatic highgrade carotid artery stenosis. An approximately 2-fold higher SNR in the carotid vessel wall was measured at 7.0T compared with 3.0T. Consequently, our study confirmed the accuracy of lumen and outer vessel wall delineation on 7.0T magnetic resonance images in a series of patients with severely stenosed carotid arteries.

Previous studies have shown the feasibility of 7.0T carotid vessel wall imaging in healthy volunteers.[15,17,25] A setup consisting of 1 unilateral local transmit/receive coil with a diameter of 15 cm resulted in reproducible vesselwall determination of the common carotid artery in healthy volunteers.[25] Second, with a rigid setup consisting of bilateral 8 surface loop transmit/receive coils, the first results of carotid vessel wall imaging in a single patient, with an ulcerating plaque and a

50% stenosis in the internal carotid artery, were presented.[15] In a third study, the combined transmit/receive coils were replaced by a separate transmit and receive coil, which yielded a more optimized setup with higher receive sensitivity while keeping SAR constraints low.[17] Together, these studies confirm that it is possible to cope with technical difficulties such as B_1^+ inhomogeneities and SAR limitations. However, the current study is the first study that attempts to visualize plaque characteristics with the available black-blood sequences on 7.0T MRI in a series of patients with a severe carotid artery stenosis.

The challenging setup of carotid artery imaging at 7.0T with dedicated surface coils and no body transmit coil makes the transfer from healthy control participants to patients nontrivial. While testing the feasibility in this more clinical situation with a series of elderly patients with significantly stenosing carotid artery plaques, we encountered several challenges. Some challenges were technical issues of which the most important was the determination of the center Larmor frequency (F_0) in the neck due to a very inhomogeneous B_0 field and the large amounts of fat present in the neck. In 1 patient, the incorrect determination of F_0 led to a nondiagnostic image quality. A second challenge comprised the B_1^+ homogeneity. The image quality was often diminished by the occurrence of local B_1^+ inhomogeneity because of a suboptimal field of either the transmit array or the 30- channel receive array. The fact that a single-size transmitter was used for all sizes of neck resulted in some cases of suboptimal placement of the transmit elements. However, in most cases, the B_1^+ shimming procedure enabled to correct this. Transmit B_1^+ fields determine the flip angle distribution throughout the neck. This flip angle distribution was set by the B_1^+ shimming procedure, in which the phases and powers of the transmit signal were determined for both transmit elements. Because of variation in neck size and depth of carotid arteries, the optimal phase sometimes varied up to 180 degrees between the participants. In case the available power was not sufficient to yield the desired flip angle in both the left and right carotid arteries, the carotid artery scheduled for CEA was given priority. In that case, the carotid artery at the contralateral side may end up in a region with very low B_1^+, visible as a black band in the image. On the other hand, in case the carotids were located at a depth more than 5cm from the surface of the neck, the low local receive field of the receive arrays resulted in a very low signal level, which also resulted in very low signal in the area of the carotids. Another important challenge was the inability of this setup to adequately fixate the patient's neck to avoid movement artifacts.

Although relaxation times are different at higher field strength, the same imaging sequences were used for the volunteer comparison at 3.0T and 7.0T. Because of the changed relaxation times, contrasts may turn out different between different field strengths. Therefore, the PDW scan, which has no additional contrast weighting, was used for the SNR analysis in the carotid vesselwall. The significantly higher SNR of the carotid vessel wall at 7.0T MRI compared with 3.0T is in agreement with the previous studies.[15,17,25] The SNR gain is slightly less than the expected gain in SNR of 7/3. However, although the first echo image of the dual-echo TSE was designed to be

PDW, the TR of 3000 milliseconds and the echo time of 50 milliseconds can still cause some T_1- and T_2-weighted signal loss, respectively. This effect is stronger at 7.0T than it is on 3.0T because T_1 increases and T_2 decreases with field strength and therefore explains more signal loss.[21] Although the SNR was still approximately twice as high and may allow the visualization of more subtle changes of the carotid artery wall in the early stages of plaque formation, this analysis is performed in young healthy volunteers. It is not guaranteed that the SNR ratio in elderly patients will be the same as the one found in the healthy volunteers, although elderly patients are more challenging at both field strengths. Nevertheless, the results of the image quality analysis have shown that lumen and vessel wall delineation remained adequate in both healthy volunteers and patients.

The high attainable SNR of this ultrahigh-field strength MRI should make it possible to obtain magnetic resonance images with an ultrahigh spatial resolution, needed for accurate plaque component imaging. Magnetic resonance imaging at a field strength of 1.5 and 3.0T has been proven to enable detailed visualization of different components within atherosclerotic plaque. Ultimately, for clinical use, different plaque components such as IPH and the fibrous cap status should be visualized in vivo with an even higher resolution at 7.0T MRI. Previously described multisequence MRI protocols for 1.5 and 3.0T recommend for IPH a highly T_1-weighted black-blood sequence or, at 1.5T, a time-of-flight sequence. For LRNC and fibrous cap analysis, a T_1-weighted black-blood TSE before and after contrast administration is required, and for calcification, different sequences can be used, preferably TSE sequences.[26] Despite the fact that the current study describes the first step toward clinical practice of even higher field strength MRI for plaque component imaging, there are 3 important limitations that have to be dealt with.

The first limitation is the lack of multiple contrast sequences at 7.0T that are conventionally used at 1.5T and 3T for carotid plaque component detection. At 7.0T, T_1-weighted TSE sequence has been subjected to T_2 contamination because of T_2 loss during the echo train, amplified by the decreased T_2 relaxation times at 7.0T. This has reduced the observed T_1 contrast and might have been the reason why, in Figure 6.7c, the plaque shows little contrast. This T_1-weighted TSE sequence is used as an alternative to conventional black-blood T_1-weighted sequences, which rely on blood suppression prepulses, which, in turn, rely on a high-coverage body transmit coil.[26] At lower field strengths, an integrated body transmit coil is standardly available, but at 7.0T, local excitation coils are used, which makes the conventional blood suppression more challenging. At this moment, the absence of dedicated black-blood sequences for plaque-component MRI at 7.0T makes a correlation between plaque components on histology and on 7.0T MRI difficult. However, the PDW sequence purely represents proton density of the visualized tissue, without additional contrast weightings. Because calcification has a low proton density and therefore should give a low signal, this sequence was used as a first validation of the contrast seen at 7.0T magnetic resonance images of the carotid artery. In addition, with the available hardware setup, it still seems to be hard to consistently obtain images with a certain level of quality. This emphasizes the

importance of future studies to develop dedicated T_1-weighted black-blood sequences and an even more robust hardware setup for 7.0T MRI of the carotid arteries to enable plaque component imaging.

Second, metallic implants have been an exclusion criterion for this ultra-high field strength MRI study. For this reason, a lot of patients were not considered for inclusion. Nevertheless, a recent study approves that not all metallic implants should be considered as a major contraindication for 7.0T MRI.[27] In addition, for many patients eligible for inclusion in this prospective study, the preoperative schedule frequently was too exciting or the idea of an experimental setup of the 7.0T MRI was too overwhelming, so they did not agree to undergo an extra MRI scan 1 day before surgery. These 2 factors caused a serious delay in the inclusion rate. Moreover, these factors were not present in the healthy volunteers, who hardly have any metallic implants and chose voluntarily to undergo the MRI. These problems underline that clinical implementation of a new imaging technique, such as 7.0T carotid plaque MRI, remains challenging in the specific patient group we used.

Third, for the development of MRI sequences and analysis of the images, comparison with histopathology is essential. Some patients did show a hyperintense lumen-vessel wall border (Figure 6.6) or a discontinuity in the lumen-vessel wall border (Figure 6.7). These images are suggestive of fibrous cap status information, but this could not be confirmed with histopathology because these findings were not found at the level of the most severely stenosed part of the internal carotid artery. Ideally, the whole plaque needs to be analyzed for a head-to-head comparison. However, according to the protocol of the Athero-Express study, only the most severely stenosed part was analyzed.[9]

6.5 Conclusions

This first series of patients with carotid atherosclerotic plaque who were scanned at 7.0T MRI shows that 7.0T MRI enables to adequately determine luminal and vessel wall areas. Signal hyperintensity in these 7.0T magnetic resonance images was inversely proportional to calcification. However, at this stage, no other correlations between histology and vessel wall contrast were found. The implementation of in vivo high-resolution 7.0T MRI of plaque components for risk stratification remains challenging. Future development of hardware and software is still needed to attain a more robust setup and to enable complete plaque characterization, similar to what is currently possible with multiple MRI sequences at 1.5T and 3.0T MRI.

References

1 **Gupta A, Baradaran H, Schweitzer AD,** et al. Carotid plaque MRI and stroke risk: a systematic review and meta-analysis. Stroke. 2013;44:3071-3077

2 **Hosseini AA, Kandiyil N, Macsweeney ST,** et al. Carotid plaque haemorrhage on magnetic resonance imaging strongly predicts recurrent ischemia and stroke. Ann Neurol. 2013;73:774-784

3 **Saam T, Hetterich H, Hoffmann V**, et al. Meta-analysis and systematic review of the predictive value of carotid plaque hemorrhage on cerebrovascular events by magnetic resonance imaging. J Am Coll Cardiol. 2013;62:1081-1091

4 **Kerwin WS, Hatsukami T, Yuan C,** et al. MRI of carotid atherosclerosis. AJR Am J Roentgenol. 2013;200: 304-313.

5 **Yuan C, Mitsumori LM, Ferguson MS**, et al. In vivo accuracy of multispectral magnetic resonance imaging for identifying lipid-rich necrotic cores and intraplaque hemorrhage in advanced human carotid plaques. Circulation. 2001;104:2051-2056

6 **Cai J, Hatsukami TS, Ferguson MS,** et al. In vivo quantitative measurement of intact fibrous cap and lipid-rich necrotic core size in atherosclerotic carotid plaque: comparison of high-resolution, contrast-enhanced magnetic resonance Imaging and histology. Circulation. 2005;112:3437-3444

7 **Yuan C, Kerwin WS, Ferguson MS,** et al. Contrast-enhanced high resolution MRI for atherosclerotic carotid artery tissue characterization. J Magn Reson Imaging. 2002;15:62-67

8 **Cappendijk VC, Kessels AG, Heeneman S**, et al. Comparison of lipid-rich necrotic core size in symptomatic and asymptomatic carotid atherosclerotic plaque: initial results. J Magn Reson Imaging. 2008;27:1356-1361

9 **Hellings WE, Pasterkamp G, Vollebregt A**, et al. Intraobserver and interobserver variability and spatial differences in histologic examination of carotid endarterectomy specimens. J Vasc Surg. 2007;46:1147-1154

10 **Underhill HR, Yarnykh VL, Hatsukami TS,** et al. Carotid plaque morphology and composition: initial comparison between 1.5- and 3.0-T magnetic field strengths. Radiology. 2008;248:550-560

11 **Cappendijk VC, Heeneman S, Kessels AG**, et al. Comparison of singlesequence T1w TFE MRI with multisequence MRI for the quantification of lipid-rich necrotic core in atherosclerotic plaque. J Magn Reson Imaging. 2008;27:1347-1355

12 **den Hartog AG, Bovens SM, Koning W**, et al. Current status of clinical magnetic resonance imaging for plaque characterisation in patients with carotid artery stenosis. Eur J Vasc Endovasc Surg. 2013;45:7-21

13 **Cappendijk VC, Cleutjens KB, Kessels AG**, et al. Assessment of human atherosclerotic carotid plaque components with multisequence MR imaging: initial experience. Radiology. 2005;234:487-492

14 **Chu B, Ferguson MS, Chen H**, et al. Magnetic resonance imaging features of the disruption-prone and the disrupted carotid plaque. JACC Cardiovasc Imaging. 2009;2:883-896

15 **Kraff O, Bitz AK, Breyer T**, et al. A transmit/receive radiofrequency array for imaging the carotid arteries at 7 Tesla: coil design and first in vivo results. Invest Radiol. 2011;46:246-254

16 **den Hartog AG, Bovens SM, Koning W**, et al. PLACD-7T study: atherosclerotic carotid plaque components correlated with cerebral damage at 7 tesla magnetic resonance imaging. Curr Cardiol Rev. 2011;7:28-34

17 **Koning W, Bluemink JJ, Langenhuizen EA**, et al. High-resolution MRI of the carotid arteries using a leaky waveguide transmitter and a high-density receive array at 7 T. Magn Reson Med. 2012;69:1186-1193

18 **Van de Moortele PF, Akgun C, Adriany G**, et al. B1 destructive interferences and spatial phase patterns at 7 Twith a head transceiver array coil. Magn Reson Med. 2005;54:1503-1518

19 **Yarnykh VL** Actual flip-angle imaging in the pulsed steady state: a method for rapid three-dimensional mapping of the transmitted radiofrequency field. Magn Reson Med. 2007;57:192-200

20 Protection TiCoN-IR. Medical magnetic resonance (MR) procedures: protection of patients. Health Phys. 2004;87:197-216

21 **KoningW, de Rotte AA, Bluemink JJ**, et al. MRI of the carotid artery at 7 tesla: quantitative comparison with 3 Tesla. J Magn Reson Imaging. 2014 [Epub ahead of print]

22 **Verhoeven BA, Velema E, Schoneveld AH**, et al. Athero-express: differential atherosclerotic plaque expression of mRNA and protein in relation to cardiovascular events and patient characteristics. Rationale and design. Eur J Epidemiol. 2004;19:1127-1133

23 **Virmani R, Kolodgie FD, Burke AP**, et al. Lessons from sudden coronary death: a comprehensive morphological classification scheme for atherosclerotic lesions. Arterioscler Thromb Vasc Biol. 2000;20:1262-1275

24 **Altman DG, Bland JM** Comparison of methods of measuring blood pressure. J Epidemiol Community Health. 1986;40:274-277

25 **Kroner ES, van Schinkel LD, Versluis MJ**, et al. Ultrahigh-field 7-T magnetic resonance carotid vessel wall imaging: initial experience in comparison with 3-T field strength. Invest Radiol. 2012;47:697-704

26 **Yuan C, Wang J, Balu N** High-field atherosclerotic plaque magnetic resonance imaging. Neuroimaging Clin N Am. 2012;22:271-284

27 **Wezel J, Kooij BJ, Webb AG** Assessing the MR compatibility of dental retainer wires at 7 Tesla. Magn Reson Med. 2013 [Epub ahead of print]

Chapter 7

Summary and Discussion

7.1 Summary and discussion

In the research presented in this thesis some innovative approaches are introduced to image the carotid arteries, or to magnetically label the blood within these arteries, with 7T MRI. The potential of ultra-high field MRI for carotid artery imaging is shown, and at the same time some technical hurdles related to the use of high frequency RF pulses are addressed. A solution for the high frequency RF coils is presented in **Chapter 2**: to avoid a compromise between SAR and SNR, separate arrays for transmission and reception have been constructed. Inspired by so-called radiative antennas (1), quarter-lambda dipole antennas were mounted on a tube with dielectric fluid for RF transmission. This array was used in combination with a 30 channel high density receiver array. The tube was shown to act as a wave-guide, effectively distributing the RF power around the neck. This also explained the asymmetric B_1^+ patterns that were found for different antenna positions on the tube. The good acceleration performance of the receiver array was demonstrated. High resolution images of the carotid artery were acquired in a healthy subject. For a better qualification of the overall performance of this setup, and to quantify the potential of 7T MRI for this application, a group of healthy subjects was scanned with this new setup at 7T, as well as on a state-of-the-art setup at 3T. This was shown in **Chapter 3**. Intrinsic SNR was compared and penetration depth was evaluated. At the average depth of the carotid arteries, a considerable gain in SNR of a factor 2.0 was measured, which is somewhat less than the theoretical factor of 7/3. Phantom experiments indicate that the high density receive array used at 7T suffers some loss in SNR due to mutual coil coupling. However, the setup benefits from the high density of receivers by increased acceleration capacity. T_1 and T_2 in the healthy vessel wall was measured and reported both for 3T and 7T. T_2 was found to be decreased at 7T, whereas an increase of T_1 was reported. These values were unknown at 7T and can be used for sequence optimization.

The leaky waveguide transmitter that was developed for RF excitation in the neck, could also be used to extend the reach of the standard 7T head coil for brain imaging. This was shown in **Chapter 4**. In this combination the waveguide transmitter was used for the magnetic labelling of the blood passing through the brain feeding arteries in the neck. With this combined setup, arterial spin labelling (ASL) sequences were applied to quantify perfusion in the brain. Whole brain ASL has shown to be challenging (2-4). The combined setup of the head coil together with external label coil allowed for efficient labelling, far enough below the brain to allow for whole brain ASL. B_1^+ performance was quantified, and possibilities were explored. B_1^+ shimming for territorial selection and increased labelling delays up to 4000ms were performed. An instability of the individual dynamically acquired perfusion maps was observed. Measurements were performed to correlate these instabilities to the respiration, however no significant correlation could be found.

Sequences cannot just be copied from 3T to be applied at 7T. Changed tissue properties and sequence restrictions at 7T require adapted sequences. The multi-sequences protocols used

successfully in earlier studies at 1.5 and 3T (5-7) have to be re-invented at 7T. Most difficult of all is the blood suppression pre-pulses that are used at 3T which, as is shown in **Chapter 5**, cannot be used at 7T. The culprit of this is the local character of the transmit coil. Standard blood suppression pulses (8, 9) require B_1^+ reach beyond the neck, even as far as the heart. With an integrated body coil as available at 3T this can sometimes already be on the edge. However, with a local transmit coil, this B_1^+ coverage is much less. **Chapter 5** shows an evaluation of alternative blood suppression techniques, that may require no or less B_1^+ coverage. An explorative research was done on a phantom flow model, and a quantitative comparison of potential suppression capacity of the different sequences was shown. Differences in suppression capacity were shown, but also it was shown that also the (unwanted) loss of the static tissue signal was different for each method. On top of that, sensitivity to B_1^+ inhomogeneity was very variable between the different methods and also the maximum obtainable acceleration (limited by SAR or a time limit for effective pre-pulse sharing) differed. In future research, all these factors should be taken into account, and *in vivo* optimizations should be done before a good high field blood suppression technique can be utilized. **Chapter 5** can serve as a basis for further developments for *in vivo* high field blood suppression techniques. A good blood suppression technique would facilitate more freedom in sequence design for carotid plaque imaging. With the sequences that are already available, a patient study is shown in **Chapter 6**. A group of patients with a higher than 70% stenosed carotid artery was scanned at 7T MRI and compared with histopathology. At this stage, full plaque component analysis was not possible yet due to the limited set of sequences. However, we showed carotid plaque imaging at 7T is feasible, even though sequence development could improve the outcome, especially with respect to the T_1W scan. This is mainly due to blood suppression complications as described in **Chapter 5**, which are not available at 7T at the moment of this study.

7.2 Present and future perspective

7T MRI is used in an increasing number of studies and starting to proof its value even for some clinical situations (10-12). Despite these achievements, many ultra-high field MRI technical developments are still in its infancy. New RF coil concepts will be required to fully explore the increased sensitivity of high field MRI in human applications. In this thesis a novel set of RF coils was developed (Chapter 2) and used in all other chapters. As developments continue, it is possible that even more efficient coils designs will be introduced in the coming years. The most essential aspect of this setup however, was the possibility to image with an array of closely positioned dedicated receivers, allowing for an uncompromised high SNR.

The particular neck pillow which was used as the basis for the dielectric medium for the transmit array was not optimally designed for MRI. Its dimensions were chosen by what was commercially available, and used for all subjects regardless of the neck diameter. It is possible that another geometry will give more robust results in all subject, even in subjects with a very thick neck.

Another possibility to gain more freedom and flexibility in the antenna design is to replace the dielectric material (deuterium oxide in this case) and use non-dielectric structures instead. As a result, the quarter lambda antennas are required to have much longer rods because of the increased effective wavelength. This is impractical, but may be compensated by reducing the outer dimensions by a so-called meander-design, as has been shown recently (13). As we saw in Chapter 3, also at the signal reception side there is room for further improvement by reduced coil coupling effects. In this research very small receive elements were used. It is a possibility to investigate the use of somewhat larger receive elements, as long as there is still enough flexibility to assure good coil coverage at each location; since inter coil gap-effects may increase while using larger elements. This way the acceleration capacity is compromised, but the coupling effects may be less.

SNR gain is one, contrast change is another. Depending on imaging parameters the SNR gain at 7T compared to 3T may become substantially compromised due to decreased T_2 and the increased T_1, as was shown in **Chapter 3**. An SNR gain of 2.0 that was found in **Chapter 3**, can be used to "buy" a smaller voxelsize. To yield the same SNR, that voxel volume can be 2.0 times smaller, which corresponds to a factor 1.26 for a decrease in all three dimensions. Whether this would in the future result in the detection of smaller plaque components, resulting in a significant improvement in risk assessment, was beyond the scope and reach of this research. It is possible that an increased resolution will indeed lead to an improved risk assessment. However, it is also possible that the main advantage of the increased field strength will instead be found in alternative contrasts.

To conclude: for carotid artery imaging, it is not a question *if* 7T MRI will improve image quality and contrast; it is a mere a question *how and when* this will happen. As the worldwide experience with ultra-high field MRI is growing, shown by many studies like the ones presented in this thesis, better coil solutions are explored, more efficient sequences are developed and more robust and user friendly setups will eventually be available. This raises the question how far to increase the field strength next? Human MR scanners are already available with a field strength of 9.4 T or 11.7T. Shorter wavelengths and higher RF frequency will cause more interference effects and more heating, respectively. However, especially for imaging objects of relatively small dimensions, like the carotid artery, even these field strengths may still be feasible. With multi-transmit techniques RF can be focused towards the carotids (as was shown in this thesis with two RF sources), and SAR hotspots can be distributed over a larger area, avoiding high local SAR values. In brain perfusion imaging, the higher field strengths mean even longer life times of the labelled blood, due to increased T_1.

In short: both challenges and opportunities increase with field strength. The future will show whether the optimal field strength for a certain application will be at 3T, 7T, 9.4T or even beyond.

References

1 **Raaijmakers, AJE, Ipek, O, Klomp, DWJ, Possanzini, C, Harvey, PR, Lagendijk, JJW, Berg, CAT van den** Design of a radiative surface coil array element at 7 T: The single-side adapted dipole antenna. Magn Reson Med 2011; 66(5): 1488-97

2 **Gardener G, Gowland PA, Francis ST** Implementation of quantitative perfusion imaging using pulsed arterial spin labeling at ultra-high field. Magn Reson Med 2009; 61(4): 874–82

3 **Teeuwisse WM, Webb AG, van Osch MJP** Arterial spin labeling at ultra-high field: All that glitters is not gold. Int J Imag Syst Tech 2010; 20(1): 62–70

4 **Luh W-M, Talagala SL, Li T-Q, Bandettini PA** Pseudo-continuous arterial spin labeling at 7 T for human brain: estimation and correction for off-resonance effects using a Prescan. Magn Reson Med 2013; 69(2): 402–10

5 **Cappendijk, VC, Heeneman, S, Kessels, AG, et al** Comparison of single-sequence T1w TFE MRI with multisequence MRI for the quantification of lipid-rich necrotic core in atherosclerotic plaque. J Magn Reson Imag 2008; 27:1347-1355

6 **Cappendijk, VC, Cleutjens, KB, Kessels, AG, et al** Assesment of human atherosclerotic carotid plaque components with multisequence MR imaging – intial experience. Radiology 2005; 234: 287-492

7 **Chu, B, Ferguson MS, Chen, H. et al** Magnetic resonance imaging features of the disruption-prone and the disrupted carotid plaque. JACC Cardiovasc Imag 2009; 2: 883-896

8 **Edelman, R, Chien, D, Kim, D** Fast Selective Black Blood MR Imaging. Radiology 1991 (181): 655–660

9 **Yarnykh, VL, Yuan C**. T1-insensitive flow suppression using quadruple inversion-recovery. Magn Reson Med 2002, 48(5), 899–905

10 **Chang, G. Xia, D, Chen, C et al** 7T MRI detects deterioration in subchondral bone micro-architecture in subjects with mild knee osteoarthritis as compared with healthy controls. J Magn Reson Imag 2014, PMID:2497471

11 **Vos, EK, Lagemaat, MW, Barentsz, JO et al** Image quality and cancer visibility of T2-weighted Magnetic Resonance Imaging of the prostate at 7 Tesla. Eur Radiology 2014, PMID 24865699

12 **Brundel, M, Rijmer, YD, van Veluw, SJ, et al** Cerebral microvascular lesions on High-Resolution 7T MRI in patients with type 2 diabetes. Diabetes 2014, PMID: 24760137

13 **Raaijmakers, AJE, Voogt, I, Klomp, DWJ, Luijten, PR, Berg, CAT van den** In Proceedings ISMRM 2013, Salt Lake City, USA.

Chapter 8

Samenvatting

Korte samenvatting in het Nederlands

MRI op zeer hoge magneetveldsterkte biedt grote mogelijkheden voor de beeldvorming van de interne mens. In dit onderzoek zijn de mogelijkheden, de moeilijkheden en de potenties van 7 tesla MRI onderzocht voor de *beeldvorming* en de *magnetisatie* van de halsslagaders.

In de halsslagaders kan, afhankelijk van leeftijd en leefstijl, atherosclerotische plakvorming voorkomen. Deze plakken kunnen zeer gevaarlijk zijn omdat deze in sommige gevallen kleine of grote deeltjes kunnen loslaten. Deze deeltjes stromen vervolgens via de bloedbaan richting de hersenen, met mogelijk desastreuze gevolgen. *Beeldvorming* van de halsslagaders is daarom belangrijk. *Magnetisatie* van het bloed in de halsslagaders kan gebruikt worden om de doorbloeding van de hersenen te meten. Hiermee kunnen mogelijk diverse afwijkingen in de hersenen in een vroeg stadium gediagnosticeerd worden.

7 tesla MRI kan mogelijk een stap voorwaarts hierin betekenen. 7 tesla MRI scanners zijn echter nog niet op alle tereinen direct toepasbaar. Bij een magneetveldsterkte van 7 tesla wordt er een fysisch regime bereikt waarin een aantal zaken, die op lagere veldsterkte minder belangrijk waren, ineens zeer dominant worden. De hoge frequenties waarmee de toegediende locale magneetveldjes moeten oscilleren om resonantie (de R van MRI) te bereiken kunnen voor opwarming van het lichaamsweefsel zorgen. Daarnaast kan bij dergelijk hoogfrequente oscillaties de voortplantingssnelheid van de electromagnetische golven (de lichtsnelheid) niet meer als onneindig groot worden beschouwd. Dit alles heeft ten gevolge dat nieuwe methodes en hardware ontwikkeld moeten worden. In dit proefschrift worden belangrijke stappen hierin gepresenteerd. MRI antennes zijn ontwikkeld die de uitdagingen van het hoge magneetveld gebruiken in hun voordeel. Hun toepassing is onderzocht, geëvalueerd en gebruikt op de potentie van 7T MRI van de carotiden en breinperfusie in kaart te brengen.

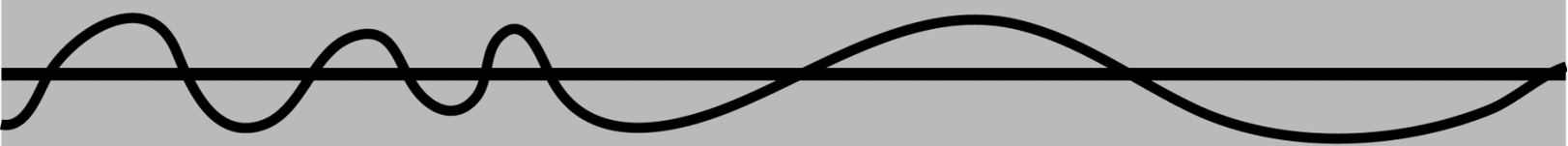

List of publications

Curriculum Vitae

Dankwoord

List of publications

Conference presentations (selection)

Koning, W, Bluemink, JJ, van der Velden, TA, Italiaander, M, Luijten, PR, Zwanenburg, JJM, Klomp, DWJ Quantitative Evaluation of the Current Status of Carotid Artery Imaging at 7T with respect to 3T. International Society for Magnetic Resonance in Medicine, 2013 Salt Lake City, Utah, USA.

Koning, W, Petersen, ET, Zwanenburg, JJM, Luijten, PR, Klomp, DWJ Full Brain and Territoriall Arterial Spin Labeling with External RF Shimmed Labeling Coil at 7 Tesla. International Society for Magnetic Resonance in Medicine, 2013 Salt Lake City, Utah, USA.

Koning, W, Bluemink, JJ, Petersen, ET, Raaijmakers, AJ, Henning, A, van den Berg, CAT, Zwanenburg, JJM, Luijten, PR, Klomp, DWJ A Setup for Continuous Arterial Spin Labeling with a 4 Channel Radiative Labeling Coil Allowing for High Duty Cycle Labeling at 7 Tesla. International Society for Magnetic Resonance in Medicine, 2012 Melbourne, International Society for Magnetic Resonance in Medicine, 2012 Melbourne, Victoria, Australia.

Koning, W, Bluemink, JJ, Boer, VO, Raaijmakers, AJ, Henning, A, Zwanenburg, JJM, van den Berg, CAT, Luijten, PR, Klomp, DWJ Radio Frequent Shimming of the Neck Using a 2 and a 4 Channel Travelling Wave Neck Array at 7T MRI. Oral presentation, International Society for Magnetic Resonance in Medicine, 2012 Melbourne, Victoria, Australia.

Koning, W, Langenhuizen, EAJ, Raaijmakers, AJ, van den Berg, CAT, Zwanenburg, JJM, Luijten, PR, Klomp, DWJ 6 Channel Radiative Transmit Array with a 16 Channel Surface Receiver Array for Improved Carotid Vessel Wall Imaging at 7T. Oral presentation, International Society for Magnetic Resonance in Medicine, 2011 Montréal, Québec, Canada.

Koning, W, Kroeze, H, van de Bank, BL, Boer, VO, van den Berg, CAT, Zwanenburg, JJM, Luijten, PR, Klomp, DWJ Traveling Wave MRI for the Acquisition of Reference Images for Parallel Imaging at the Carotid Artery at 7T – Proof of Concept. International Society for Magnetic Resonance in Medicine, 2010 Stockholm, Sweden.

Peer-reviewed publications

Koning, W., de Rotte, A.A.J., Bluemink, J.J., van der Velden, T.A., Luijten, P.R., Klomp, D.W.J., Zwanenburg, J.J.M. MRI of the Carotid Artery at 7 Tesla: Quantitative comparison with 3 Tesla. Journal of Magnetic Resonance 2014, PMID 24578311.

de Rotte, AAJ, **Koning, W**, den Hartog, AG, Bovens, SM, Moll, FJ, Klomp, DWJ, Luijten, PR, de Borst, GJ, Hendrikse, J, 7.0 T MRI detection of cerebral microinfarcts in patients with a symptomatic high-grade carotid artery stenosis. Journal of Cereb. Bl

de Rotte, AAJ, **Koning, W**, Truijman, MTB, den Hartog, AG, Bovens, SM, Vink, A, Sepehrkhouy, S, Zwanenburg, JJM, Klomp, DWJ, Pasterkamp, G, Moll, FJ, Luijten, PR, Hendrikse, J, de Borst, GJ, 7.0T MRI of Atherosclerotic Plaque in the Significantly Stenosed Carotid Artery. Investigative Radiology 2014

Koning, W, Bluemink, JJ, Langenhuizen, EAJ, Raaijmakers, AJ, Andreychenko, AE, van den Berg, CAT, Luijten, PR, Zwanenburg, JJM, Klomp, DWJ, High-Resolution MRI of the Carotid Arteries Using a Leaky Waveguide Transmitter and a High-Density Receive array at 7 Tesla. Magnetic Resonance in Medicine 69: 1186 – 1193 (2013)

den Hartog AG, Bovens, SM, **Koning, W**, Hendrikse, J, Luijten, PR, Moll, FL, Pasterkamp, G, de Borst, GJ Current status of Clinical Magnetic Resonance Imaging for plaque characterisation in patients with carotid artery stenosis. European Journal of Endovascular Surgery 45: 7-21 (2013)

Kalleveen, IM, **Koning, W**, Boer, VO, Luijten, PR, Zwanenburg, JJM, Klomp, DWJ Adiabatic Turbo Spin Echo in human applications at 7 Tesla. Magnetic Resonance in Medicine 68(2): 580 – 587 (2011)

den Hartog AG, Bovens, SM, **Koning, W**, Hendrikse, J, Moll, FL, Pasterkamp, G, de Borst, GJ PLACD-7T Study: Atherosclerotic Carotid Plaque Components Correlated with Cerebral Damage at 7 Tesla Magnetic Resonance Imaging. Current Cardiology Reviews 7: 28 – 34 (2011)

Curiculum Vitae

Wouter Koning (Wageningen, 1979) finished his pre-university secondary education in 1996 in Arnhem. After different explorative experiences he started a study in Biomedical Engineering at the University of Technology in Eindhoven. There, after specializing in fluid dynamics, he came in touch with the fascinating field of magnetic resonance imaging and joined the MRI group of prof. Klaas Nicolay. Under his wings, he went to Canada and did research on MRI techniques to detect single iron loaded cells, at the University of Western Ontario, under the supervision of prof. Brian Rutt. Back in The Netherlands he obtained his MSc degree in 2009 with his research on MRI techniques for obtaining positive contrast using superparamagnetic contrast agents.

The same year, Wouter joined the high field MRI group of prof. Peter Luijten in the UMC Utrecht, where he did research on sequence and hardware design for 7 tesla MRI. This resulted in this PhD thesis and in his marriage with Natasha, who was working as a scientist in the same UMC at that time.

Wouter decided to continue contributing to science, but now at a more fundamental level: in 2014 he started working as a physics teacher at Het Gooi Lyceum in Bussum.

Dankwoord

Geen promotie zonder proefschrift, geen proefschrift zonder dankwoord, en geen dankwoord zonder clichés.

Dit proefschrift zou niet tot stand hebben kunnen komen zonder de vele geweldige mensen die ik de afgelopen jaren om me heen heb gehad. Ik wil graag een aantal mensen bedanken die op de een of andere, directe of indirecte wijze een bijdrage hebben geleverd aan dit proefschrift.

Allereerst mijn promotor **Peter Luijten**. Peter, ik vond je rol in de groep ontzettend prettig. Je staat niet zozeer in de groep, als wel erboven, en hebt dat vind ik op een hele prettige en effectieve manier gedaan. De meetings met jou hadden een sterk even-orde-op-zaken-stellen karakter, en dat was erg prettig en productief. Bedankt voor deze tijd en succes met je nieuwe verantwoordelijkheden en met de muziek!

Mijn copromotoren **Dennis Klomp** en **Jaco Zwanenburg**. Ik denk dat ik het onmogelijk beter had kunnen treffen met dit duo aan copromotoren. Dennis, de eerste helft van mijn onderzoek heb ik vooral veel onder jouw vleugels gevlogen. Een onderzoeksgroep moet maar net het geluk hebben dat er zó een positieve, enthousiaste, motiverende, efficiënte en inventieve groepleider als jij rondloopt, en dat geluk heeft de 7T groep. De 7T groep is een echt team, zonder interne competitie en concurrentie strijdjes, en daar hou ik jou voor een groot deel verantwoordelijk voor. Jaco, de tweede helft had ik meer met jou te maken. En jij, helaas voor jou, meer met mij. Ik heb het je niet echt gemakkelijk gemaakt. Maar als er iemand was waar ik toch altijd op kon rekenen, dan was jij het en daar ben ik je ontzettend dankbaar voor. We zijn behoorlijke tegenpolen wat betreft werkwijze, maar op een andere manier zaten we toch ook vaak juist op dezelfde golflengte. Je bent echt een enorme hulp geweest, bedankt! Succes met Joep.

Aanvullend aan dit rijtje wil ik graag mijn professor van weleer **Klaas Nicolay** bedanken. Klaas, overal (maar dan ook overal) kom ik mensen tegen die bij jou aan de TU/e in de MRI zijn grootgebracht en afgestudeerd. Ik denk dat jouw bijdrage aan de MRI wereld moeilijk te overschatten is.

Esben, I was lucky to have one of the biggest ASL experts in the world by my side, which resulted in Chapter 4. Your sense of humor combined with your relaxed personality, made those experiments all really fun, thanks a lot!

Tijl, ik had de mazzel dat ik jou mocht begeleiden in je afstuderen, al was die mazzel natuurlijk vooral ook andersom. Jouw afstudeerwerk heeft geresulteerd in Hoofdstuk 5 van dit boek. Dat was een heerlijk jaartje experimenteren, sequence development, creatieve uitspattingen en nachten doorhalen achter de scanner, filmpje erbij, terwijl jij bang was dat het flow fantoom zou gaan lekker en de 7T met kortsluiting zou platleggen. Mooie tijd waar ik met veel plezier naar

terugkijk! The other student who flew sort-of under my wings for a while: **Dhaval,** thanks for my first bhangra lessons in the 7T control room during the scan sessions!

Gert-Jan de Borst, bedankt voor de samenwerking met de vaatchirurgie.

Alexandra, de hele patienten studie is dank zij jou goed van de grond gekomen. Het soms behoorlijk uitdagend, maar je heerlijke enthousiaste houding en enorme discipline hebben toch tot een mooie publicatie en Hoofdstuk 6 in dit boekje geleid. En ook nog een gezellige kantoorgenoot, thanks!

Hanneke, je hebt een grote bijdrage geleverd aan dit proefschrift met de RF simulaties. Supergezellig toen jij nog op Q4 zat, en leuke scansessies altijd!

Michel-ik-fix-het-wel-even**-Italiaander, Mark** en **Ingmar,** bedankt voor de vele technische ondersteuning!

Wat de oude garde 7T mensen betreft die ik aantrof toen ik begon: **Alexander, Anja, Bart, Catalina, Daniel, Fredy, Hans, Irene, Jeroen, Mariska, Natalia, Vincent en Wybe.** Ja, gewoon een stel zeer fijne en geschikte mensen, waarvan we ook de mensen die uitgewaaid zijn gelukkig nog af en toe zien. Lange tijd het kantoor gedeeld met Catalina, Daniel en Wybe. Dat voelde echt lekker thuis. Bedankt voor de mooie tijd allemaal. De 7T groep is aardig gegroeid sindsdien, en een nieuwe generatie is aan de groep toegevoegd: **Alex, Martijn, Tijl, Ronald, Joep en Jannie,** en later **Anita, Nikki, Arjen, Erwin, Lennard,** namen noemen is namen vergeten, ik stop maar. Bottom line: de sfeer is er altijd bijzonder goed onder gebleven en ik ben blij een bloeiende groep achter te laten! Al is het natuurlijk altijd maar afwachten hoe de boel zonder mij gaat functioneren.

Sylvia, jij bent het kloppende moederhart van de groep, die alle stormachtige veranderingen in de groep maar steeds in goede banen moet leiden. Ik heb het altijd heel prettig gevonden dat jij er bent op Q4, bedankt voor de gezelligheid! **Kapitein Hugo**, bedankt voor een onvergetelijke zeiltocht over zee van Frankrijk naar Nederland, waar Vincent en ik het zelfs hebben weten te schoppen tot ketelbinkie 1^{e} klas (wat dat ook moge betekenen) na het passeren van de nulmeridiaan.

De dokterinnetjes (**Bertine, Mies, Laura, Jill en Anja-van-der-Kolk-radiologie**): ik heb jullie gezellig kantoortje best gemist het laatste jaartje, nadat jullie één voor één verdwenen. Ik kon daar altijd even terecht om jullie van het werk te houden. Wat waren dat gezellige tijden. De communicatie tussen ons werd steeds beter. Op het eind was een snelle “nu even niet, Wouter” (meteen bij het openen van jullie deur), of het simpelweg ophouden van jullie koptelefoons, genoeg om te begrijpen dat jullie ook af en toe gewoon even wat werk wilden doen. Gelukkig werd er op jullie kantoortje nooit geroddeld, want daar houden we niet van. Qua planning was **Anja** (Anja van der Kolk heeft een agenda) altijd mijn grote voorbeeld waar ik helaas nooit iets van heb geleerd.

De mensen van de stichting huisvesting personeel (SHP): **Coby, Jan** en **Ria.** Dankzij jullie heb ik heerlijk kunnen wonen in een bonte verzameling van wetenschappers uit de hele wereld, waarvan ik er ook nog met één getrouwd ben geraakt. Bedankt voor de fijne communicatie en het scheppen van de (woon)omstandigheden waarin ik dit proefschrift heb kunnen schrijven!

So many people from all over the world with whom I shared our great place in the Lange Nieuwstraat. Thanks to you all, the PhD time became a very memorable time. Just a few of the many I would like to mention: **Susana, Roberto, Natasha, Saskia, Eissa, Eduardo, Anibal, Magda, Mette, Pradeep, Anup, Joana, Ela, Wilt, Amin, Vinicius, Gudrun, Thomas, Welling, Eric, Tristan, Suzanne, Emrah, Casper....** So many nice occasions, with so many different cultures, some nice culture clashes every now and then, and also a lot of support and sharing. Nice diners and parties. You guys were my family for many years and I will definitely see some of you around!

Mijn geweldige paranimfen, twee wijze mensen: de geniale musicus en wiskundige **Alessandro** en de briljante fysicus **Anna** (in het dankwoord mag je best een beetje overdrijven, al is het in dit geval maar een klein beetje overdreven). De serie van drie is compleet nu. We begonnen alle drie rond dezelfde tijd aan ons onderzoek. Ik vond Alessandro een rare kwiebus en Anna een typische stugge Russin en had nooit gedacht dat we zo goed bevriend zouden geraken. Veel meegemaakt. Heerlijke tijd, bedankt!

Familie en vrienden laat ik buiten beschouwing, behalve degenen die voor me hebben moeten afzien in de 7T scanner. En dat zijn er toch wel een aantal, met als toppunt mijn broertje, die ik eens op een zaterdag ruim zes uur in de scanner heb gehouden (met pauzes hoor). Veel dank aan alle vrijwilligers, en met name de patienten die vrijwillig en zonder belang hebben meegeholpen aan dit onderzoek.

Hoppakidee, klaar!